Christoph Baumann

Neutral Pion and Direct Photon Production in the SPS Energy Regime

— 2009 —

Experimentelle Physik

Neutral Pion and Direct Photon Production in the SPS Energy Regime

Inauguraldissertation
zur Erlangung des Doktorgrades
der Naturwissenschaften im Fachbereich Physik
der Mathematisch-Naturwissenschaftlichen Fakultät
der Westfälischen Wilhelms-Universität Münster

vorgelegt von
Christoph Baumann
aus Münster

– 2009 –

Dekan:	Prof. Dr. J. P. Wessels
Erster Gutachter:	Prof. Dr. J. P. Wessels
Zweiter Gutachter:	Priv.-Doz. Dr. K. Reygers
Tag der Disputation:	21.07.2009
Tag der Promotion:	21.07.2009

Gegenüber der ursprünglich abgegebenen Version dieser Arbeit wurden einige Korrekturen vorgenommen.
Die Ergebnisse sowie die Abbildungen der Arbeit sind unverändert.

Contents

1. Introduction

The search for the quark-gluon plasma (QGP) has been the major driving force behind research activities in the field of ultra-relativisic heavy-ion physics in the last decades. Since the start of the experimental program at the BNL-AGS, pursuit of such extreme states of matter have been the focus of many experiments. The predicted deconfinement of quarks and gluons is not only of interest with respect to the Standard Model of Particle Physics, it is also relevant for cosmology. Current models assume that the universe was filled with a quark-gluon plasma shortly after the Big Bang. Experimental results from heavy-ion experiments can help to refine the understanding of the early phase of the cosmos.

A first milestone in the search for the QGP was the CERN press release in 2000, announcing the discovery of a hot and dense state of matter bearing many properties of the predicted QGP. In 2005, the four major RHIC experiments jointly announced the creation of an extreme state of matter, similar to the predicted QGP, although some key properties, e.g. the similarity to a perfect fluid, were unexpected. The start of the LHC research program scheduled for the end of this year, evidence from lattice QCD calculations for the existence of a critical point in the phase diagram of hadronic matter, and the beginning of the commissioning for the new FAIR facility have fueled interest in understanding the energy dependence of the properties of the extreme state of matter created in ultra-relativistic heavy-ion collisions.

In this thesis, the analyses of experimental data from two heavy-ion experiments are described: the PHENIX experiment has obtained data of Cu+Cu collisions at a center-of-mass energy of 22.4 GeV, close to the top energy of the SPS accelerator for heavy ions. WA98 has recorded data sets from p+Pb and p+C collisions at $\sqrt{s_{\mathrm{NN}}} = 17.3$ GeV.

Two possible signatures of a QGP are the focus of these analyses: the search for experimental evidence of jet quenching and the search for a thermal direct photon signal. While the discovery of jet quenching is clearly established at RHIC energies. a possible influence of this effect in the SPS energy regime has remained unclear. Especially the lack of a reliable, measured reference with high p_{T} coverage has posed a problem. The measurement of the neutral pion production in p+Pb and p+C collisions can be used to address this issue by serving as a baseline for the previously published Pb+Pb results. The measurement of the neutral pion production in the PHENIX Cu+Cu data can also help to quantify jet quenching in the SPS energy regime and allows controlling the consistency of RHIC results with SPS measure-

ments experimentally. The analysis of the direct photon production in the p+C and
p+Pb data can help to set limits on the contribution of prompt direct photons at
SPS energies to the inclusive photon spectrum. With such limits it may be possible
to quantify a thermal contribution in the published direct photon measurements
from Pb+Pb collisions.

2.   The Quark-Gluon Plasma

The term quark-gluon plasma describes a state of matter in which the confinement of quarks and gluons is locally revoked. In this chapter the theoretical foundations and the predicted properties of this state are presented.

2.1   The Standard Model

The established theoretical description of elementary particles and their fundamental interactions is provided by the so-called Standard Model of particle physics. The standard model contains six leptons and six quarks as elementary building blocks of hadronic matter. Within the standard model two of the elementary forces, the electromagnetic and the weak interaction, can be described by a unified approach as electroweak interaction, the strong interaction is described by a separate but formally similar approach. The interactions are mediated by specific vector bosons, which are characterized by an integral spin: the electromagnetic interaction is mediated by the photon, the weak interaction by the $W^{\pm}$- and Z-bosons and the strong interaction by gluons [Per00, Yag05, Pov06].

The elementary particles are all fermions, i.e. they have a spin of 1/2. They can be grouped into three families as shown in Table 2.1. The lightest particles are the three neutrinos, which do not carry an electric charge. So far only upper limits for their mass have been determined [Ams08]. From the measurement of mass differences in oscillation experiments by the KAMIOKANDE experiment it could, however, be concluded that at least two neutrinos necessarily have a non-zero mass [Fuk98]. The other three leptons, the electron, the muon, and the tau all carry the same charge of $-e$. The electron is the only stable one of these three particles. All leptons can only interact via gravity, the electromagnetic and the weak force. The strong force only couples to the 6 quarks. Each family of quarks consists of one quark with a charge of $+\frac{2}{3}e$ and one with a charge of $-\frac{1}{3}e$. Unlike the leptons, quarks cannot be observed as free particles. They have been observed in deep inelastic scattering experiments as pointlike constituents of the nucleons, which were called partons. Later these partons were identified with the quarks proposed by Gell-Mann [GM64] and Zweig [Zwe64a, Zwe64b] in 1964, to understand the multitude of experimentlly known hadrons.

The standard model is known to be incomplete, e.g. it is not possible to describe gravitation within the same formalism as the other three fundamental forces. Also,

Family	Particle		Charge	Mass
1	quarks	u	$\frac{2}{3}e$	$1.5 - 3.3$ MeV
		d	$-\frac{1}{3}e$	$3.5 - 6.0$ MeV
	leptons	e	$-1e$	0.511 MeV
		ν_e	0	$< 2\ e$V
2	quarks	s	$-\frac{1}{3}e$	104^{+26}_{-34} MeV
		c	$\frac{2}{3}e$	$31.27^{+0.07}_{-0.11}$ GeV
	leptons	μ	$-1e$	105.66 MeV
		ν_μ	0	< 0.19 MeV
3	quarks	b	$-\frac{1}{3}e$	$4.20^{+0.17}_{-0.07}$ GeV
		t	$\frac{2}{3}e$	171.2 ± 2.1 GeV
	leptons	τ	$-1e$	1776.84 MeV
		ν_τ	0	< 18.2 MeV

Table 2.1: The fundamental fermions of the Standard Model. Properties are quoted according to [Ams08].

it does not make predictions for the mass of the neutrinos. Therefore, alternatives and extensions of the Standard Model are explored, which would allow overcoming these shortcomings.

One of the crucial tests is the search for the Higgs boson, which is expected to be discovered at the Large Hadron Collider, provided its existance in the mass range predicted by the Standard Model. This gauge boson is needed to explain the masses of the other elementary particles within the framework of the standard model.

The LHC results may also allow the discrimination between predictions of the Standard Model and those of other models, e.g. Super-Symmetric (SUSY) theories, some of which even predict multiple Higgs bosons.

2.2   Quark Confinement

Quarks carry one of three colors – red, green, or blue – with the respective anti-colors for anti-quarks. Eight gluons, each carrying a color and an anti-color, are needed to facilitate all possible transitions of the color charge.

The introduction of color as an additional property is necessary to retain the validity of the Pauli principle for particles like the Δ^{++} which consists of 3 u-quarks with parallel spin [Pov06]. However, no free object carrying a color charge has been observed. To account for this, it has been postulated in QCD that each free particle

has to be color neutral and that quarks can therefore not be observed individually. This postulate is one of main properties of QCD and referred to as color-confinement. The known color-neutral objects are either mesons, consisting of a quark and an anti-quark, or baryons, which contain 3 quarks, all of them having different color charges, so that in both cases the resulting hadron is color-neutral.

A phenomenological illustration of this color confinement can be given by the commonly used quark-antiquark potential [Per00]:

$$V_S = -\frac{4}{3}\frac{\alpha_s}{r} + kr \tag{2.1}$$

The first term, which is dominant at small distances, is similar to the Coulomb potential of the electromagnetic interaction. The second term increases linearly with the distance r of the original two quarks. Once the energy described by this term is large enough, a new $q\bar{q}$-pair is created to avert the creation of single quarks.

QCD is a SU(3) gauge theory for which the coupling α_s depends on the momentum transfer Q. $\alpha_s(Q^2)$ is therefore often referred to as a *running coupling constant*, similarly to the coupling constant of the electromagnetic interaction α_{em}. While α_{em} increases slowly with growing Q^2, α_s shows a different behavior. An important difference between the electromagnetic and the strong interaction is that unlike photons, gluons are carriers of the charge they couple to and thereby interact with each other. The coupling constant can be written as:

$$\alpha_s(Q^2) = \frac{12\pi}{(33 - 2n_f)\ln(Q^2/\Lambda^2)} \tag{2.2}$$

The number of participating quark flavors is determined by the available energy characterized by Q^2. The parameter Λ has to be determined by comparing QCD predictions to experimental results and is commonly given as $\Lambda \approx 250 MeV/c$ [Pov06, Ams08]. The Q-dependence of α_s reproduces the phenomenologically determined behavior of quarks: For small values of Q, the coupling increases so that the quarks cannot be separated. This is described as quark confinement. For large values of Q, which correspond to small distances or high energies, α_s asymptotically vanishes. This case is called *asymptotic freedom.*

2.3   QCD Phase Transitions

QCD predicts two general types of phase transitions: The restoration of chiral sym-metry and a transition from hadronic matter to a quark-gluon plasma (QGP). The restoration of the chiral symmetry is predicted to occur at high temperatures or high

densities. In this case the Hamiltonian of the Goldstone bosons, which can be iden-
tified with the lightest mesons, e.g. the pions, is subject to an additional symmetry.
This may be observed as a modification of the mass and width of the light mesons,
because QCD allows the description of all observables in terms of expansions of the
pion mass [Bur00, Yag05].

In this thesis, the focus will be on the effect of the second phase transition, the
transition to a quark-gluon plasma. In such a state, quarks and gluons can interact
freely over a significantly larger volume than the one of a nucleon.

It is assumed that shortly after the Big Bang the available partons formed a
quark-gluon plasma before the formation of hadronic matter took place. The under-
standing of this state is therefore important for the understanding of the evolution
of the universe. The examination of a deconfined state also allows improving the
theoretical description of the strong interaction and testing of QCD predictions.
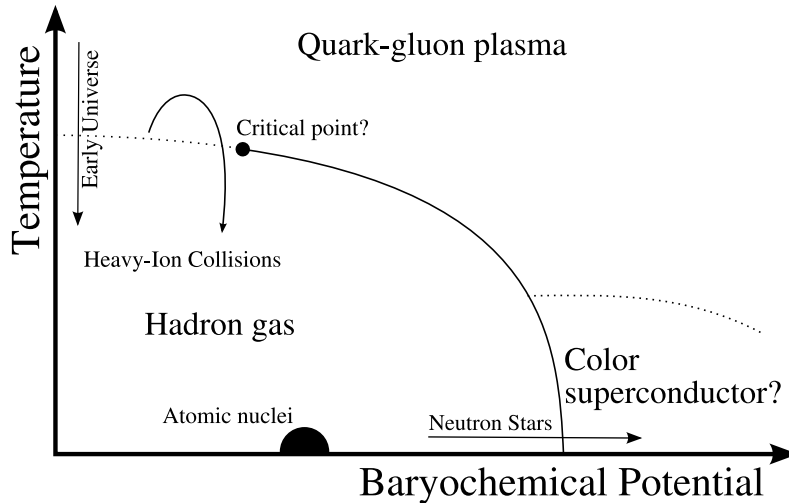
Figure 2.1: Schematic illustration of the phase diagram of strongly interacting matter.

An illustration of the phase transition from ordinary hadronic matter to a QGP
is shown in Figure 2.1. The phase diagram illustrates the two extreme cases in which
the creation of a QGP is possible.

The existence of a QGP was first considered for the case of low temperatures
and high densities in 1975 [Col75]. For this scenario a transistion from a hadronic
phase and to a QGP is expected to occur. Such conditions are assumed to exist in
neutron stars.

In the other extreme, at high temperatures and low net baryon densities, the
existence of a QGP was proposed in 1980 by Shuryak [Shu80]. Such a state can be

created in ultra-relativistic heavy-ion collisions, which is the common experimental approach to create a quark-gluon plasma in accelerator experiments.

One open question is the order of the phase transition. For high densities and low temperatures a first order transition is expected, while the phase transition at high temperatures and low densities may be a cross-over. This would imply the existence of a critical point in the phase diagram.

Several signatures are proposed to constitute evidence for the production of a QGP prior to hadronization in an experiment. None of these alone can be regarded as evidence for the creation of a QGP, but only the parallel observation of different signatures. They are discussed in Chapter 2.6.

2.4   Ultra-Relativistic Collisions

Collisions of heavy nuclei at high center-of-mass energies have been used for more than twenty years in experiments trying to create a quark-gluon plasma. The large amount of particles created in such collisions, when compared to p+p collisions, promises to be sufficient to create the energy densities necessary for the creation of a QGP.

The first experiments with ultra-relativistic heavy-ion collisions were carried out at center-of-mass energies of up to $\sqrt{s_{\mathrm{NN}}} = 5$ GeV at the AGS in Brookhaven and at the CERN-SPS with center-of-mass energies of up to $\sqrt{s_{\mathrm{NN}}} = 17.4$ GeV. The Relativistic Heavy Ion Collider at the BNL delivers collisions up to $\sqrt{s_{\mathrm{NN}}} = 200$ GeV for heavy ions. 2008, the LHC started its operation and will deliver Pb+Pb collisions up to $\sqrt{s_{\mathrm{NN}}} = 5.5$ TeV. The planned FAIR accelerator at the GSI will deliver a comparatively low center-of-mass energy of 8 GeV, with the aim to study matter at high baryon densities.

At the highest currently available energies for $\sqrt{s_{\mathrm{NN}}} \gtrsim 100$ GeV, a resulting QGP would have a very low baryon density, as the colliding nucleons can be regarded as nearly transparent for each other. The conditions of a QGP in such collisions would be comparable to those after the Big Bang (although, naturally, on a much smaller scale). At energies of $\sqrt{s_{\mathrm{NN}}} \approx 10$ GeV, the stopping of the colliding baryons is much more pronounced, leading to higher baryonic densities at the freeze out. The variation of the center-of-mass energy therefore allows the search for a possible critical point [Won94, Sen06].

In order to study nucleus-nucleus collisions and to understand possible medium effects, a baseline needs to be established. p+p collisions allow the observation of basic scattering processes without additional influences from a hot and dense medium or the surrounding cold matter. The total cross section for p+p collisions

for 10 GeV $\lesssim \sqrt{s_{\text{NN}}} \lesssim$ 1000 GeV shows only little dependence on the collision energy. Elastic scattering processes, which do not change the total kinetic energy of the incident particle, therefore do not contribute to the particle production in the collision. Inelastic scattering processes, however, in which the energy lost by the incident particles is mainly transformed into newly created particles, dominate the total cross section. At beam energies of 100 GeV/c, the cross section is $\sigma_{inel}(p+p) \approx 30mb$ [Ams08].

The mean number of charged particles produced in a collision can be described by simple relation to the center-of-mass energy [Won94, Tho77]:

$$\langle N_{ch} \rangle = 0.88 + 0.44 \ln s + 0.118 (\ln s)^2.$$

Most of the particles produced in such inelastic collisions are pions. The total number of particles can be estimated by assuming that only pions are produced in the collision and that π^+, π^- and π^0's are produced in equal abundance. The average total number of particles can then be derived from the measurement of charged particles emitted in these collisions:

$$\langle N_{total} \rangle = \frac{3}{2} \langle N_{ch} \rangle.$$

Most particles are produced in so-called soft processes. They are characterized by a small energy loss of the incident particle. For $p_{\text{T}} < 1$ GeV/c, these processes dominate, with $\langle p_{\text{T}} \rangle \approx 0.3$ GeV/c. Perturbative solutions of QCD are not applicable in this energy regime. When extrapolating the p_{T} spectra from this so-called soft region to $p_{\text{T}} \gtrsim 2$ GeV/c , the high-p_{T} results are usually underestimated. At these transverse momenta, the collisions are characterized by a high momentum transfer Q^2 compared to the QCD energy scale. This deviation was an early evidence of hard parton-parton scattering [Jac80].

These hard processes can be described by perturbative QCD (pQCD) calculations. A common approach is to factorize the cross section into the parton distribution functions of the colliding particles or nuclei, a fragmentation function and an interaction term describing the strong interaction.

The inclusive cross section for the production of a hadron h can be written in next-to-leading-order (NLO) pQCD as [Aur00]

$$\frac{d\sigma^h}{dp_{\text{T}} d\eta} = \sum_{i,j,k=q,g} \int dx_1 dx_2 F_{i/h_1}(x_1, M) F_{i/h_2}(x_2, M) \quad \frac{dz}{z^2} D_k^h(z, M_F)$$

$$\times \left[\left(\frac{\alpha_2(\mu)}{2\pi} \right)^2 \frac{d\hat{\sigma}_{ij,k}}{dp_{\text{T}} d\eta} \left(\frac{\alpha_2(\mu)}{2\pi} \right)^3 K_{ij,k}(\mu, M, M_F) \right]. \qquad (2.3)$$

The initial state of the colliding hadrons is represented by the parton distribution functions (PDFs) F_{i/h_n}, which have to be determined experimentally from deep inelastic scattering experiments [Ams08]. For the purpose of pQCD calculations, sets of fits to these measurements are provided by different groups [Gro09].

The fragmentation of a parton k into a hadron h is described by the fragmentation function (FF) $D_k^h(z, M_F)$. This can be derived from fits to spectra of a given hadron species, similar to the PDFs. Empirically determined sets of fragmentation functions are available [Rad09, Kni00, Kre00, Bou01, Alb08, Ams08]. For prompt photons, which are produced in initial hard parton-parton scattering processes, this term becomes a δ-function.

The scattering cross-section is given here in NLO, where $\hat{\sigma}_{ij,k}$ is the Born cross section for gives process $i + j \rightarrow k + X$, the $K_{ij,k}(\mu, M, M_F)$ term introduces the higher order corrections.

The factorization scale M, and M_F for the final state as well as the renormalization scale μ can be chosen arbitrarily, which introduces large uncertainties, especially for low transverse momenta. Commonly these scales are set to $M = M_F = \mu = p_\mathrm{T}$ and then varied with values between $p_\mathrm{T}/2$ to $2p_\mathrm{T}$ to estimate the uncertainty.

2.5 Space-Time Evolution of a Heavy Ion Collision

Ultrarelativistic heavy-ion collisions allow the creation of a state with high energy densities. From state-of-the-art lattice calculations critical temperatures in the range $T_C \approx 160 - 190$ MeV for the phase transition into a quark-gluon plasma can be obtained, which corresponds to an energy densitiy $\epsilon_C \approx 1$ GeV/fm^3 [Aok09, Yag05].

An estimate for the energy density ϵ_0 achievable in central heavy-ion collisions can be obtained from the Bjorken formula

$$\epsilon_0 = \frac{1}{\pi R^2 \tau_0} \left. \frac{dE_\mathrm{T}}{dy} \right|_{y=0}$$

where R is the radius of the overlapping area of the colliding nuclei, τ is the initial time for the creation of a thermalized medium, usually assumed to be 1 fm/c and $\left. \frac{dE_\mathrm{T}}{dy} \right|_{y=0}$ is the average transverse energy measured at midrapidity [Won94]. From the measurement of charged particle multiplicities and the transverse energy, it could be shown that the critical energy densitiy for a QGP formation is already reached in collisions of light ions, as oxygen and sulfur, at SPS.

In an ultrarelativistic heavy-ion collision, the colliding nuclei are Lorentz contracted along their flight path. The thickness along this axis for a nucleus with

the radius R is given by $2R/\gamma_{cm}$ with $\gamma_{cm} = E_{cm}/2m_N$, where E_{cm} is the center-of-mass energy of the collision and m_N the nucleus mass. Highest energy densities can be achieved in collisions, where the nuclei fully overlap, so-called central collisions. The centrality is usually described by the impact parameter b, which is illustrated in Figure 2.2. As the de Broglie wavelength of the nucleons is small in ultrarelativistic collisions, the nucleons can be classified into two categories: the nucleons in the overlap region are designated as *participants*, the nucleons outside of this area are called *spectators*. In a basic picture, the spectators leave the interaction region without suffering interactions, while the participants undergo binary nucleon-nucleon collisions.
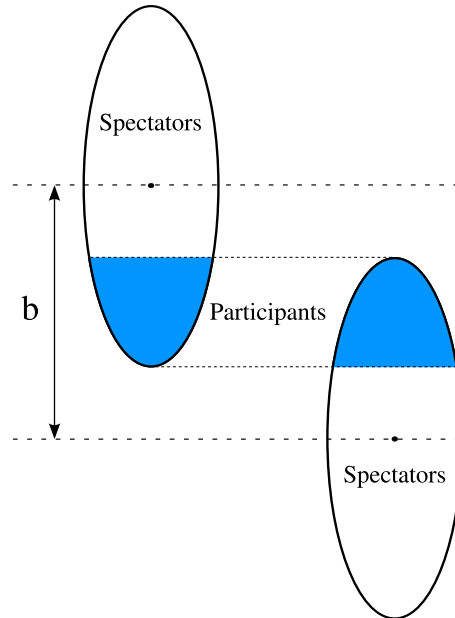
Figure 2.2: Illustration of the impact parameter b, which reflects the distance between the centers of the colliding nuclei. The overlap region of the collision is shaded. The nucleons inside this region are called *participants*, those outside are *spectators*.

Figure 2.3 shows a schematic depiction of the space-time evolution of the medium created in the collison.

For $\sqrt{s_{\mathrm{NN}}} \lesssim 10 GeV$, the Landau picture of nucleus-nucleus collisions can be applied [Yag05]. In this picture, the colliding nucleons are stopped. This creates a hot and baryon rich region, which subsequently undergoes hydrodynamic expansion. Here, the production of secondary particles occurs. At higher center-of-mass energies, the Bjorken picture can be applied to characterize the system created in
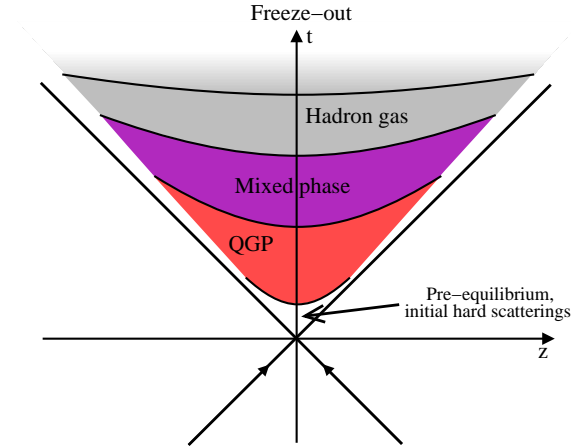
Figure 2.3: Schematic view of the space-time evolution of an ultrarelativistic nucleon-nucleon collision [KB04].

the collision. Unlike in the Landau picture, the colliding nucleons are not stopped. In the Bjorken picture, the wee quarks and gluons, which carry in summary a large fraction of the energy of the nucleon, form an excited state with low baryon density in the overlap region. The decoherence time τ_{de} necessary for these virtual particles to decay into real quarks and gluons is part of the pre-equilibrium stage of the medium created in the collision. After the creation of real quarks and gluons, these particles strive for thermal equilibration. The exact mechanism of this thermalization is still an open issue. Different mechanisms are under discussion [Yag05]. The thermally equilibrated phase, which is the phase commonly regarded as the quark-gluon plasma, expands hydrodynamically. Recent results from the RHIC experiments suggest that the expansion of this state shows properties similar to a perfect liquid. While the temperature decreases, the phase transition from a quark-gluon plasma to a hot hadron gas (HHG) is expected to occur. For this gas, two stages of freeze-out are expected: chemical freeze-out, after which the composition of particle species is fixed, since no more inelastic collisions occur, and the thermal freeze-out after which the kinetic equilibrium is no longer maintained, because no more elastic collisions between the created particles take place. [Won94, Yag05].

Different theoretical approaches are utilized to understand the properties of a quark-gluon plasma.

Basic estimates can be derived using few assumptions like in the MIT bag model [Cho74]: In this model it is assumed that quarks and gluons inside a bag with a radius R are massless and have infinite masses outside of this bag. The con-

finement is modeled phenomenologically by assuming a pressure B directed from the outside of the bag towards the inside. This bag pressure is counteracted by the energy of the confined quarks and gluons on the inside. For a given radius R, the bag pressure constant B, for which this model of hadrons with N quarks is stable, is given by:

$$B^{\frac{1}{4}} = \left(\frac{2.04N}{4\pi} \right)^{\frac{1}{4}} \frac{1}{R}.$$

The pressure P of a quark-gluon plasma, in which quarks, antiquarks, and gluons could be regarded as free particles, at a temperature T is given by

$$P = 37 \frac{\pi^2}{90} T^4.$$

For the critical temperature T_C the results in

$$T_C = \left(\frac{90}{37\pi^2} \right)^{\frac{1}{4}} B^{\frac{1}{4}}.$$

For a typical hadron radius of $R = 0.8$ fm Equation 2.5 yields $B^{\frac{1}{4}} = 206$ MeV, which results in a critical temperature $T_C = 144$ MeV [Won94].

Precise results from pure QCD calculations can currently not be derived due to technical difficulties imposed by the non-linear nature of this theory.

Lattice QCD (LQCD) calculations, which have been used to obtain the estimate of the critical temperature at the beginning of this section, are an important tool to understand this state of matter in the framework of the QCD. In LQCD, space and time are discretized, which allows the examination of non-perturbative features of QCD. While first calculations assumed quarks to be massless, current calculations are carried out for more realistic quark masses. Recent LQCD results are able to describe various physical observables with good accuracy and e.g. allow drawing conclusions on the nature of the phase transition and on the existence of a critical point, although the extrapolation for the light quark masses still contain large uncertainties [Jan08, Phi08].

2.6   Signatures of the Quark-Gluon Plasma

There is no signature of the quark-gluon plasma proposed so far that would by itself allow concluding the creation of this state of matter. Only the parallel observation of many different signatures can give evidence for the creation of a QGP.

In 2000, the CERN announced the discovery of a *"new state of matter in heavy ion collisions at the SPS"* that *"features many of the characteristics of the theoretically*

predicted quark-gluon plasma" [Hei00], based on the evaluation of the data collected by the different experiments. The next major milestone in the search for the QGP was the publication of 4 *white-papers* from the RHIC experiments, summarizing the findings from the first three years of RHIC data [Ada05, Adc05, Ars05, Bac05]. From these results, the creation of a new state of matter was deduced. Due to unexpected properties, like the similarity to a perfect fluid, which was not predicted by theoretical models for a quark-gluon plasma available at that time, the discovery of the QGP has so far not been explicitly claimed.

In the following, a short overview over important signatures of the quark-gluon plasma is given. The two signatures relevant for this thesis – suppression of particles with high transverse momentum and direct photon production – are discussed in more detail in Sections 2.7 and 2.8.

Possible signatures of the QGP and their experimental evidence have been reviewed frequently, e.g. [Gyu05, BM07, Ull08]

As explained above, global observables, like the rapidity distribution of the charged particles, allow the determination of the initial temperature of the medium created in heavy-ion collisions. For SPS and RHIC data, the estimates are above the critical temperature $T_C \approx 160$ GeV [Yag05].

An enhancement in the production of strange particles from p+p to nucleus-nucleus collisions has been observed at SPS and RHIC. It is compatible with models for a QGP, which expect an enhanced yield due to thermal production and a possible chiral symmetry restoration. A more robust observable is the ratio of different particles species at chemical freeze-out. Using simple statistical models, it is possible to describe the data at SPS and RHIC energies with the assumption of a medium with a temperature $T \approx 170$ MeV [BM03, And09].

The size of the system at freeze-out can be determined from Hanbury-Brown-Twiss (HBT) analyses. By charting the correlation between particles of the same species, a size on the order of 5 fm was obtained. While the results from SPS are well understood, the sizes obtained from RHIC data show an unexpected tendency in the evolution of the expansion, also known as the "HBT puzzle". Recent improvements in theoretical models indicate that these inconsistencies may have been overcome [Pra09] and the data can be understood with models assuming a QGP.

In the hot and dense medium the dissociation of quarkonium states, e.g. the J/Ψ, is expected due to color screening. However, theoretical models not involving a QGP can also include mechanims leading to a suppression of the J/Ψ production in nuclear matter [Cap02, BM07]. These effects have to be disentangled to draw conclusions on the presence of a QGP. Results consistent with both scenarios habe been observed by different experiments at SPS and later also at RHIC, but which mech-

anisms are causing the observed suppression could so far not be identified. At LHC energies, however, $c\bar{c}$-pairs are produced abundantly in hard parton-parton scatterings during the early stage of the collision and recombine later. This effect may offset the suppression observed at lower center-of-mass energies and even lead to a net enhancement of the charmonium production from statistical production [BM09].

Another interesting observation was the enhancement of low mass di-leptons in A+A collisions when compared to p+p results observed first by the CERES collaboration. This enhancement is not fully understood today, but can be explained at least partically by the modification of meson masses in the created medium and contributions from thermally produced particles [Tse05].

Thermally produced photons are another proposed signature for the quark-gluon plasma. As photons do not interact strongly, they could serve as a clean probe of the early stage of the collision, but the measurement is very ambitious. An overview of the production mechanisms of photons in heavy-ion collisions is given in Section 2.8

The interaction of highly energetic particles with a created medium can be accessed with another observable: highly energetic quarks and gluons leaving the interaction zone create a spray of hadrons, called jets. In a hot and dense medium, strongly interacting particles like quarks and gluons lose energy. When compared to p+p collisions, the energy of jets is suppressed in A+A collisions due to energy loss of the initially created parton in the medium. This so-called jet-quenching can be probed by different signatures like the suppression of particles with high transverse momentum, the vanishing of back-to-back correlations and modifications of the jet shape and momentum distribution. Jet-quenching is discussed in detail in Chapter 2.7.

The observation of elliptic flow, the anisotropy of particle momenta with respect to the reaction plane, which can be defined by the direction of the beam and the centers of the colliding nuclei, allows the assessment of hydrodynamic properties of the medium. Due to the almond-shape of the overlap region of the two colliding nuclei, particles with high transverse momentum emerging in transverse direction with respect to the reaction plane travel longer distances in the medium, thereby losing more momentum on average than particles emerging in the reaction plane. Particles with low energies are influenced by the pressure gradient caused by shape of the overlapping volume, which leads to an enhanced yield in the reaction plane. These effects can be quantified via the second coefficient of the Fourier decomposition of the angular distribution at a given p_T, the v_2. Experimental results can be described by hydrodynamic calculations thereby constraining the hydrodynamic properties of the created medium [Sor09].

2.7 Jet quenching

In proton-proton collisions, jets were first observed in the 1970s. The measurement of two narrowly collimated sprays of hadrons in opposite directions gave direct evidence for the existence of quarks: quarks and gluons from the collisions fragment into the vacuum. As they are produced in pairs, jets appear in azimuthal back to back collisions [Jac78, Jac79, Bro79, Cor79, Cla79, Arn83].

The suppression of these jets in heavy ion collisions due to energy loss in the created medium has been proposed as one of the earliest signatures for a quark-gluon plasma [Bjo82]: in such a hot and dense state a parton is expected to interact with the medium and to lose energy in hard parton-parton interactions, thereby reducing the total energy of the jet into which this parton fragments in comparison to a parton that has only a short pathlength within the medium before hadronization as shown in Figure 2.4. Different observables are accessible experimentally to measure this energy loss: the suppression of particles with high-p_T and the modification of the jet shape, either in measurements of single jets or in hadron-hadron correlations at high-p_T [d'E09].
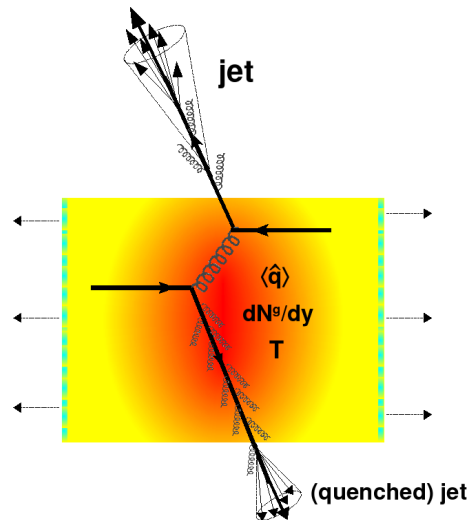

Figure 2.4: Schematic view of partonic energy loss in a QGP [d'E09].

2.7.1 Suppression of high-p_T particles

The suppression of particles with high p_T can be quantified relative to a p+p reference. While partons produced in p+p collisions fragment directly into the QCD-vacuum, partons produced in heavy ion collisions are expected to pass through a

hot and dense state of matter, where they lose energy. For particles with high momenta, the energy loss mechanisms are dominated by radiative energy losses, mainly by medium-induced gluon radiation processes. When fragmenting into hadrons, they carry on average a lower energy than expected from p+p collisions due to this in-medium energy loss [Vit06a]

The nuclear modification factor R_{AA} is commonly used to quantify the relation between nucleus-nucleus and proton-proton collisions:

$$R_{AA} = \frac{1}{N_{coll,AA}} \cdot \frac{dN_{AA}/(dp_T dy)}{dN_{pp}/(dp_T dy)}$$

where $dN_X/(dp_T dy)$ is the fractional yield for A+A and p+p collisions respectively and $N_{coll,AA}$ the number of binary parton-parton collisions. This is usually determined from Glauber simulations. An R_{AA} compatible with unity indicates, in a basic picture, that the production mechanisms for high p_T particles in p+p and A+A collision are the same and can be understood via simple scaling using the number of colliding nucleons. This is only valid for hard processes, which dominate the spectra for $p_T \gtrsim 2$ GeV. For lower p_T, where soft processes dominate particle production, the nuclear modification factor is expected to increase with p_T. At these momenta a scaling with the number of participants N_{part} is expected.

An R_{AA} below unity, however, would indicate a suppression of the high-p_T particle production in A+A collisions.

The nuclear modification factor is often also calculated with a p+A reference as R'_{AA} or, through comparison between central and peripheral collisions, as R_{cp}. By defining cuts on global characteristics of an event from simulations, its centrality can be classified. The number of binary nucleon-nucleon collisions of the reference has to be taken into account in these two cases:

$$R'_{AA} = \frac{N_{coll,pA}}{N_{coll,AA}} \cdot \frac{dN_{AA}/(dp_T dy)}{dN_{pA}/(dp_T dy)}$$

$$R_{cp} = \frac{N_{coll,AA,peri}}{N_{coll,AA,cent}} \cdot \frac{dN_{AA,cent}/(dp_T dy)}{dN_{AA,peri}/(dp_T dy)}.$$

Due to effects of Cold Nuclear Matter, which are discussed in the next section, the results may differ from the R_{AA} and allow conclusions on the presence of medium effects like jet quenching.

2.7.2   Effects of Cold Nuclear Matter

It can be argued that the comparison between nucleus-nucleus and proton-proton collisions alone is not sufficient to identify a suppression signal in the nuclear modification factor with jet-quenching, as the influence of Cold Nuclear Matter (CNM)

may not have been properly accounted for. Nuclei and protons are, for instance, described by different Parton Distribution Functions. This difference may have an impact on the nuclear modification factor. Comparisons, not only to p+p but also to p+A collisions, can be used to quantify these effects.

An especially important effect is the influence of the Cronin enhancement, which has been discovered in the comparison of particle yields from collisions of protons with different nuclei [Cro75, Ant79]. The cross sections for the production of different particles could be parameterized by the function

$$\frac{Ed^3\sigma}{dp^3}(p_\mathrm{T}, A) = \frac{Ed^3\sigma}{dp^3}(p_\mathrm{T}, 1) \cdot A^{\alpha(p_\mathrm{T})}.$$

For the lowest p_T, an exponent $\alpha \approx 0.7$ was expected, since in the soft regime the particle cross section is predicted to scale proportional to the cross section of the nucleus with $A^{2/3}$. For high p_T, where hard scattering processes dominate, the exponent is predicted to be constant at $\alpha = 1$. While the data reproduces the expected behaviour at low p_T, α significantly exceeds unity for higher p_T, as shown in Figure 2.5.

This behaviour is commonly explained with multiple soft scatterings of the incident nucleons, which broaden the transverse momentum distribution. When calculating the nuclear modification factor for p+A collisions with a p+p reference from Equation 2.7.1, often referred to as R_{pA}, it exhibits an enhancement above unity, typically for 1 GeV $< p_\mathrm{T} <$ 3 GeV [Ant79].

This enhancement can counteract a possible suppression signal owing to jet-quenching. The relative magnitudes are not known a priori and have to be determined from measurements.

The first experimental confirmation of jet quenching was reported in 2001 by the PHENIX collaboration [Adc02]. A detailed assessment of the available experimental results on jet quenching in heavy ion collisions is given in Chapter 3.1.

2.7.3 Medium Modification of Jets

The measurement of particle correlations allows an even more direct access to the influence of the medium on the jet energy. In the analysis, a highly energetic hadron, the leading hadron, defines the direction of the jet. For this particle the difference in the azimuthal angle for other highly energetic hadrons in the same event is determined. In p+p and d+Au collisions two peaks at 0° and 180° are visible, as shown in Figure 2.6, which can be understood by the back-to-back correlations of partons created in hard collisions. In Au+Au collisions the variation of the p_T interval of the associated hadrons reveals a rich structure: at low p_T, the back-side
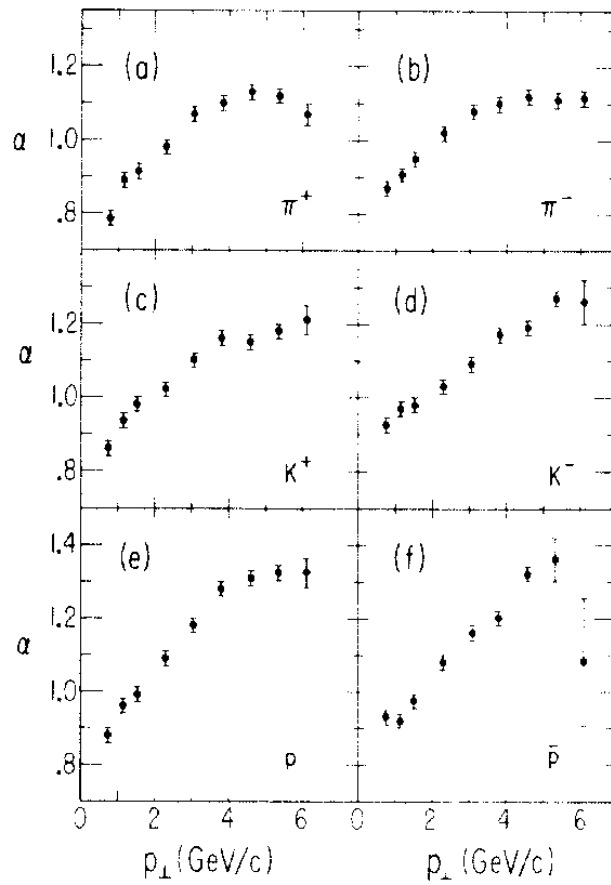
Figure 2.5: Original observation of the so-called Cronin enhancement [Cro75]. For high p_T, α is expected to asymptotically reach unity, if it scales with the number of nucleons. The deviation indicates the presence of a previously unaccounted nuclear effect.

peak at $\phi = 180°$ is significantly broadened compared to the p+p measurement. For higher p_T the backside peak exhibits a dip at the center, which can be interpreted as a medium response to the energy loss of the initial parton. Interestingly, the peak reappears at the highest associated p_T. This is commonly regarded as a punch-through of the parton through the medium [Adl03a, Hor07, Ada08a].
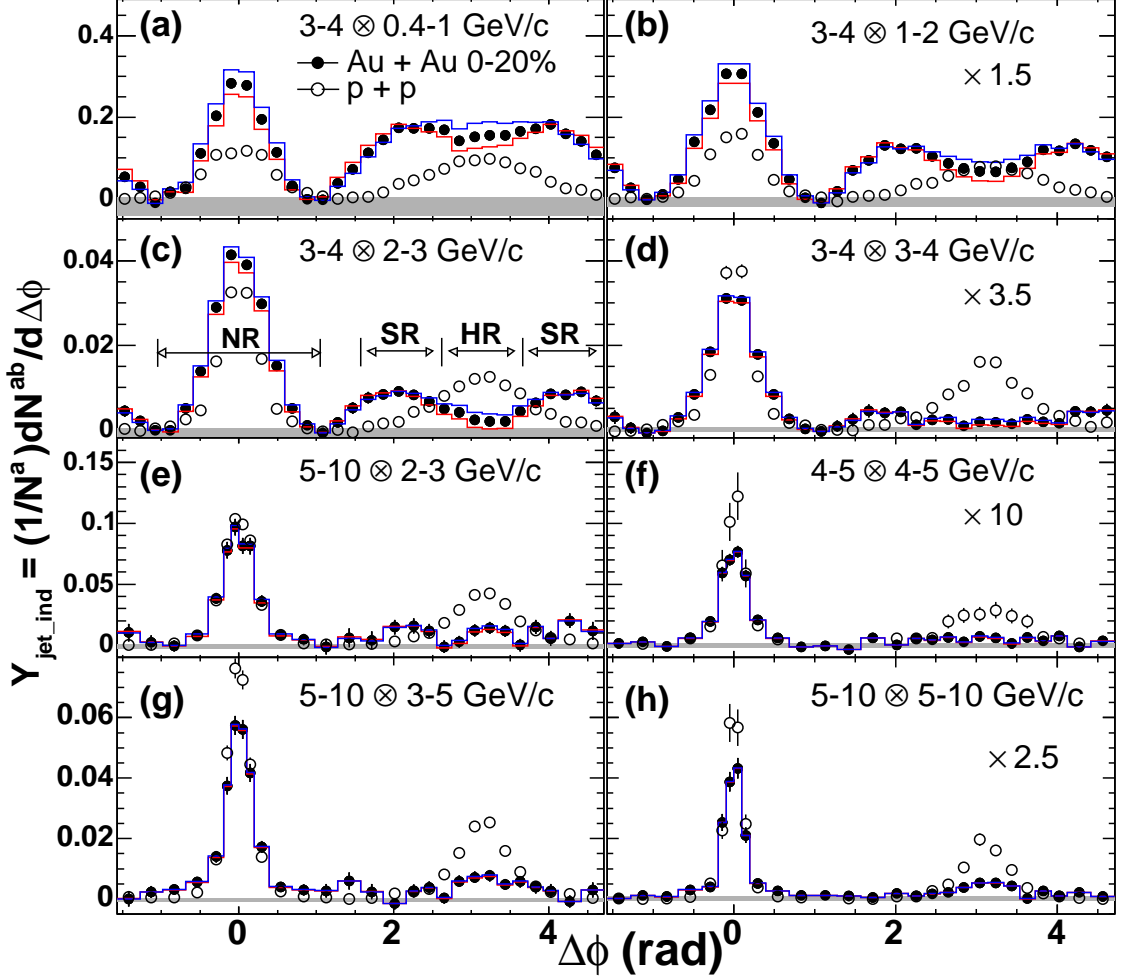
Figure 2.6: Azimuthal correlation of charged hadrons in p+p and central Au+Au collisions measured by PHENIX for different p_T-intervals [Ada08a]. In the upper right corner of each panel, the ranges for the trigger p_T and the partner p_T are given.

A two-dimensional analysis of the correlation in the $\Delta\Phi - \Delta\eta$-plane shows a ridge-like structure of the associated hadrons along $\Delta\eta$. This observation and its explanation by theoretical models is a subject of ongoing research [Bie09a].

2.8   Direct Photons

Photons are produced during all stages of a heavy-ion collision. Typically, photons are subdivided into photons from hadronic decays and photons produced by other mechanisms, which are summarized as direct photons.

Photons produced in the early stage of the collisions in hard parton-parton scatterings are referred to as *prompt direct photons*. The measurement of *thermal direct photons* may allow experimental access to a thermally equilibrated phase created during the collision. Other sources of direct photons are the pre-equilibrium phase of the medium and medium-jet interactions [Cha09].

Since photons only interact via the electromagnetic force, they can leave the interaction zone virtually unmodified. This makes them an ideal probe for the different stages of the collision. The measurement is experimentally challenging, since the contribution of decay photons dominates photon production in ultrarelativistic collisions.

Furthermore, the different production mechanisms of direct photons cannot be separated experimentally. Theoretical calculations and baseline measurements in p+A and p+p collisions are needed to quantify the individual contributions.

The different production mechanisms of direct photons and common approaches for the measurement of direct photons are discussed in the following sections, a review of the available experimental results is given in Chapter 3.2. Detailed discussions of existing results and theoretical calculations can, e.g., be found in [Ala96, Pei02, Gal03, Sta05, Cha09, Tse09, Gal09]

2.8.1   Production of Non-Thermal Direct Photons

Prompt Photons

Prompt photons are created in hard scattering processes during the initial stage of the collision. pQCD calculations have successfully described the spectra of $p + p$ and $p + \bar{p}$ spectra from the SPS energy regime up to energies of about 2 TeV. The Feynman graphs for the leading order, as shown in Figure 2.7, are quark-gluon compton scattering, quark-antiquark annihilation and quark fragmentation. When including Next to Leading Order terms (NLO), the terms are typically separated into a direct or prompt contribution from annhilation and Compton scattering, which also accounts for relevant higher order contributions, and a fragmentation contribution [Aur06].

In nucleus-nucleus collisions, additional effects like the different z-component of the isospins of neutrons and protons, coherence effects that may be prevalent
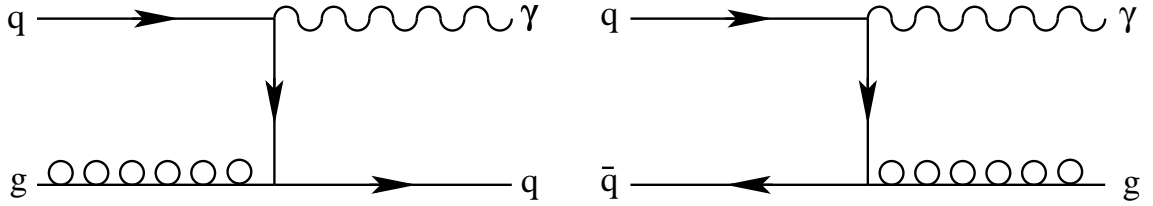
Figure 2.7: Feynman graphs in leading order pQCD for prompt photons [Pei02]. In addition, the corresponding cross-terms not shown here have to be taken into account [Ell96].
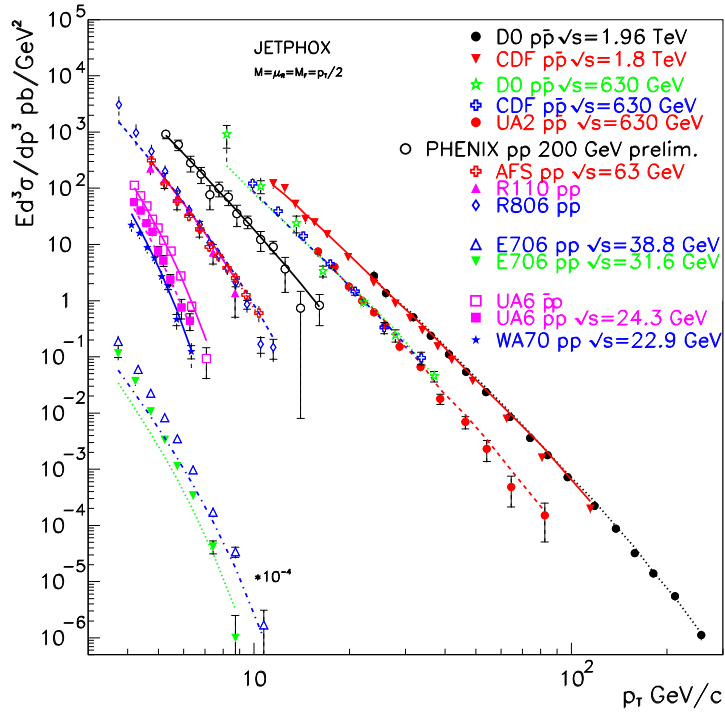
Figure 2.8: Comparison of pQCD calculations to measured direct photon cross section from $p + p$ and $p + \bar{p}$ collisions from the SPS to the Tevatron energy regime. Except the results from E706, all data sets are described reasonably with a common scale of $\mu = p_T/2$ [Aur06].

in a Color Glass Condensate [Ian02] or the EMC effect [Gee95] could lead to a deviation from the assumption of scaling with the binary nucleon-nucleon collisions. Experimental results are needed to constrain these possible effects. The same holds true for proton-nucleus collisions, where e.g. the Cronin enhancement discussed above may lead to an enhancement of photon production when compared to results from proton-proton collisons

2.8.2   Production of Thermal Photons

The thermal production of photons has been one of the earliest signatures proposed for the QGP. It has long been assumed that the production of photons from a QGP dominates over other sources.

In 1991, calculations by Kapusta, Lichard and Seibert showed that photon production in a Hot Hadron Gas (HHG) does not differ significantly from that in a QGP, when both are at the same temperature [Kap91]. While the theoretical formalism is similar for the calculation of the photon rate, the large number of hadrons and possible decay channels makes a precise calculation of the hadron gas contribution difficult.

A further complication in the separation of these two competing mechanisms arises from the fact that after the chemical freeze-out of the QGP an HHG is expected to be created. If a QGP is created, the thermal signal will be superimposed on the thermal signal from a HHG. Figure 2.9 shows the expected thermal photon signal and the contributions from the different thermal contributions [Tur04]. Over the full p_{T} range, the thermal photon yield from a QGP is significantly below the total photon yield from a hadron gas. With accurate measurements of the p_{T} dependence of the thermal photon production it may therefore be possible to identify a contribution from a QGP.

2.8.3   Additional Mechanisms of Photon Production

Other sources of photons also need to be considered, e.g. the production during the pre-equilibrium stage, where different theoretical models are employed and the interaction of jets with the medium, which may lead to the production of direct photons. While theoretical models can incorporate these processes, the precision of the available data is not sufficient to allow any conclusions on the influence of these effects [Sta05, Cha09].
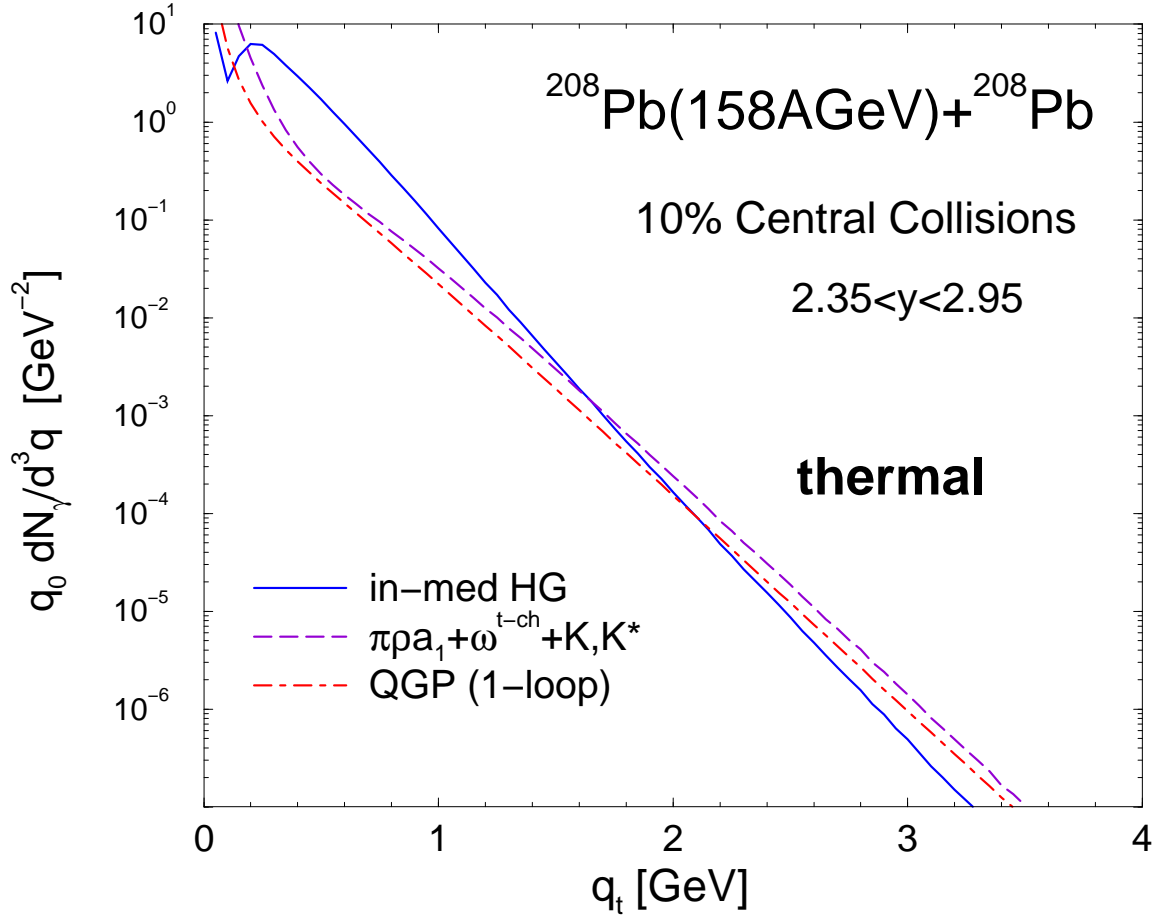
Figure 2.9: Direct Photon production at SPS energy. The plot shows the expected photon rate from a QGP and different contributions to a Hadron Gas. Over the full p_T range, the QGP rate is significantly below the total rate of the Hadron Gas [Tur04].

2.8.4   Experimental Techniques

Different techniques have been developed and employed to measure direct photon spectra.

Perhaps the most straightforward approach is the measurement of photons with electromagnetic calorimeters. This technique is employed in the analysis presented in this thesis and is described in detail in Chapter 6. In principle, all photons are measured with calorimeters. Veto detectors are used to reject contributions from charged particles. The contribution of photons from particle decays is then subtracted to obtain the direct photon spectrum.

The measurement of dileptons also allows obtaining results on direct photon production by exploiting photon conversions: The external conversion method uses a converter to enhance the conversion rate for photons in a defined location. This can either be a dedicated component or a part of the experimental setup, in fixed target experiments often the target itself fulfills this purpose. The electron-positron pairs from photon conversions are narrowly collimated. By setting rigid constraints on the distance of the two particles in the detector, photons can be reconstructed.

Any source of photons also creates virtual photons. The mass of the corresponding electron-positron pair is typically much smaller than the mass of the mother particle. In order to obtain the fraction of direct photons with respect to the total photon yield, the contribution of dileptons from hadron decays has to be subtracted. Typically, the shape of the two invariant mass distributions from virtual photons and hadron decays is determined from simulations and matched to the measured invariant mass distribution at very low invariant masses, where the shape of the two is very similar. The measured invariant mass spectrum is then fitted to the sum of the two parameterizations in a region, where the shape of the two contributions deviates significantly. The only free parameter is the relative magnitude of the hadronic and the photonic component. From this parameter the contribution from direct photons can be obtained.

The Hanbury-Brown-Twiss interferometry (HBT) allows the measurement of direct photons at very low p_{T}, where the other analyses are obscured by the large background from hadronic decays. The measurement exploits the Bose-Einstein correlation of photon pairs from the interaction region. The correlation strength can be used to identify direct photons.

Other analysis methods include, e.g. tagging methods or the correlation of hadron-jets with photons or of two photons.

3. Previous Results

In this thesis results concerning the suppression of single hadrons and direct photons in heavy ion collisions are presented. This chapter gives a summary of previous findings on these two quantities and highlights open questions that still need to be addressed experimentally.

3.1 High-p_T Suppression of Single Hadrons

Following the initial idea of jet quenching as signature for the QGP in 1982 [Bjo82], significant efforts to discover jet quenching at the SPS were undertaken. However, during the running of the SPS program no conclusive results were obtained [Wan98]. Hence, the suppression of particles with high transverse momenta was also not one of the signatures included in the CERN press release of 2000, which announced the discovery of a hot and dense state of matter [Hei00].

First experimental evidence for jet quenching was found at RHIC by the PHENIX and STAR experiments in 2001 in Au+Au collisions at $\sqrt{s_\mathrm{NN}} = 130$ GeV [Adc02, Adl02]. Until today, RHIC experiments have established the suppression of high-p_T particles for different hadron species in the range 62.4 GeV $\leq \sqrt{s_\mathrm{NN}} \leq 200$ GeV for different colliding nuclei. The interpretation of a suppressed nuclear modification factor as an indication for energy loss in a medium was supported by PHENIX, when comparing R_{AA} of hadrons to the R_{AA} of direct photons (Figure 3.1). Since photons do not interact via the strong force, they do not exhibit a suppression.

However, recent results from Au+Au collisions at $\sqrt{s_\mathrm{NN}} = 200$ GeV show a tendency for the nuclear modification factor of photons towards values below unity at the highest measured p_T, as shown in Figure 3.2. This does not necessarily imply a suppression of photons due to jet quenching in the created medium. It may also be explained by other mechanisms like isospin effects, the EMC effect or the suppression of fragmentation photons. Recent preliminary results from Cu+Cu collisions at the same center-of-mass energy do not exhibit such a reduction of the R_{AA} for direct photons. The exact interpretation of these observations and the identification of contributing effects is a matter of current research [Arl07, Vit08].

Neutral Pions and η mesons produced in central Au+Au collisions at $\sqrt{s_\mathrm{NN}} = 200$ GeV exhibit a suppression by about a factor of 5. Recent measurements by the PHENIX experiment indicate that other mesons, e.g. the ω and the ϕ, show a less pronounced suppression. The mechanisms for this have not been fully understood
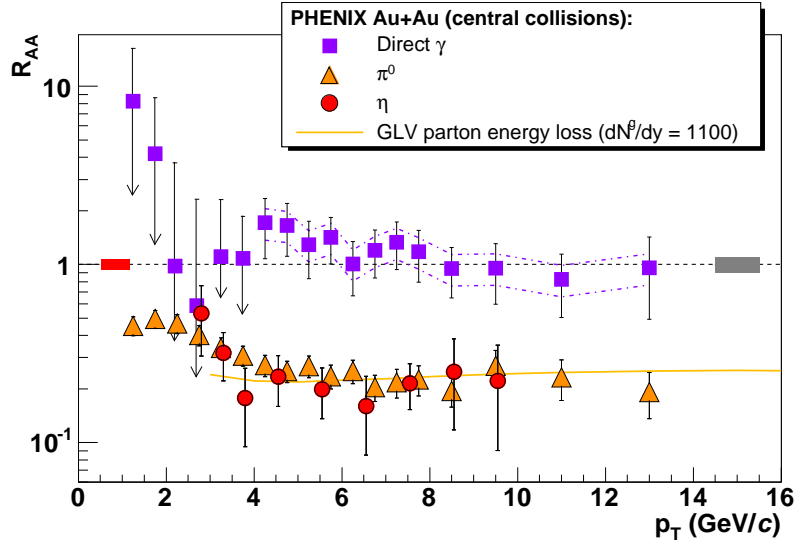
Figure 3.1: The nuclear modification factor for neutral pions, η-mesons and direct photons, measured by PHENIX in Au+Au collisions with a proton reference at $\sqrt{s_{\mathrm{NN}}} = 200$ GeV [Adl06].

yet and are again an object of ongoing research [Rey08]. The nuclear modification factor for hadrons decreases smoothly for increasingly central collisions. In the comparison of the suppression signal for different colliding species, it was found that the magnitude of the suppression depends solely on the number of participating nucleons N_{part} [KB08]. In order to determine the energy of the onset of jet quenching, RHIC has collided gold nuclei at center-of-mass energies of $62.4, 130$, and 200 GeV. The suppression at 130 GeV and at 200 GeV was comparable, at 62.4 GeV which is consistent with the suppression observed at higher center-of-mass energy for the highest $p_{\mathrm{T}} \approx 6$ GeV/c [KB08].

The STAR [Ada03b, Abe07] and the BRAHMS [Ars03, Ars04, Ars07] collaboration have reported results on the nuclear modificaton factor which are consistent with the PHENIX findings mentioned above.

The discovery of jet quenching at RHIC has triggered efforts to re-evaluate the earlier SPS results [d'E05, d'E04, Blu07]. Nuclear modification factors were obtained or could be derived from results of WA98, NA49, NA45/CERES and NA57 for different hadron species and are discussed in the following.

The WA98 collaboration has presented results on the production of neutral pions in Pb+Pb collisions at $\sqrt{s_{\mathrm{NN}}} = 17.3$ GeV [Agg02] and employed two methods to quantify a possible suppression signal: The comparison between the yields in
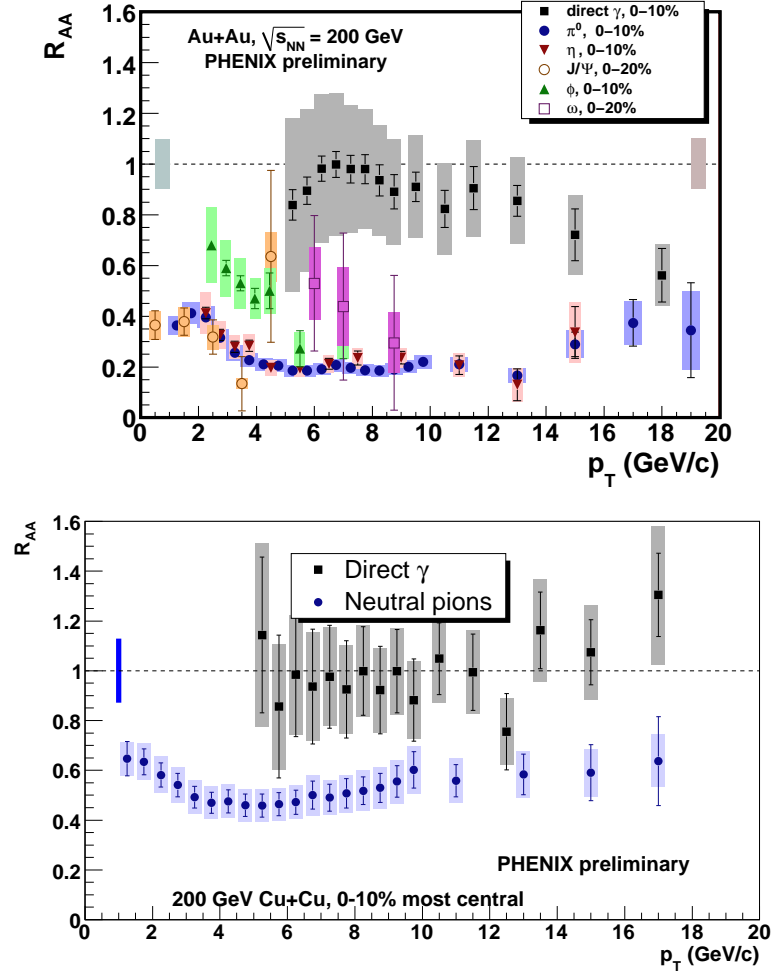
Figure 3.2: The upper panel shows the available preliminary measurements of the nuclear modification factor of different species in Au+Au collisions at $\sqrt{s_{NN}} = 200$ GeV by PHENIX [Rey08]. The nuclear modification factor for direct photons and neutral pions in Cu+Cu collisions at $\sqrt{s_{NN}} = 200$ GeV is shown in the lower panel [Sah09].

central and peripheral Pb+Pb collisions (R_{cp}) and the comparison of the neutral pion yield from central Pb+Pb collisions to a parameterization of neutral pion measurements in p+p collisions at higher center-of-mass energies scaled to the WA98 center-of-mass energy. The R_{cp} has large uncertainties and shows large fluctuations. Although the nuclear modification factor is higher with a more reference from more peripheral Pb+Pb collisions, the data slightly favor a signal below unity, as shown in Figure 3.3 [Rey02]. To obtain a p+p reference, available results on the neutral-pion production at $\sqrt{s_{NN}} \approx 19$ GeV were fitted, since no data were avail-
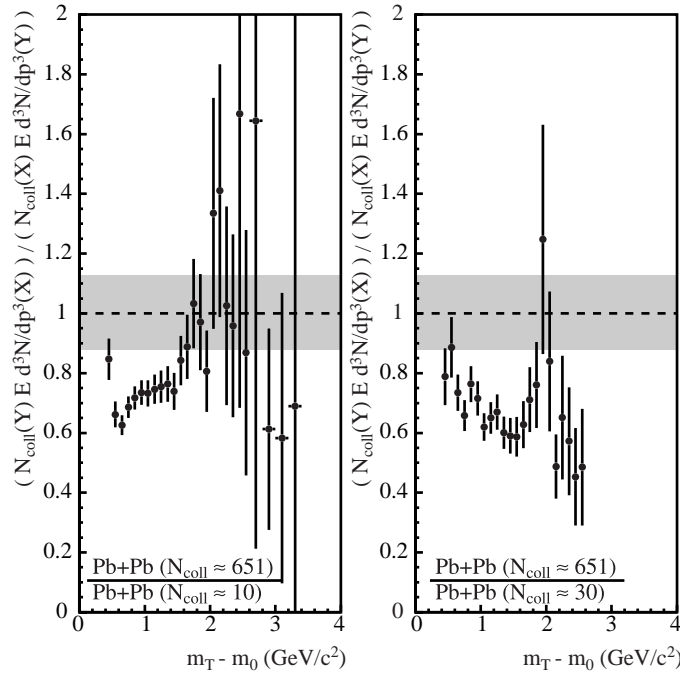
Figure 3.3: R_{cp} of neutral pions in Pb+Pb collisions measured by WA98 for two different centrality combinations. Although the R_{cp} is consistent with unity within errors, a tendency towards a suppression is visible [Agg02].

able at exactly the same center-of-mass energy. To correct for this, x_T-scaling was applied [Owe87, Blu98]. Using this reference a strong enhancement of the nuclear modification factor was observed (Figure 3.4). Due to the contradicting results
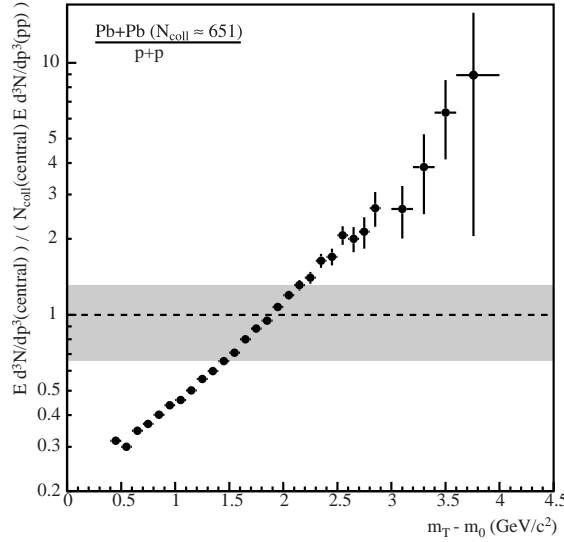
Figure 3.4: The nuclear modification factor for neutral pions in Pb+Pb collisions at $\sqrt{s_{\text{NN}}}$ = 17.3 GeV, using a parameterization of p+A and p+p measurements at $\sqrt{s_{\text{NN}}} \approx 19$ GeV, scaled to the WA98 energy by applying x_T-scaling, as reference. The nuclear modification factor with this reference exhibits a strong enhancement [Agg02].

of the two approaches, no definite conclusions on a possible suppression could be drawn.

The NA49 experiment has measured the production of different charged hadron species in Pb+Pb, p+C and p+p collisions at $\sqrt{s_{\text{NN}}}$ = 17.3 GeV [Alt06, Alt07, Alt08, Las08] as shown in Figure 3.5. The data for charged pions are limited to $p_T \lesssim 2.1$ GeV/c and thereby do not cover the region where hard scattering processes are dominant and jet quenching is expected to be most pronounced. Although the R'_{AA} with a p+C reference shows a signal below unity, it is significant only for $p_T < 2$ GeV/c, where N_{coll} scaling is not yet applicable. The shape of the result is consistent with results from PHENIX at these p_T. The p+p reference from NA49 has a slightly smaller p_T coverage compared to the Pb+Pb data, the R_{AA} is consistent with unity at the highest available $p_T \approx 2$ GeV/c, rising smoothly with increasing p_T. From the Pb+Pb data, a R_{cp} has also been calculated, the result is consistent with the R_{cp} obtained by WA98 for neutral pions within the uncertainties. NA49 has also obtained data for the production of $p/\bar{p}$ and $K^{+/-}$, the findings being
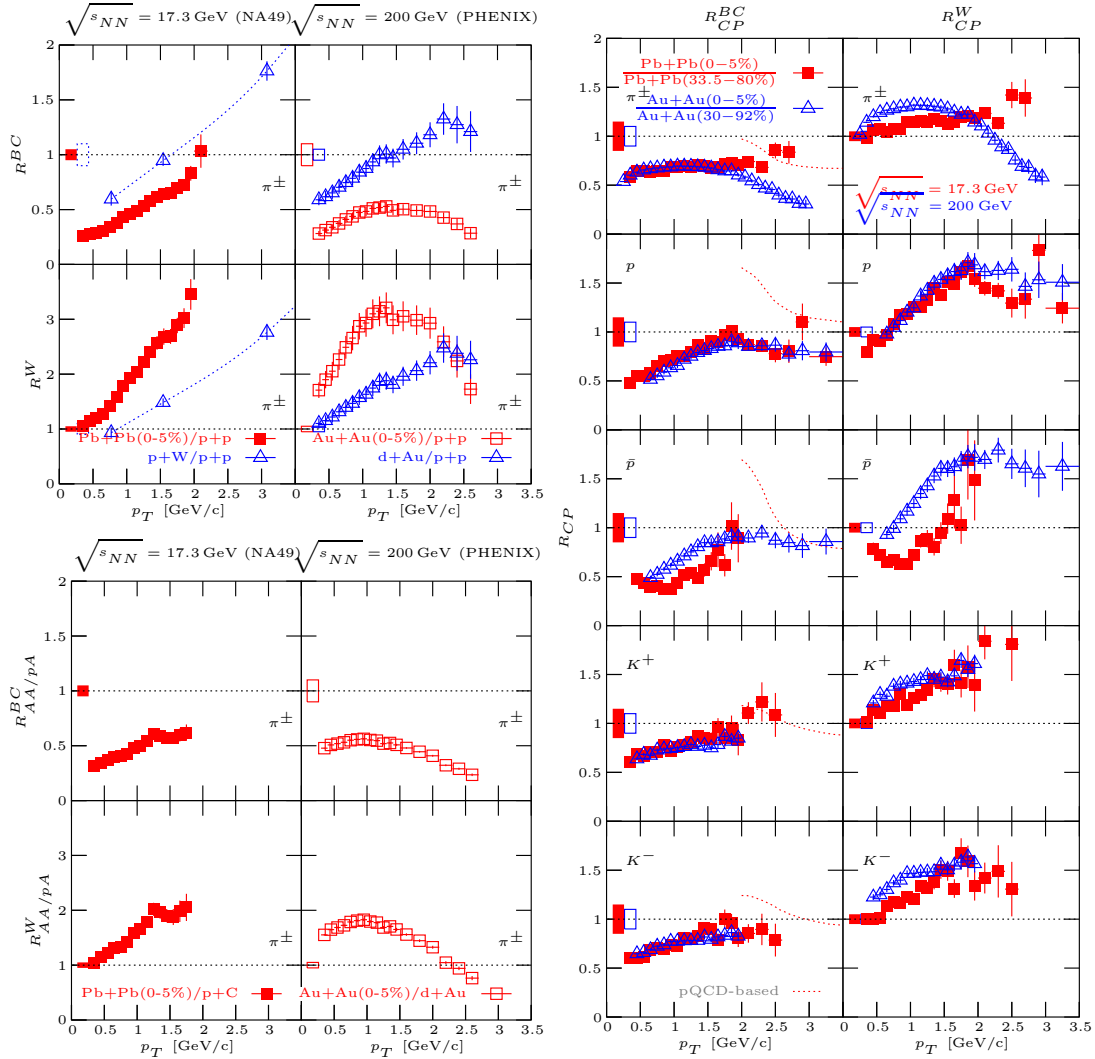
Figure 3.5: NA49 results on the nuclear modification factor. The R^{BC} ratios correspond to the nuclear modification factor as described in Chapter 2.7.1, the R^W ratios assume a scaling with N_{part} according to the *wounded nucleon model*, as described in [Bia08]. For all NA49 results a comparison to PHENIX results in Au+Au collisions at $\sqrt{s_{NN}} = 200$ GeV is given. The upper left panel shows the nuclear modification factor for central Pb+Pb collisions with a p+p reference for $p_T \lesssim 2$ GeV/c. The p+W data is taken from [Ant79]. The lower left panel uses a p+C reference to quantify the nuclear modification factor. Here the shape of the NA49 results and the PHENIX results from central Au+Au collisions is similar. The panel on the right shows the ratio of central to peripheral events for different particle types. Data for $p_T > 2$ GeV/c R_{cp}^{BC} are available for charged pions, protons and kaons [Las08].

compatible with results for charged pions but statistically less significant. In general, the significance of the NA49 results for the quantification of a high-p_T suppression is limited by the p_T coverage of the available data, which does not extend significantly into the region dominated by hard scattering processes.

NA45/CERES has published a result on the R_{cp} of charged pions in Pb+Au collisions at $\sqrt{s_\mathrm{NN}} = 17.3$ GeV for 1.3 GeV/$c < p_\mathrm{T} < 3.5$ GeV/c [Wur04, Sli03]. They find a moderate enhancement up to $R_{cp} \approx 1.5$ for the highest momenta, consistent with a moderate Cronin enhancement or Cronin enhancement offset by jet quenching (Figure 3.6). The R_{cp} is quoted from the ratio of the $0-5\%$ most central events to the $21-26\%$ most central events. The centrality selection used as reference was the most peripheral defined in the analysis, but it is not clear if influences from a possibly created hot and dense medium can already be neglected, making the interpretation of this result difficult. No p+p or p+A reference is available from NA45/CERES.
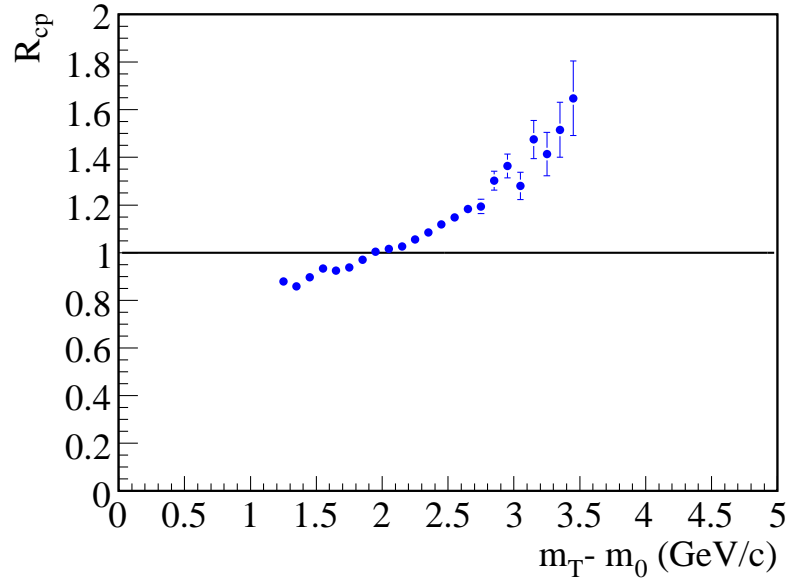
Figure 3.6: R_{cp} for the averaged production of charged pions in Pb+Au Collisions at $\sqrt{s_\mathrm{NN}} = 17.3$ GeV measured by CERES [Sli03, Bie09b]. The R_{cp} is calculated from the $0-5\%$ most central events to the $21-26\%$ most central events.

The NA57 collaboration measured the inclusive production of negatively charged hadrons (h^-), Λ and K_s^0. For these particles, the R_{cp} has been presented in [Ant05]. The data covers transverse momenta $p_\mathrm{T} < 4$ GeV/c for K_s^0 and Λ and $p_\mathrm{T} < 5$ GeV/c for the h^-. The R_{cp} shown in Figure 3.7 is compatible with unity for h^- and K_s^0,

the R_{cp} of the Λ shows a small enhancement. The data can be described best by models that include partonic energy loss scenarios.
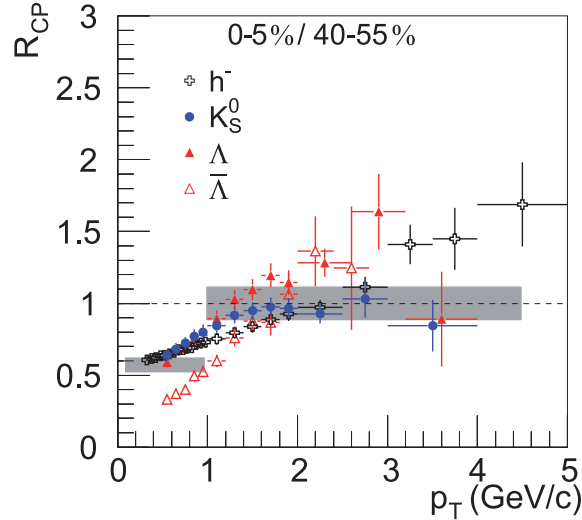
Figure 3.7: R_{cp} measured by NA57 for negatively charged hadrons, Λ and K_s^0 [Ant05]. The shaded band around $R_{cp} = 1$ indicates the uncertainty of the N_{coll} scaling, the band at low p_T indicates the expectation from N_{part} scaling in the soft regime with the associated uncertainty.

Again, from these measurements no conclusion on a possible influence of jet quenching at the top SPS energies can be drawn, while RHIC measurements have established the presence of this effect clearly for $\sqrt{s_{NN}} \geq 62.4$ GeV. Especially the lack of a measured p+p or p+A reference with a good coverage for $p_T \gtrsim 2$ GeV/c introduces large uncertainties, since parameterizations or data scaled from other center-of-mass energies have to be used.

The usage of R_{cp} as a replacement does not improve the situation: the results of the different SPS experiments, although largely consistent within errors, vary between a slight suppression as reported by WA98 and NA49 and a small enhancement as reported by the CERES collaboration. Additionally, it is not clear in how far cold nuclear matter effects may be relevant here.

In order to overcome the uncertainties in the p+p reference, d'Enterria [d'E04] has compared three parameterizations of the Lorentz-invariant cross section of neutral pions in p+p collisions to inclusive pion measurements in p+p collisions for 16.9 GeV $\leq \sqrt{s_{NN}} \leq 19.4$ GeV. The parameterization proposed by the WA98 collaboration in [Agg02] systematically underpredicts the available data at high transverse momenta and overpredicts it at low p_T. The parameterization by Wang and

Wang [Wan00, Wan01] shows an offset to the data of $\approx 50\%$. It is found that the parameterization by Blattnig et al. [Bla00] yields the best description of all available data, with a systematic uncertainty of 25%. Figure 3.8 shows in the upper panel the R_{AA} for central Pb+Pb collisions with each of the three parameterizations taken as a reference. The WA98 and the Wang and Wang parameterization lead to a strong enhancement of the nuclear modification factor for high $p_{\rm T}$, while the Blattnig parameterization yields a much flatter R_{AA}, which is consistent with unity. In the lower panel, the R_{AA} for pions from central events measured by WA80, WA98 and CERES is shown using the Blattnig parameterization as a reference. All three data sets agree with unity within errors. The light shaded band indicates the prediction from theoretical calculations including energy loss in a hot medium and enhancement processes from the Cronin effect. The experimental results agree, within errors, with this calculation. Although no significant suppression has been observed, this provides evidence for the presence of jet-quenching already at SPS energies and underlines the need for a measured p+p or p+A reference with large $p_{\rm T}$ coverage at $\sqrt{s_{\rm NN}} = 17.3$ GeV.

The uncertainty in the nuclear modification factor at the top-SPS energy for heavy-ions is emphasized, when the dependence of the nuclear modification factor on the center-of-mass energy is considered. Figure 3.9 shows two compilations of the R_{AA} [d'E05] and the R_{cp} [Blu07] as a function of the center-of-mass energy from SPS energies of $\sqrt{s_{\rm NN}} \approx 17$ GeV to the top-RHIC energy of 200 GeV. For both cases, a strong suppression is observed for the RHIC data with $\sqrt{s_{\rm NN}} \gtrsim 60$ GeV, while the SPS results deviate significantly. Moreover, the available data is not fully consistent within errors. It is not possible to differentiate between a suppression and an enhancement scenario.

In this thesis results on neutral pion production in p+Pb and p+C collisions at $\sqrt{s_{\rm NN}} = 17.3$ GeV are presented, which can serve as a baseline for the available results from heavy-ion collisions, as well as neutral pions from Cu+Cu collisions at 22 GeV measured by the PHENIX experiment, which allow to consistently portray the development of the nuclear modification factor from the SPS energy regime to top RHIC energies from data measured by one experiment.

3.2   Experimental Results on Direct Photon Production in Heavy-Ion Collisions

Already in the 1970s first evidence for the production of direct photons in proton-proton collisions was found [Dar76, Fer84]. Due to the higher event multiplicities and the large background from decay photons, the measurement of direct photons
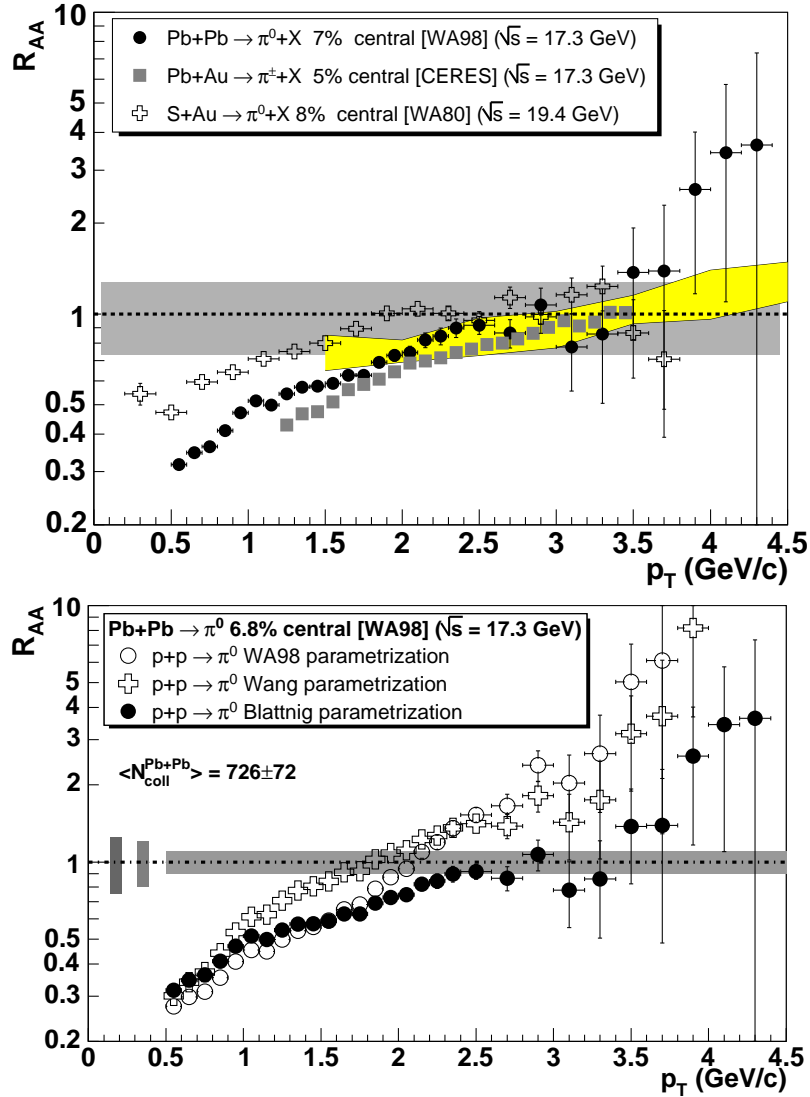
Figure 3.8: The lower panel shows the nuclear modification factor of neutral pions in central Pb+Pb events measured by WA98 with three different paramterizations. In the upper panel, the parameterization by Blattnig et.al. is used as a reference for the R_{AA} of pions measured by WA80, WA98 and CERES [d'E04].

in nucleus-nucleus collisions is a challenging task. The first significant result was reported by the WA98 collaboration in 2000 [Agg00b]. Since then the experimental efforts by SPS and RHIC experiments have been extensively reviewed [Pei02, Dre05, Rey05, Sta05, Fra07, Cha09]. In the following, a summary of the most important results obtained in nucleus-nucleus collisions is given.

The NA34/Helios collaboration measured the production of photons in collisions of p, O and S beams with Pt and W targets. The results were found to be consistent with expectations from decay photons, employing a conversion method for the
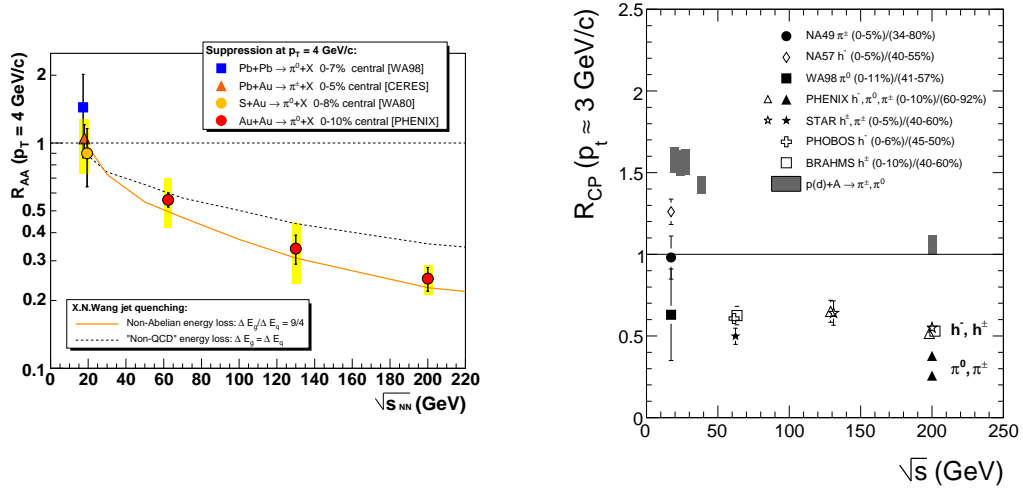
Figure 3.9: The nuclear modification factor from SPS to top RHIC energies is shown for central nucleus-nucleus collisions. For the SPS data at $\sqrt{s_{NN}} \approx 17$ GeV the reference from Blattnig et.al is used to compute the R_{AA}, model calculations different energy-loss mechanisms are shown [d'E05]. The right panel shows the R_{cp} in the same center-of-mass energy range [Blu07].

---

photon measurement [Ake90]. The collaboration did not report an upper limit of the data, but as argued in [Pei02, Sta05] it would be possible to infer such a limit from the reported results for inclusive photons and pions, integrated over the full p_T interval. However, such an upper limit would not lead to any new conclusions, since – due to the steepness of the spectra – it would essentially correspond to an upper limit for the lowest p_T interval.

CERES/NA45 has reported such upper limits on direct photon production in S+Au collisions. The results were obtained by reconstructing the photon momentum from measured electron-positron pairs with vanishing opening angle [Bau96, Kam97, Bau97]. With a confidence level of 90%, the contribution of direct photons to the integrated cross section in the interval 0.4 GeV/$c < p_T < 2.0$ GeV/c was limited to less than 14% of the inclusive photon yield.

The WA80 collaboration employed a lead-glass calorimeter for the detection of photons. From O+Au collisions, an integrated upper limit could be determined [Alb91]. The first p_T-dependent upper limit on direct photons produced in heavy-ion collisions was measured in S+Au collisions (see Figure 3.10) and allowed to derive constraints on theoretical models of photon production at high p_T [Alb96].

The significant direct photon signal measured by the WA98 collaboration in Pb+Pb collisions at $\sqrt{s_{NN}} = 17.3$ GeV is shown in Figure 3.11 [Agg00b, Agg00a].
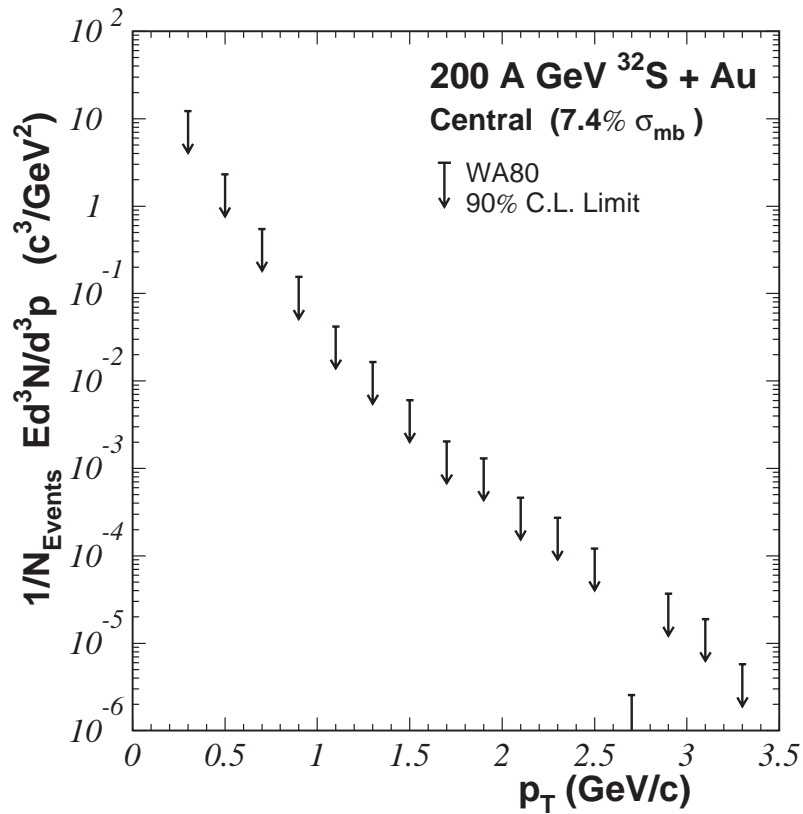
Figure 3.10: Upper limits on the direct photon production reported by the WA80 collaboration from measurements of central S+Au collisions [Pei02].

The extraction of a thermal contribution is one of the prime motivations for the measurement of direct photons in heavy-ion collisions (see Chapter 2.8.2). To quantify a cross section from thermal emission, a baseline from p+p or p+A measurements has to be established for quantitative comparisons. The best measurements available were taken at different center-of-mass energies. x_T-scaling was employed to compare them to the WA98 results. With the data-sets by E629, E704 and NA3, which were used as reference, it was not possible to discriminate an assumed thermal signal from the dominantly produced prompt direct photon contribution. Data points are available only for $p_T > 2.2$ GeV/c, thereby only partially covering the region where a thermal contribution to the cross section of photons is expected to be strongest. Additionally, the data sets exhibit strong fluctuations and the systematic uncertainty introduced by the x_T-scaling may have been underestimated, as the systematic comparison of parameterizations of neutral pion yields presented in the previous section indicates. Theoretical models, e.g. [Tur04], involving a thermal contribution from the QGP, describe the data very well. However, alternative models involving no thermal contribution from a QGP but e.g. k_T-broadening still cannot be ruled out. From peripheral Pb+Pb collisions upper limits on the direct photon production could be obtained by the WA98 collaboration, but again the significance of these results is not sufficient to further constrain theoretical models. WA98 has also reported the significant measurement of direct photons for $p_T < 0.5$ GeV employing HBT interferometry. These results cannot be fully described by the currently available theoretical models [Agg04].

PHENIX has measured real photons in Au+Au and Cu+Cu collisions at $\sqrt{s_{NN}} = 200$ GeV, whose relevance for the confirmation of N_{coll}-scaling has been discussed in Chapter 3.1. The search for a thermal contribution to the direct photon signal, also at these higher energies, is one of the main motivations for the measurement of direct photons. Calorimetric measurements in the low p_T region of $p_T \lesssim 5$ GeV/c, where a thermal signal is expected to be most pronounced [Tur04], are challenging, e.g. due to the large background of decay photons at these momenta. The available data from Au+Au [Adl05a], p+p [Adl05b, Adl07b] and preliminary results for d+Au [Bat07, Per07] collisions at $\sqrt{s_{NN}} = 200$ GeV do not allow conclusions to be drawn on a possible thermal contribution.

These difficulties can be overcome by the measurement of photons from internal conversions as described in Chapter 2.8.4. PHENIX has recently published first results with this method from Au+Au and p+p collisions at $\sqrt{s_{NN}} = 200$ GeV, shown in Figure 3.12, and reports an enhancement of direct-photon production in Au+Au collisions. This can be interpreted as evidence for a thermal photon signal in heavy-ion collisions [Ada08b].
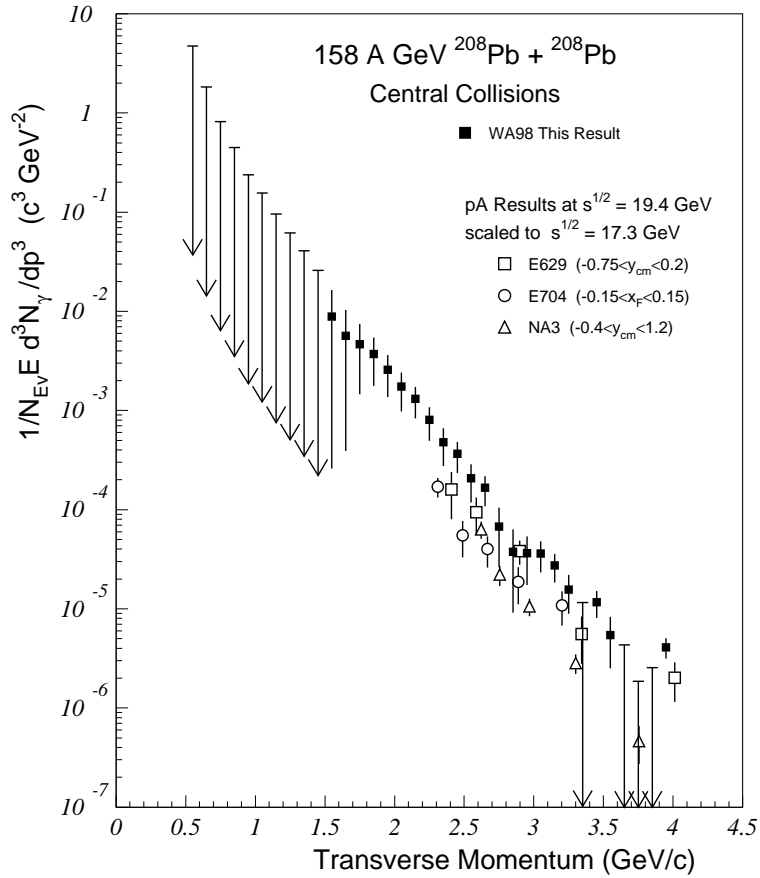
Figure 3.11: Direct photon yield measured by the WA98 collaboration in central Pb+Pb collisions at $\sqrt{s_{NN}} = 17.3$ GeV. The data is compared to results from p+p collisions at $\sqrt{s_{NN}} = 19.4$ GeV scaled to the SPS center-of-mass energy [Agg00b].
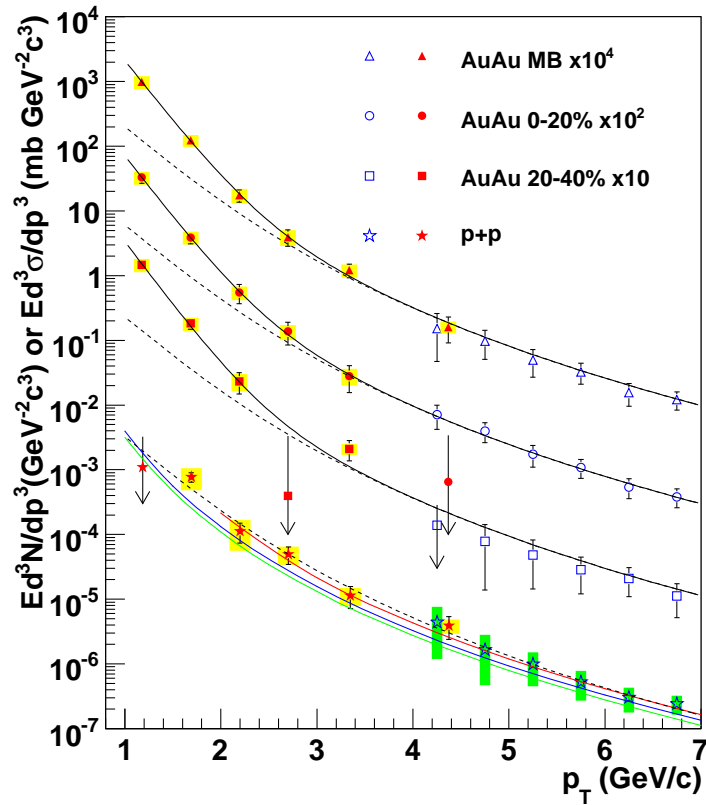
Figure 3.12: Measurement of direct photons by the PHENIX collaboration. The closed data points have been obtained by measuring di-lepton pairs from internal conversions.The full lines show the results of pQCD calculations, the dashed lines represent a fit to the p+p result scaled by T_{AA}. The measurements in Au+Au collisions exceed this expectation [Ada08b].

The STAR collaboration has recently presented first results on direct-photon production in p+p and d+Au collisions at $\sqrt{s_{\mathrm{NN}}} = 200$ GeV [Rus07a, Rus07b]. So far no results on a direct photon signal from nucleus-nucleus collisions have been reported by this experiment.

The small number of available significant direct photon yields from heavy ion collisions underlines the experimental difficulty of this measurement. Especially in light of the direct photon excess at low p_{T} reported recently by the PHENIX collaboration, the possibility of deriving constraints on the prompt direct photon production in Pb+Pb collisions at $\sqrt{s_{\mathrm{NN}}} = 17.4$ GeV from the available p+A data is discussed in this thesis.

4. Experimental Setup

For this thesis, data obtained with two heavy-ion experiments have been analyzed: the PHENIX experiment at the Brookhaven National Lab and the WA98 experiment, which was located at the CERN-SPS accelerator. In this chapter, these two experiments and the detector systems relevant for the analyses detailed in the following chapters will be described.

4.1 WA98

The WA98 experiment was proposed in 1991 [Ang91]. It was designed as a multi-purpose experiment for the detection of hadrons and photons. Two spectrometer arms were optimized for the measurement of charged hadrons, the electromagnetic calorimeter LEDA for the measurement of photons and hadrons with photonic decay channels, e.g. the π^0 and η mesons. A schematic view of the setup of the experiment during the 1996 data-taking period is given in Figure 4.1.

4.1.1 The SPS

The Super Proton Synchrotron (SPS) was designed for the acceleration of protons and has been upgraded to also deliver heavy-ion beams. Presently, the SPS mainly serves as injection accelerator for the LHC but is also still used for experiments which directly utilize the SPS beam.

In 1996, when the proton-induced collisions analyzed for this thesis were recorded, the SPS could accelerate lead ions up to a maximum beam energy of 158 GeV/c. Protons could be accelerated up to a beam energy of 450 GeV/c. The protons were created in a hydrogen plasma source and injected into the LINAC 2 accelerator, which accelerated the protons up to 50 MeV/c. After additional acceleration steps in the Proton Synchrotron Booster (PSB) and the Proton Synchrotron (PS), the protons were injected into the SPS with an energy of 28 GeV/c. They were subsequently accelerated to their maximum energy of 450 GeV/c. The ion beam was transferred to the western experimental area (WA) through the H3 beam line. In order to obtain a proton beam with an energy similar to that of the lead beam, the primary proton beam collided with a 500 mm thick beryllium target. For the data described here, the T1 target was used to obtain a secondary beam. This secondary beam contained a mixture of different particles distributed over a wide

WA98 Experimental Setup
158 A GeV Pb+Pb Collisions
at the CERN SPS
(1996)

highly segmented **Lead-Glass Calorimeter**
(identification of photons, π^0 and η -mesons)

Forward-Calorimeter

Had.-Calorimeter
(transverse energy)

highly segmented **Photon-Multiplicity-Detector**

Time of Flight (#2)
(PID of positive hadrons)

Streamer Tubes

Pad Chambers

Goliath Magnet

Target
(inside Plastic-Ball)

Start Counter

33 TeV Pb

Plastic-Ball
(π^+, p, ... He in target region)

Silicon-Pad and Silicon-Drift Detectors
(pseudorapidity-dist. of charged particles)

Charged Particle Veto-Detector

21.5 m

Time of Flight (#1)
(PID of negative hadrons)

Multistep Avalanche Chambers
with CCD-readout (tracking of charged particles)

Figure 4.1: Schematic overview of the WA98 setup for the data-taking period in 1996 [WA909].

CERN Accelerators

Figure 4.2: Schematic overview of the CERN accelerator facility[Car01, Ste98].

	Positively charged	Negatively charged
p	49.3%	1.2%
π	46.0%	93.4%
K	4.7%	5.4%

Table 4.1: Composition of the secondary beam created at the T1 target of 500 mm Beryllium under an angle of 0 mrad at the H3 beam line of the CERN SPS. The energy of the incident proton energy is 450 GeV/c, the selected energy of the secondary beam is 160 GeV/c [Ath80]. For the analysis presented here only the positively charged particles were selected.

range of energies. The exact composition depended on the energy of the incident primary beam, the angle between beam and target, as well as on the target material and thickness. Dipole and quadrupole magnets behind the target allowed the selection of the momentum and charge of the secondary particles and were used to focus this secondary beam [MC02, Ath80].

At the beam energy of 160 GeV/c selected for the data presented here, which was chosen to closely match the beam energy of the lead-beam run, the relative amount of protons and positively charged pions was nearly the same. The relative fractions of the particles in the secondary beam used during the WA98 PR96 run are shown in Table 4.1.

4.1.2   Setup of the WA98 Experiment

In this section, an overview of the WA98 setup is given, with a focus on the LEDA detector, mainly utilized for the analyses presented in this thesis.

The Targets

For the measurements during the proton beam-time in 1996 (PR96), ^{208}Pb and ^{12}C targets were used. Data was recorded for two different ^{208}Pb-targets with different areal densities, one ^{12}C-target and for reference purposes also without a target. The properties of the targets used are listed in Table 4.2. The targets were supported by a wheel-structure inside the Plastic Ball Detector described below, the wheel being able to hold up to 5 targets. For reference measurements of the interaction rate outside of the target described below, one of these positions was purposely left empty.

Target	thickness (mm)	areal density (mg/cm^2)
^{208}Pb	0.210	239
^{208}Pb	0.436	495
^{12}C	10.022	1879

Table 4.2: Properties of the targets used during the PR96-beamtime.

Central Detectors

The start trigger for the experiment was generated by Cherenkov counters positioned 3.5 m upstream of the target. With a time resolution of 27 ps, the Cherenkov counters could separate beam particles which other detectors would not be able to separate the resulting events for, and reject them to exclude pile-up events. They also served as a start trigger for the Time-of-Flight measurement in the hadron-spectrometer arms [Blu98]. For the p+Pb and p+C beam times, two additional Cherenkov counters positioned 21 m and 6.4 m upstream of the target were used for the identification of the beam particle. Each detector had an efficiency of 90% for the identification of pions. By requiring a coincidence of the two a efficiency of 99% could be obtained [MC02].

As muons from the halo of the beam can cause wrong start trigger decisions, two scintillator walls positioned before the target were used to reject them. The inner halo detector was positioned 4.7 m upstream of the target and consisted of ten scintillators, each 50 cm wide and 100 cm long. These were arranged end-to-end in a wall of 2×5 scintillators with the two scintillators in the middle positioned 32 cm apart to form an opening of 32×50 cm^2 for the beampipe. The outer halo detector was positioned 72 cm upstream of the inner halo detector. Two orthogonal layers of 4 scintillator strips, each 98 cm long and 12.5 cm wide, with a 6 cm hole in the middle for the beam pipe, formed this detector wall. An additional scintillation detector, the 'little veto', with a small opening for the beam was positioned 1.7 m upstream of the target to reject interactions in or behind the start trigger [Rey99].

The target itself was placed inside the Plastic Ball Detector [Bad82], which was designed for experiments at the Bevalac in Berkeley and was already part of the WA80 experiment, a predecessor experiment of WA98. The detector consisted of 655 $\Delta E - E$ telescopes which covered an angle of $30° \leq \theta \leq 160°$ corresponding to a pseudorapidity region of $-1.7 < \eta < 1.3$, the azimuthal angle was covered fully, it allowed the identification of protons, positively charged pions and fragments of the nucleus.

Directly behind the vacuum chamber of the target, two detectors for the measurement of charged particle multiplicities were installed: the Silicon Drift Detector

(SDD) and the Silicon Pad Multiplicity Detector (SPMD), both described in detail in [Ste98]: the SDD consisted of a single n-doped silicon wafer which covers the rapidity region of $2.0 < \eta < 3.4$ and was positioned 12.5 cm behind the target. Concentrical p-doped regions served as cathodes. They were connected via resistors acting as a voltage divider for the high voltage of $1600 - 2500$ V, which was applied between the cathodes and the 360 anodes on the outer border of the wafer. This voltage created a parabolic potential that let the electrons, created by charged particles traversing the detector, drift towards the outside with nearly constant velocity. From the charge distribution on the anodes and the drift time, a 2-dimensional resolution of up to 20 μm could be achieved.

The SPMD was positioned 32.8 cm downstream of the target. The circular detector was divided into 4 quadrants, each of which was made of a 300 μm thick n-doped silicon wafer. An implanted p-doped layer created a p-n junction to which a voltage of 50 V was applied to fully deplete the silicon. The detector was segmented into 4000 pads, which could be read out separately. These pads divided the azimuthal angle into 180 segments and the pseudorapidity into 22 rings. Each pad covered $\Delta\eta = 0.064$ and $\Delta\phi = 2°$. As the size of the pads changed in each ring, the probability for a hit was similar for all pads. The detection efficiency for charged particles was better than 99%, with a conversion probability of only 0.2%, such that the photon detectors are not significantly affected [Ste98].

The Charged Particle Veto detector (CPV) consisted of two sectors, each equipped with 86 Iarocci-type streamer tubes [Rey99]. It was positioned 1 m in front of the electromagnetic calorimeter and had the same acceptance. Charged particles created a localized discharge between the anode wire and the cathode, which induced a signal on externally mounted pads. The main purpose of this detector was to allow the rejection of hits in the electromagnetic calorimeter caused by charged particles.

The Photon Multiplicity Detector (PMD) was a so-called preshower detector, which uses lead plates with a thickness of 1.7 cm corresponding to 3 X_0 for photons, as converter material. The secondary particles were detected by 54000 scintillator tiles, which were read out by CCD cameras via wavelength shifting fibers. Hadrons and photons could be differentiated by their measured average pulse height. The PMD identified pulses with at least three times the height of a pulse from a minimum-ionizing particle as photons. This resulted in a detection probability for photons of 68% with a hadron contamination of 35% in central Pb+Pb collisions [Rey99].

The MIRAC calorimeter[1], covered the rapidity region $3.5 < \eta < 5.5$. The calorimeter had an electromagnetic component and a hadronic component, both featuring a sandwich structure. The electromagnetic part was constructed of alternating layers of lead and plastic scintillator, with a total thickness of 15.8 X_0. The hadronic part of alternating layers of iron and scintillators, with a depth of 6.1 hadronic interaction lengths. The measured resolution was $17.9\%/\sqrt{E}$ for electromagnetic showers and $46.1\%/\sqrt{E}$ for hadronic showers.

The Zero Degree Calorimeter (ZDC) detector comprised 35 modules each made of alternating layers of iron and scintillator material, similar to the MIRAC setup. The signal from hadronic showers was read out by photomultiplier tubes. It covered the rapidity region $\eta > 5.9$ and measured the energy of the projectiles and their fragments (spectators).

4.1.3   The Hadron Spectrometer Arms

The Goliath dipole magnet, which had a bending power of 1.6 Tm, was used to separate the charged particles at midrapidity and direct them towards the two hadron spectrometer arms of WA98 [Rey99]. The first arm measured negatively charged particles with 6 Multistep Avalanche Chambers (MSACs) and a Time-of-Flight (TOF) chamber. The second arm, which was added in 1996, employed two streamer tube planes, two MSAC planes, and a TOF plane. The MSACs in the first arm were read out using CCD cameras: charged particles passing through the chamber created free electrons. These were amplified by the strong electric field between parallel wire meshes, to which a high voltage was applied. The detector is filled with a neon-argon gas mixture, allowing an avalanche amplification of the initially created electrons. This avalanche caused the emission of UV-photons from Triethylamin (TEA) molecules added to the gas mixture. These photons were directed via mirrors to CCD cameras where they were detected. The position resolution of this device has been measured to be 3 mm. An approximately 8 m² large scintillator wall formed the TOF detector. In consisted of 480 plastic scintillators. They were read out at both ends and had a time resolution of 130 ps. Together with the start trigger, this detector can be used for the identification of charged particles.

The second arm different is equipped with MSACs of different design: charge-sensitive pads inside the gas volume were used for read-out, such that no addition of the toxic TEA to the gas mixture was necessary. The streamer tubes were based on the CPV streamer tubes, but had smaller read-out pads. The TOF in this arm had a time resolution of 80 ps.

---

[1]The MIRAC calorimeter was already part of the WA80 experiment. At the lower beam energies it had a different rapidity coverage, leading to its name MId RApidity Calorimeter

4.1.4   Trigger and Data Acquisition

The WA98 system has been optimized for the maximum data rate from all subsystems, although the different systems had significantly different read-out speeds. The detectors were therefore grouped in different trigger classes, which allowed read-out and triggering of the fast detectors more often than of the slower ones (see [Buc99]).

For this analysis, two trigger conditions are used: the basic minimum bias trigger condition was generated by a coincidence of the start trigger and the MIRAC, which required a minimum deposited energy. An additional trigger on photons with high p_{T} enriched rare events in the data sample. For normalisation purposes the number of beam particles passing the experiment with and without an inhibit from the DAQ has been recorded using a simple beam trigger.

The WA98 data acquisition (DAQ) framework recorded the data from the experiment in several steps: each detector was read out by a CPU working as subevent-builder, which buffered and aggregated the data in subevents. The subevent builders were read out at the end of a beam spill from the accelerator by the master-event-builder, which then assembled the full events and wrote them to DLT data tapes. The events were grouped into runs of 400 MB size. This corresponds to 7000-10000 events for the p+A data.

In an offline analysis, the raw data is converted into Column-Wise Ntuples that contain calibrated physical properties of the event. The so-called HBOOK files were originally analyzed using the HBOOK libraries [HBO09] or PAW [Paw09]. For the purpose of this analyses presented in this thesis, they have been converted into data files for the C++ based ROOT-analysis framework [Roo09].

4.1.5   The Lead-Glass Calorimeter

The WA98 Lead-Glass Calorimeter (LEDA) was designed to be later employed as part of the PHENIX calorimeter, which lead to a modular setup. LEDA consisted of 10080 lead-glass modules read out by photomultipliers. To allow an easy reconfiguration of the setup, the modules have been assembled into supermodules of 6×4 modules as shown in Figure 4.3.   Each module was wrapped in alumnized Mylar foil to prevent optical crosstalk between adjacent modules. Each supermodule was equipped with LEDs that simulated the Cherenkov light produced by highly energetic particles and allowed monitoring of the energy calibration over extended periods of time. The light intensity of the LEDs was monitored by photo diodes. A detailed description of this detector and its calibration is given in [Blu98].
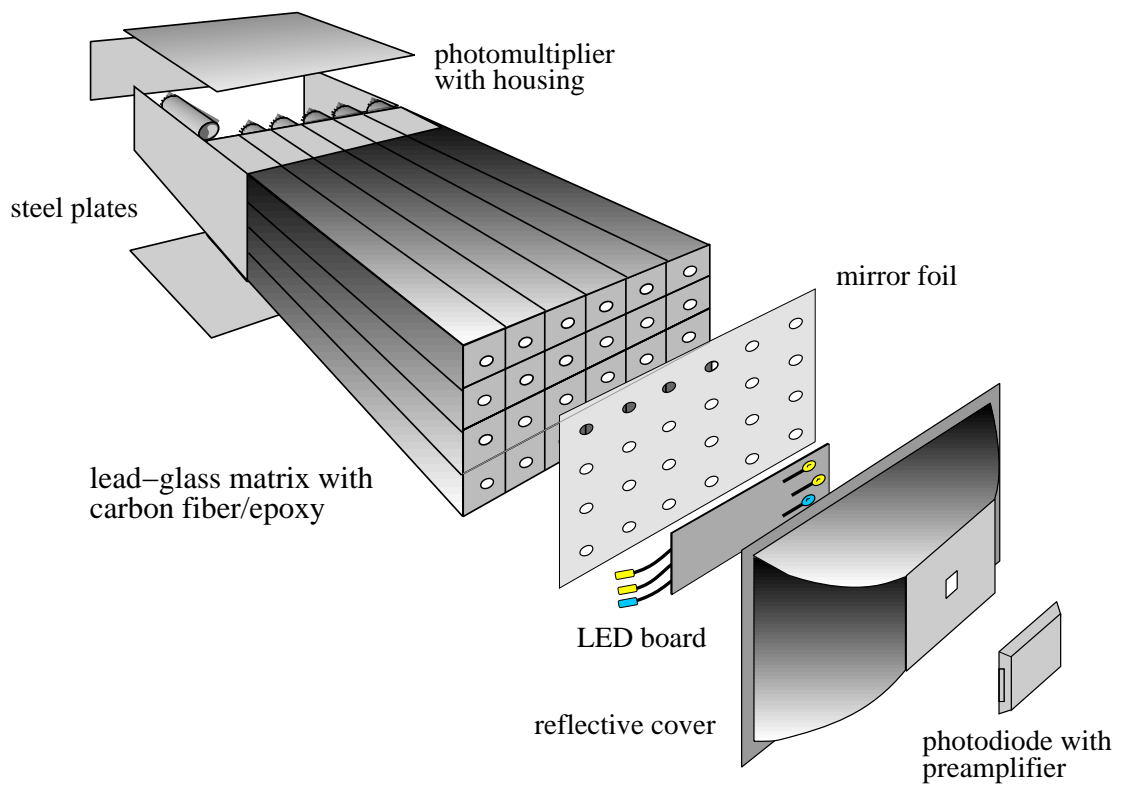
Figure 4.3: Schematic view of a supermodule of the LEDA detector [Rey99].

Photons create an electromagnetic shower, a cascade of secondary e^+e^- pairs and bremsstrahlung, in the lead-glass crystal. The lateral extension of such a shower can be expressed by the Moliere radius R_M:

$$R_M = 21 \text{ MeV} \cdot \frac{X_0}{\varepsilon}, \tag{4.1}$$

where X_0 describes the radiation length of the material and ε is the critical energy necessary for ionization processes. 99% of all shower particles are produced within a radius of $3R_M$. Electrons and positrons moving at a velocity v larger than the speed of light in a material $v_c(n) = c \cdot 1/n$, where n is the refractive index of the material and c the speed of light in vacuum, emit Cherenkov light which is registered by the photomultipliers. Such electromagnetic showers have two properties which are advantageous for the energy measurement of highly energetic photons: the number of Cherenkov photons a particle produces per unit of tracklength is constant and the energy of the initial photon corresponds linearly to the total length of all positron and electron tracks. This linearity is limited by the linearity of the light absorption in the material for the different penetration depths of particles with different energies and by the fact that showers of particles with very high energies may leak out of the module due to its finite depth.

Hadrons undergo different interactions leading to larger fluctuations of the shower shape. On average, hadronic showers are broader in the lateral direction than electronmagnetic showers. This fact can be used to discriminate between photonic and non-photonic showers.

The edge of the module surface with a length of 4 cm corresponded approximately to $R_M = 3.9$ cm. The depth of each module of 40 cm corresponded to 14.4 radiation length, and roughly one hadronic interaction length. Therefore, $1/e \approx 37\%$ of the hadrons did not undergo hadronic interactions within the detector and were registered as Minimum Ionizing Particles (MIPS). The hadrons created Cherenkov photons, which were detected with an energy signal corresponding to 512 MeV. The CPV detector could be used to further reduce the contamination from hadrons to the photon data sample.

The photomultiplier signal was digitized by ADCs being able to buffer the values while waiting for a trigger and to summarize the contents of different ADCs.

4.2 PHENIX

PHENIX is one of the two general purpose experiments located at the Relativistic Heavy Ion Collider (RHIC) at Brookhaven National Laboratory (BNL). The two

main physics goals, which the experiment was designed for, are the detailed exami-
nation of the strong interaction, especially the determination of the properties of a
possible QGP in heavy ion collisions, and the measurement of the spin structure of
the proton in polarized proton-proton collisions.

4.2.1 The RHIC Facility

The Relativistic Heavy Ion Collider   RHIC has been designed for p+p colli-
sions up to $\sqrt{s} = 500$ GeV and nucleus-nucleus collisons up to $\sqrt{s_{\mathrm{NN}}} = 200$ GeV.
The main focus of the nucleus-nucleus measurements is the creation and detailed
examination of a quark-gluon plasma. The p+p program is not only relevant as a
baseline measurement for A+A collisons, but also allows to examine the spin struc-
ture of the proton. RHIC is the only ultra-relativistic collider that can provide
collisions of polarized protons.

The heavy ions collided at RHIC are created in a pulsed sputter ion source and
subsequently injected into a Tandem Van de Graaf accelerator, where the ions are
accelereated to energies of 1 AMeV and ionized from the initial -1 charge to a $+12$
state by passing through a stripping foil. After exiting the Tandem Van de Graaf
accelerator, the ions are ionized further to a $+32$ state by passing through another
stripping foil. The ions are then injected to the Booster through a transfer line
where the ion pulse is shaped to match the 45 bunched Booster turns. The booster
accelerates the ions up to an energy of 95 AMeV, groups them into 6 bunches,
before injecting the beam into the AGS. On exiting the booster, the ions undergo
another stripping process, where all but the two most tightly bound electrons are
removed. Four Booster fillings are injected into the AGS, the ions are rebunched
into four bunches and accelerated to 8.86 AGeV. The last electrons are removed
on exiting the AGS, when the ions are injected into RHIC. The ions are injected
into two separate rings, in one ring clockwise, in the other counterclockwise. At
four dedicated interaction points, where the experiments are located, the bunches of
the two beams cross each other to cause the collisions of the nuclei. When protons
are collided at RHIC, they are injected directly from the Proton LINAC into the
Booster ring with an energy of 200 MeV and then undergo the same acceleration
steps as the heavy ions [Ben, Hah03].

In 2000, first physics data was taken with a maximum center-of-mass energy of
$\sqrt{s_{\mathrm{NN}}} = 130$ GeV, followed by Au+Au and p+p collisions at $\sqrt{s_{\mathrm{NN}}} = 200$ GeV in
2001. In February 2009, the first p+p collisions at the top energy of $\sqrt{s} = 500$ GeV
were created at RHIC.

RHIC is equipped with two independent collider storage rings, both together
with the availability of two independent Tandem Van de Graaf accelerators, facilitate

collisions of different species. RHIC already provided d+Au collisions at $\sqrt{s_{\mathrm{NN}}} =$ 200 GeV in 2002. Deuterium was chosen over protons for its charge-to-mass ratio which is similar to that of gold. This allows an easier configuration of the collider. In 2004/2005, RHIC also provided data for a second heavy-ion species at $\sqrt{s_{\mathrm{NN}}} =$ 22.4, 62.4 and 200 GeV with collisions of copper nuclei. Besides PHENIX, which is detailed in the next section, 3 major experiments are situated at RHIC, as shown in Figure 4.4.

BRAHMS The BRAHMS experiment [Ada03a] employs two independently moveable spectrometer arms to measure the rapidity dependence of particle production with good particle identification capabilities. Although the azimuthal coverage of each of the two arms is small, it is possible to cover the entire rapidity interval of $0 \lesssim y \lesssim 4$. The experiment has concluded its experimental program and stopped data taking in June 2006.

PHOBOS   Similar to BRAHMS, PHOBOS [Bac03] has also been designed to cover a large rapidity interval. Its multiplicity array allow the measurement of charged particle multiplicities in the rapidity region $|\eta| \leq 5.4$. Two spectrometer arms allow the examination of identified charged particles for rapidities $0 \leq \eta \leq 2$ in greater detail.

STAR   The STAR [Ack03] experiment is focussed – similar to the physics program of PHENIX – on the search for signatures of the QGP and the measurement of the spin-structure of the proton. The experimental approach differs significantly from the PHENIX design. The most important detector of STAR TPC with a length of 4 m. It allows for full track reconstruction in the pseudo-rapidity range $|\eta| < 1.0$ with complete 2π azimuthal coverage. It is located inside a solenoidal magnet which can provide a magnetic field of up to 0.5 T to enable the momentum measurement of charged particles. Together with information on the energy loss, this allows the identification of charged particles. Other subsystems include electromagnetic calorimeters, a time-of-flight layer and a RICH detector enhance the capabilities for particle identification and the measurement of high-p_{T} particles.

4.2.2   PHENIX Setup

The PHENIX experiment has been designed to measure a wide range of different observables. Around midrapidity, an electromagnetic calorimeter and different tracking detectors provide information on photons, electrons and charged hadrons,
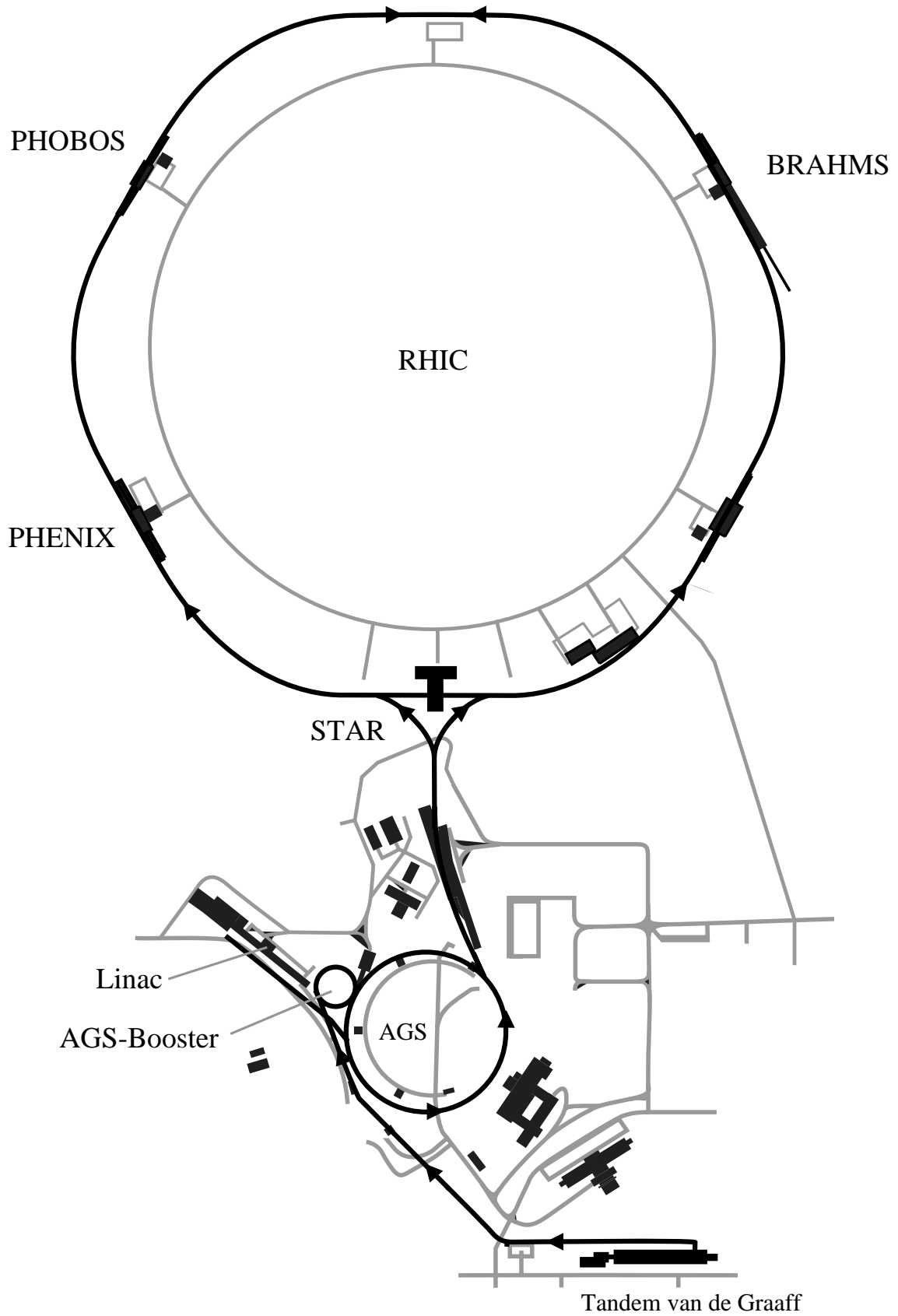
Figure 4.4: Overview of the RHIC facility and the major experiments [Hah03].

two forward arms are dedicated to the measurement of muons, an additional set of
detectors is used to characterize the global properties of each event [Adc03b]. An
overview of the PHENIX setup for Run5 is shown in Figure 4.5, the different de-
tectors are discussed in the following, focussing on the subsystems relevant for the
neutral-pion measurement presented in this thesis.

Global Detectors

The Beam-Beam-Counter (BBC), the Multiplicity Vertex Detector (MVD), and the
Zero Degree Calorimeter (ZDC) are located near the beampipe and are often referred
to as global or inner detectors. Their task is the determination of global event
properties as centrality, collision vertex and charged particle multiplicity as well as
the determination of the minimum-bias trigger condition [All03].

The two BBC detectors are placed 144 cm away from the interaction point
around the beam pipe. Each consists of 64 photomultipliers with a quartz crys-
tal as Cherenkov radiator. The BBC has a time resolution of 52 ps and delivers
the start time for the TOF measurement. Together with the ZDC it is also used to
determine the z-vertex, i.e. the position along the beam axis, of the collision. The
multiplicity information of the BBC is commonly used to determine the centrality
of an event.

The MVD has been designed to measure the production of charged particles
and to determine the collision vertex. It consists of two concentric silicon strip
detector barrels and two disk shaped silicon pad detectors as endcaps. In Run5,
only these endcaps, positioned around the beampipe at $z \approx \pm 35$ cm, are in the
setup to minimize the material in front of the calorimeter arms.

The ZDCs [Adl03b] are hadron calorimeters located near the beam axis. They
can detect neutrons emitted under small angles with respect to the beam axis in
heavy ion collisions.

The Muon Arms

PHENIX is equipped with two muon arms that can track and identify muons at
forward rapidities of $1.2 \leq |y| \leq 2.4$ with full azimuthal coverage. The physics goals
for this subsystem are the study of the vector meson production, the Drell-Yan
process and heavy quark production [Aki03]. The two arms feature the same setup:
a muon tracker, consisting of three so-called stations of tracking chambers inside
a magnet providing a radial field for momentum analysis, enables the separation
of different heavy quark states and vector mesons and allows reconstructing the
tracks. The Muon Identifier consists of alternating layers of absorber material and
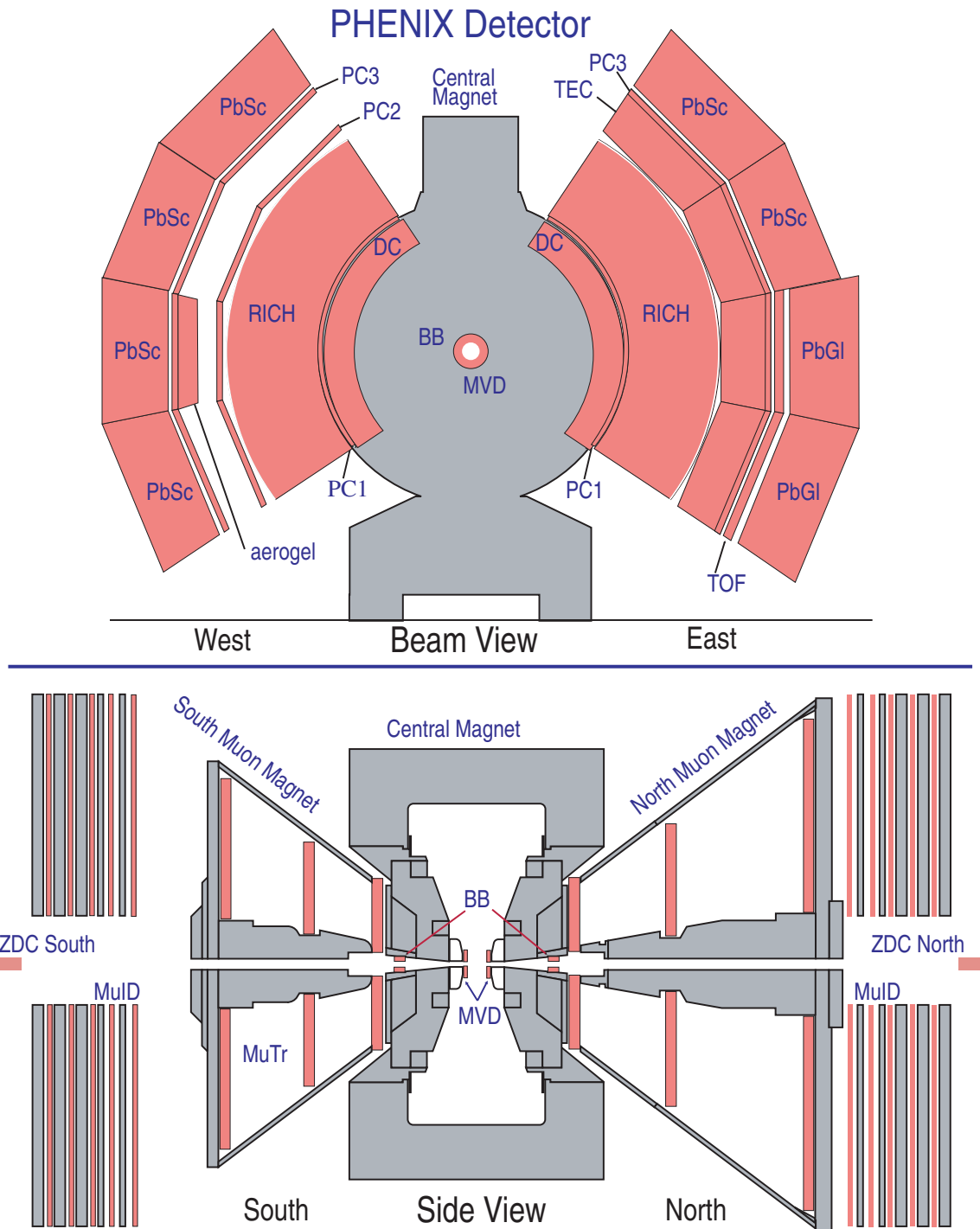
Figure 4.5: Setup of the PHENIX experiment for the Run5 beamtime [PHE09].

low resolution tracking detectors. The detectors are assembled as planes of Iarocci
tubes, operated in proportional mode. The layered setup improves the tracking
capabilities of this system.

The Central Arm

In the central arm several different types of tracking detectors allow determining
the path of a particle. This can be combined with the information of the particle
identification detectors and calorimeters. The central arm is separated into two sets
of detectors as shown in Figure 4.5, the East-Arm and the West-Arm, their setup is
detailed in [Adc03a].

The innermost detectors are the Drift Chambers (DC) in both the east and
the west arm, located $2 - 2.4$ m from the beam axis. The detector provides high-
resolution p_T information for single particles and for the reconstruction of the in-
variant mass of particle pairs from the trajectory through the magnetic field. It also
adds position information for the tracking of particles through different subsystems.

3 layers of Pad Chambers (PC) in the west arm (PC1, PC2, PC3) and two layers
in the east arm (PC1, PC3) provide high resolution space points for the tracking
of particles. The PCs consist of multiwire proportional chambers with one wire
plane and two cathode planes. One of these cathode planes is subdivided into pixels
and allows a two-dimensional position determination with a resolution of 1.7 mm in
z-direction.

The Time Expansion Chamber (TEC) consists of 4 sectors with 6 stacked multi-
wire tracking chambers in the east arm. The TEC provides direction vectors for the
charged particles passing through the detector that can be matched to the PC and
DC information in the event reconstruction. Additionally, the energy loss of particles
in the detector allows to identify different particles and especially improves the
electron/pion separation for p_T between 200 MeV/c and 2.5 GeV/c. As an upgrade
of the TEC that would allow extending the electron/pion separation capabilities
up to several tens of GeV/c by measuring transition radiation, radiators have been
installed, but have not been utilized so far.

A Ring Imaging Cherenkov detector (RICH) is installed in each of the two arms
behind the PC1. It is the main detector for electron identification in PHENIX
and has a volume of 40 m^3 filled with CO_2. This gas has been chosen because
the Cherenkov threshold for pions is relatively high at $p = 4.65$ GeV/c, enabling
a separation from electrons up to these momenta. Together with the information
from the EMCal described below and the TEC, the RICH helps to limit the false
identification of hadrons as electrons or positrons to less than 1 in 10^4 for momenta
below the Cherenkov threshold.

Charged hadrons can be identified by the Time Of Flight (TOF) detector. It consists of 960 scintillator slats, oriented in the r-ϕ direction at a distance of 5.1 m from the collision vertex in the east arm of the experiment. The TOF can determine the arrival of a particle with a resolution of 100 ps. Together with the start signal from the BBC, this allows separating π/K up to 2.4 GeV/c and K/p up to 4.0 GeV/c.

The central arm also contains two different types of electromagnetic calorimeters (EMCal). These are the main detectors for the PHENIX analysis presented in this thesis and are discussed in more detail below.

Electromagnetic Calorimeters

For the PHENIX Electromagnetic Calorimeter (EMCal) two different detector types are employed [Aph03]. The EMCal is composed of 8 sectors, four in each of the central arms. The sectors E0 and E1 in the east arm are equipped with a lead-glass calorimeter (PbGl), this subdetector is assembled from the WA98 LEDA detector. The supermodules were designed to be rearranged for the PHENIX geometry, the two sectors are built of 192 of the WA98 supermodules. While the WA98 calibration system has been retained, the supermodules have been equipped with new readout electronics for the PHENIX experiment.

The second subdetector system of the EMCal used for the other 6 sectors is a lead scintillator calorimeter (PbSc). This detectors has been constructed as sandwich calorimeter consisting of 66 cells which each contain a 1.5 mm thick lead absorber and a 4 mm thick organic scintillator. The cells are connected by wavelength shifting optical fibres, which are read out by a photomultiplier at the end of 5.535 cm $\times$ 5.535 cm $\times$ 37.5 cm large towers. Four towers are grouped together mechanically to form a module. For installation purposes, 6×6 modules are assembled to a mechanically firm supermodule, 3×6 of these supermodules forming one sector of the PbSc. For calibration and monitoring purposes, a UV laser is distributed via optical splitters and fibres to each module. The system has been designed to simulate an electromagnetic shower of 1 GeV.

Although hadrons deposit more energy in the PbGl calorimeter, the use of scintillators in the PbSc allows the measurement of low energy hadrons, that do not produce Cherenkov light and thereby on the one hand provides a better energy measurement for hadrons which is used for the determination of the transverse energy E_{T}. On the other hand this increases the background for photon measurements. Due to its finer granularity, the PbGl detector is better suited for the measurement of highly energetic showers, where the merging of adjacent showers reduces the detector efficiency. This is especially important for the measurement of neutral pions

with high transverse momenta, as the showers created by the two decay photons are created close to each other on the detector surface.

Trigger and Data Acquisition

The PHENIX data acquisition relies on two consecutive trigger levels to record the physics data and identify and mark events with interesting characteristics before storing them [Adl03c, Adl03d].

The detector subsystems provide the event data to the triggers and the data acquisition through Front End Modules (FEMs), which allow standardized communication between the trigger and the different sub-detectors. The trigger level 1 is divided into two components: the Local Level-1 (LL1) and the Global Level-1 (GL1). Each of the LL1 systems reads the event data of one subsystem from the according Front End Module (FEM) and reduces the information necessary for the generation of a trigger decision to a small bit pattern that is provided to the GL1. The results of this analysis, the Level 1 primitives, are forwarded to the Level 2 trigger together with the data. Some of the subsystems do not need a dedicated LL1 system, e.g. the ZDC only forms coincidences of the signal from the two detectors and provides this information to the GL1. The task of the GL1 is to generate a Level 1 trigger decision from the results provided by the LL1 systems and to forward the RHIC clock to the FEMs and LL1 systems. If an event is accepted by the Level 1 trigger, the FEMs transfer the event data to the Data Collection Modules (DCMs). These VME based modules perform zero suppression and reformat and compress the data before forwarding it to the Event Builder. In this step, the data rate is decreased from a maximum trigger rate of more than 100 GB to a maximum of 140 MB/s during Run 2. To compensate for high rates, the DCM can buffer up to 5 events.

In the Event Builder (EvB) the data streams from the DCMs are merged into one event output, additionally, the Level 2 trigger is generated in the EvB framework. An event builder controller assigns the events to one Assembly/Trigger Processor (ATP). The data are transferred there from the DCMs via subevent buffers and read in asynchronous transfer mode from the ATPs to optimize the bandwidth usage. The ATPs are commercially available PCs that have been designed to assemble an event and apply different Level 2 triggers with a processing time of ≈ 25 ms per event. The Level 2 trigger conditions e.g. enrich events containing particles with high-p_{T}. As the events are produced with typically 40 MB/s and the transfer to the HPSS storage and the RHIC Computing Facility (RCF) cannot exceed 20 MB/s, the events are stored temporarily on dedicated computers in the PHENIX counting house. Due to the decreasing luminosity of the beam during one fill and breaks between fills of RHIC, the data can be transferred from these machines to HPSS without losses.

These processes are coordinated in the PHENIX On-Line Computing System (ONCS) by the Run Control software. This software package also allows online monitoring and a first calibration of the data.

Data Summary Tables

The offline computing activities for PHENIX can be subdivided into 3 sections: data simulation, data reconstruction and data analysis. The PHENIX Integrated Simulation Application (PISA) is a Geant based simulation package that allows simulating events for the PHENIX geometry and the generation of event files that can be used to test the analysis and level 2 trigger code. The events are reconstructed in a computing farm, which is also used for the analysis. The available computing ressources can be shared between these tasks as needed. The PHENIX offline software is written in C++ and based upon the ROOT software package [Adl03c].

The analysis software is interfaced by the Fun4All framework that provides standardized access to the data files. The reconstructed data is saved as Data Summary Tables (DSTs), which are used for the analysis. To reduce the amount of data that has to be filtered by each individual analysis, additional types of DSTs are created, which contain subsets of the data needed for different analyses. The PHENIX analysis presented in this thesis has utilized the so-called PWG-DSTs, which contain the fully reconstructed information of the central-barrel detectors.

5. Neutral Pion Production in PHENIX and WA98

In this thesis, analyses of the neutral pion production measured by WA98 and by PHENIX in ultra-relativistic collisions will be presented. Although the data were taken with different setups at different accelerators, the basic analysis techniques employed are very similar: the neutral pion yield is determined on a statistical basis in the $\pi^0 \rightarrow 2\gamma$ channel, which constitutes 98.8% of all neutral pion decays. Owing to the short lifetime of $8.4 \cdot 10^{-17}$s of the neutral pion [Yao06], the decay vertex for all practical purposes corresponds to the reaction vertex. Reconstruction of the neutral pions via the reconstruction of invariant masses of photon pairs is possible in both experimental setups. In order to determine the combinatorial background, a mixed event technique is employed.

5.1 PHENIX Measurements of the Neutral Pion Production in Cu+Cu Collisions

Copper nuclei were collided at RHIC at three different center-of-mass energies from 22.4 GeV to 200 GeV in the so-called Run05 of RHIC. In this thesis the analysis of the 22.4 GeV data-set is described.

5.1.1 Selection of Data

The data are read from the calibrated PWG-DSTs described in Chapter 4.2.2. During this run, the only trigger condition in use was the minimum bias trigger. The trigger condition requires at least one hit in BBC North and South each. 7.1 million events are available in this data set.

Additionally, the events used for the analysis are restricted to a z-vertex of $|z| \leq 30$ cm. This excludes events occurring in regions shielded by the pole tips of the magnets and suppresses background from scattered particles.

For all runs, observables as the average charge measured in the BBC and the average energy in ZDC are monitored to check for runs that systematically deviate from the average values. This would be an indicator for technical problems during these runs. But as all of the runs DSTs available exhibit a consistent behavior, as shown in Figure 5.1, all are used for the analysis.
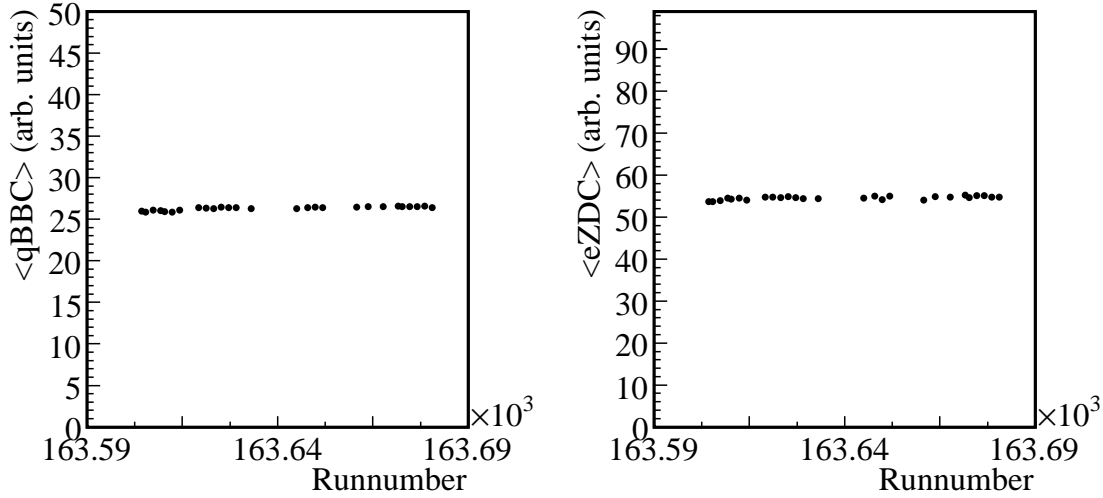
Figure 5.1: Comparison of the average energy in the ZDC and the average charge in the BBC measured in the PHENIX setup as function of the run number. The data are shown with arbitrary units. No deviations, which would be a hint for problems in the data segment, are visible.

5.1.2   Determination of Centrality

The centrality of a collision describes the overlap of the colliding nuclei. In PHENIX, usually the Beam-Beam-Counters (BBC) are used to determine the centrality of a collision. At $\sqrt{s_{\mathrm{NN}}} = 22.4$ GeV however, the rapidity of the beam $y_{\mathrm{beam}} \approx 3.2$ is within the pseudorapidity acceptance of the BBCs of $3.0 < \eta < 3.9$. Therefore the BBC signal cannot easily be used to determine the centrality of an event, since it is not trivial to understand the influence of spectator nucleons on it. Instead, the hit multiplicity in Pad Chamber 1 (PC1) is used to determine the centrality. This is done by comparing the measured multiplicity distribution to a simulated muliplicity distribution and applying the same cuts to both. The centrality information derived from the simulation can then be used to quantify the centrality of the data [Rey06].

The Front-End Modules (FEMs) of the PC1 detector have to be reset at regular intervals. During these resets no data can be obtained from this subsystem. These events are usually recognized and removed during the DST production. The production macros used for the production of Cu+Cu results at $\sqrt{s_{\mathrm{NN}}} = 22.4$ GeV, however, fail to correctly identify the cycle of these resets and instead remove a small fraction of correct events. When the reset occurs, only a low number of hits,

usually zero or one, is recorded by the PC1, although the real number of hits may be significantly higher.

In an event with a real small PC1 multiplicity, only a small number of tracks should be recorded in the Drift Chamber (DC). By correlating the number of PC1 hits with the number of DC tracks, we can estimate the number of events during which a PC1 reset occurred and which were not removed from the DSTs. Events with zero or one hit in PC1, but more than twenty tracks in the DC, are regarded as events during which a reset occured. From this we can estimate that 0.15% of the total number of events used in the analysis are affected by the problem. This is also the maximum number of events which are wrongly removed from the data set. As the selection of these erroneously removed events was based solely on the bunch number, and the absolute number of these events is small, no bias on the physics properties of the remaining events is introduced.

More central events have a higher number of PC1 hits than more peripheral events, as discussed in more detail below. The remaining events during which a PC1 reset occurrs are therefore all assigned to the most peripheral class. It is known, that the PC1 resets occur only in bunches 57 to 70. By requiring a minimum of two PC1 hits only for these bunches, we effectively remove most of the PC1-reset-events without a significant influence on the valid peripheral events, as shown in Figure 5.2.

Use of the Pad Chamber for Centrality Determination

The PC1 multiplicity distribution is linked to the centrality information using a Glauber Monte Carlo simulation of the distribution to obtain the number of participants per event (N_{part}). The number N_{ancestor} of particles from which a PC1 hit is generated can be related to N_{part} via an exponent α:

$$N_{\text{ancestor}} = N_{\text{part}}^{\alpha}. \tag{5.1}$$

The simulated PC1 hit multiplicity is obtained by sampling a negative binomial distribution (NBD) for each of the ancestor particles:

$$P_{\mu,k}(n) = \frac{\Gamma(n+k)}{\Gamma(n+1)\Gamma(k)} \cdot \frac{(\mu/k)^n}{(\mu/k+1)^{n+k}}. \tag{5.2}$$

This procedure is carried out systemtically for a grid of values for the parameter α, μ, and k as well as for the BBC trigger efficiency ε_{BBC}. The PC1 hit distribution shows a slight dependence on the z-vertex. To correct for this, a set of parameters for the interval -5 cm $< z < 5$ cm is determined by choosing the set of parameters
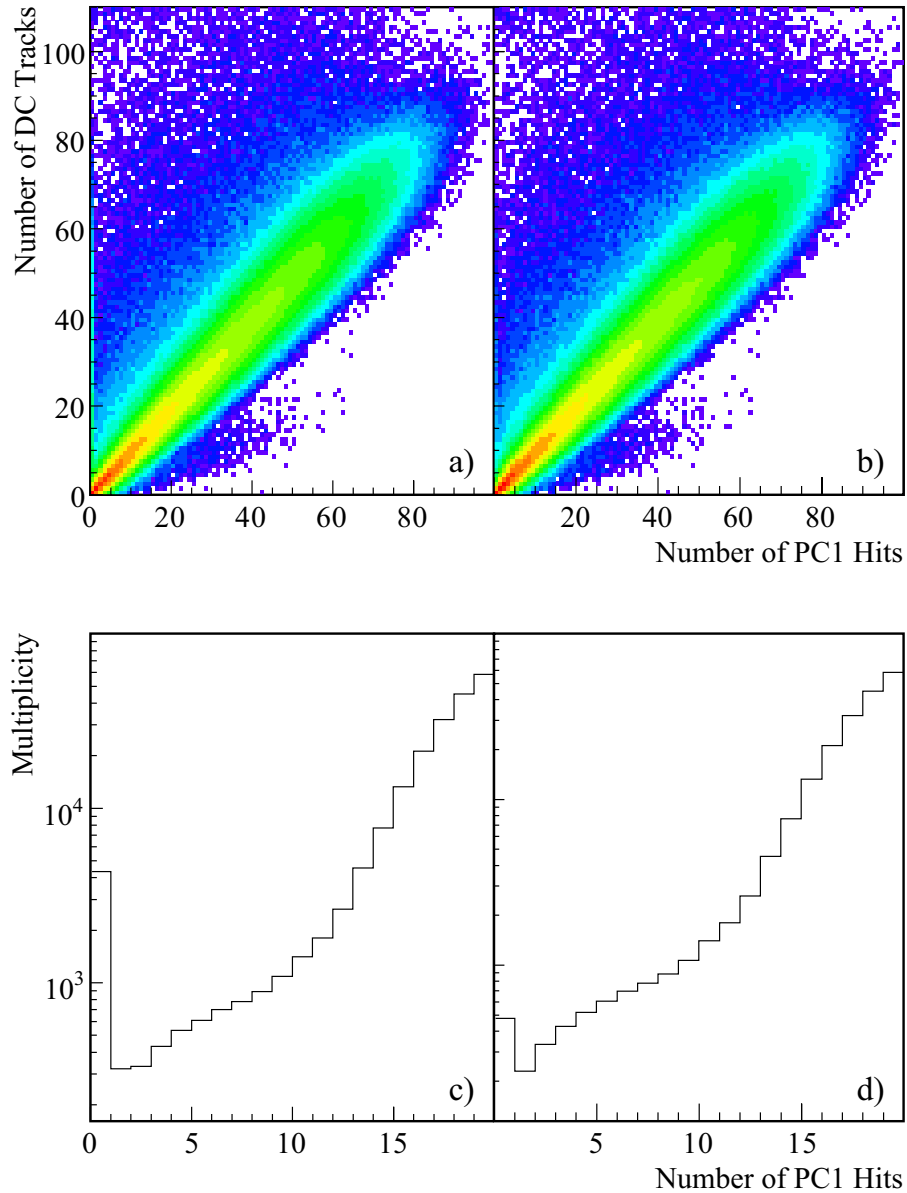
Figure 5.2: Comparison of the number of driftchamber tracks measured by PHENIX before (a) and after (b) the rejection of PC1 resets. The z-axis of these two plots is shown on a logarithmic scale. A projection of the number of PC1 hits for at least 20 tracks in the drift chamber before the rejection is shown in (c). After the rejection, the initally large amount of events with zero PC1 hits is significantly reduced (d).

for the simulation which yields the lowest χ^2 value when compared to the data according to

$$\chi^2 = \sum_i \frac{(N_{PC1}(i) - N_{PC1,MC}(i))^2}{\sigma^2(N_{PC1}(i)}.$$

At small N_{PC1}, the simulation exceeds the data. This deviation can be attributed to the BBC trigger efficiency ε_{BBC}. The best description of the data is obtained with $\varepsilon_{BBC} = 0.8$ [Rey06].
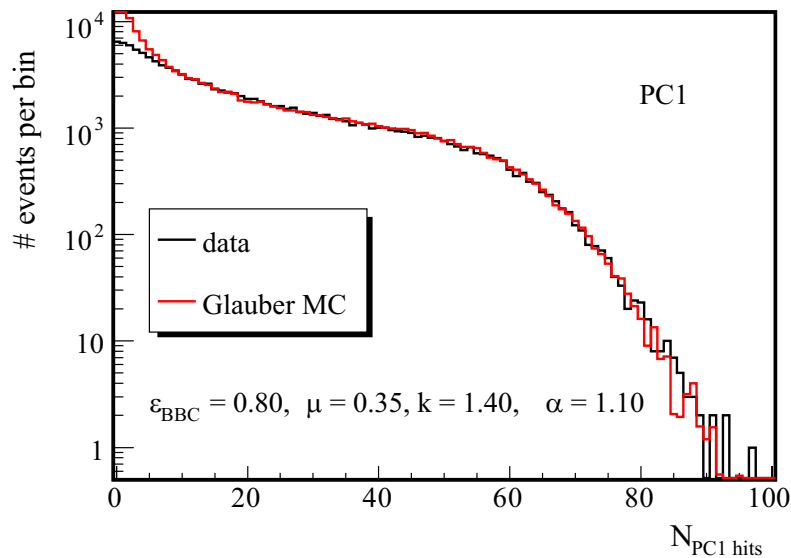
Figure 5.3: PC1 hit multiplicity for the z-vertex interval $|z| < 5$ cm measured by PHENIX and the result from a Glauber Monte Carlo calculation. The overestimation of the data by the simulation for small PC1 multiplicities can be explained by the effect of the BBC trigger bias which is not modeled in the simulation [Rey06]. The values assumed for Equations 5.1 and 5.2 are shown in the Figure.

The normalization of the measured PC1 distributions varies for different cuts on the z-vertex. A correction factor f_{PC1} is determined so that $N_{PC1,corr} = f_{PC1} \cdot N_{PC1}$ describes the data. The correction factors used in the analyis are shown in Table 5.1. When taking the full range of the BBC z-vertex of ± 30 cm into account, a broad range of values for ε_{BBC} delivers reasonable results. Therefore the trigger efficiency can only be constrained to $0.75 \le \varepsilon_{BBC} \le 0.95$. This is also a major difference to the centrality determination for other systems and at other center-of-mass energies: while the same Glauber code that has been used here has also been

z-vertex interval (cm)	factor f_{PC1}
$[25, 30[$	1.065
$[20, 25[$	1.037
$[15, 20[$	1.037
$[10, 15[$	1.
$[5, 10[$	1.
$[0, 5[$	1.
$[-5, 0[$	1.
$[-10, -5[$	1.
$[-15, -10[$	1.
$[-20, -15[$	1.014
$[-25, -20[$	1.027
$[-30, -25[$	1.060

Table 5.1: Correction factors for the simulated PC1 distribution to account for the z-vertex dependence of the measured distribution. [Rey06].

employed for other PHENIX measurements, the trigger efficiency has been an input into the calculation.

To demonstrate the validity of the results from the Glauber Monte-Carlo calculation, different cross-checks are done: first, the method described to reproduce the PC1 distribution is used to fit the BBC distribution. Although a strong non-linearity is observed, which can be attributed to the influence of the beam, the resulting range for the trigger efficiency is compatible with the PC1 results. Furthermore, the trigger efficiency is estimated using VENUS 4.12 [Wer93]. In this simulation, the BBC trigger condition is regarded as fulfilled when at least one charged particle is found in the acceptance of both the BBC North and the BBC South. This model yields $\varepsilon_{\mathrm{BBC}} = 0.78$, which confirms the results obtained from the Glauber Monte Carlo calculation.

The centrality classes and the corresponding number of participants N_{part} and collisions N_{coll} are determined in the Glauber Monte Carlo simulation. The cuts on the PC1 multiplicity derived from the simulation are then utilized in analysis to classify the centrality of an event.

The centrality cuts used, together with the corresponding values for N_{part}, N_{coll}, T_{AB} and the impact parameter b with the corresponding uncertainties, can be found in Table 5.2. The uncertainties are determined, in addition to the uncertainties for e.g. the nucleon-nucleon cross section and the assumed nuclear geometry, by two

PC1 cut	centr.	N_{part}	σ_{sys}	N_{coll}	σ_{sys}	T_{AB} (mb^{-1})	σ_{sys}	b (fm)	σ_{sys}
$N \geq 53$	0- 5%	98.2	2.0	152.7	16.5	4.73	0.44	2.0	0.1
$53 > N \geq 44$	5- 10%	85.9	2.2	128.1	12.3	3.97	0.34	2.9	0.2
$44 > N \geq 30$	10- 20%	67.8	3.1	93.6	9.4	2.90	0.28	4.0	0.3
$30 > N \geq 14$	20- 40%	41.0	3.6	48.4	6.5	1.50	0.21	5.7	0.3
$14 > N \geq 9$	40- 50%	23.1	3.3	22.9	4.4	0.71	0.14	7.0	0.4
$9 > N \geq 0$	50-100%	8.8	1.6	7.3	1.7	0.23	0.05	8.8	0.5
$N \geq 44$	0- 10%	92.2	2.2	140.7	14.8	4.36	0.40	2.4	0.1
$44 > N \geq 21$	10- 30%	58.6	3.2	77.6	8.1	2.40	0.25	4.6	0.3
$21 > N \geq 6$	30- 60%	24.9	3.2	25.9	4.5	0.80	0.14	6.9	0.4
$6 > N \geq 0$	60-100%	6.5	1.3	5.0	1.2	0.15	0.04	9.1	0.5

Table 5.2: Glauber results from 22.4 GeV Cu+Cu collisions with the corresponding systematic uncertainties σ_{sys} [Rey06].

different parameter sets for the NBD, which correspond to two extreme assumptions for the trigger efficiency of the BBC $\varepsilon_{\text{BBC}} = 0.76$ and $\varepsilon_{\text{BBC}} = 0.90$.

5.1.3 Photon Identification Cuts

As described in Section 4.2.2, the DSTs contain information on the shape of the individual showers in the electromagnetic calorimeters. This information can be used to improve the identification of photons and to reduce background from hadronic showers in the analysis, due to the fact that hadronic showers occupy larger areas, when projected onto the detector surface, than electromagnetic showers. For the PbGl and the PbSc calorimeter different methods are foreseen:

for the PbGl calorimeter, the dispersion D in x- and y-direction of the detector surface is stored in the DSTs. It is determined from the energies E_i registered in a detector module at the position x_i.

$$D = \frac{\sum E_i x_i^2}{\sum E_i} - \left(\frac{\sum E_i x_i}{\sum E_i}\right)^2 = \overline{x^2} - \overline{x}^2 \qquad (5.3)$$

As the finite size of the detector modules leads to a minimum dispersion $D^{min} = |\overline{x}| - \overline{x}^2$ for each x, a corrected dispersion

$$D_x^{cor} = D - D^{min} \qquad (5.4)$$

can be defined.

We reject all hits, for which the maximum of the cut threshold D_{cut} is exceeded by the maximum value of the dispersion along the x and y axis. This cut is described in detail in [KB00], it is given by the equation

$$D_{\text{cut}}(\theta) = 0.27 - 0.145 \cdot \theta + 0.00218 \cdot \theta^2. \tag{5.5}$$

The cut parameter depends on the angle θ with respect to a perpendicular on the detector surface. It is necessary to introduce an angular dependence, because for increasing angles the showers spread over a larger number of modules.

For the PbSc calorimeter, the DSTs contain the χ^2-parameter representing the agreement of the shape between the measured shower and an ideal shower from detailed simulations (see Section 4.2.2). We only identify hits with $\chi^2 < 3$ as electromagnetic showers for the analysis.

To reject minimum-ionizing particles, which do not create a shower in the calorimeters and therefore cannot be rejected with the cuts described above, a minimum energy of the cluster $E_{\text{cluster,min}}$ of 200 MeV is required.

5.1.4   Exclusion of Calorimeter Modules

Not every module in the electromagnetic calorimeters is available for the analysis. Some modules were deactivated during data taking due to known hardware problems. During the DST production additional quality assurance criteria were applied e.g. on the energy spectra to identify and remove modules from the data which are defective. During the analysis we record the hit multiplicity for each module for different energy intervals. Modules exceeding the mean hit multiplicity by more than 6 times the RMS value of the PbGl and 4.5 times the RMS value of the PbSc detector, are regarded as *warm* modules and excluded from the analysis. The map of the excluded modules can be found in Appendix C.1.

5.1.5   Determination of the Invariant Mass and Extraction of the Neutral Pion Yield

As photons do not have a rest mass, the invariant mass of the photon pair can be expressed as

$$m_{inv} = \sqrt{(P_{\gamma 1} + P_{\gamma 2})} = \sqrt{2E_{\gamma 1}E_{\gamma 2}(1 - \cos(\theta_{12})}. \tag{5.6}$$

In order to determine the neutral pion yield, the invariant mass is calculated for each photon pair combination in an event and stored in a histogram according to the reconstructed p_{T}. The energy distribution of the decay photons in the lab system

should be uniform: in the rest frame of a neutral pion, the decay into two photons, with an angle of 180° is symmetric. When observed in the lab frame, the random angle between the decay photons and the flight path together with the Lorentz-boost, which has to be taken in to account when changing the reference frame, lead to the uniform distribution of the neutral pion energy on the two photons. Due to the steeply falling shape of the p_T spectra of the neutral pions, this combinatorial background is dominated by low energy photons. Most of the pair combinations are random – the photons are not correlated – which leads to a strongly enhanced contribution of photon pairs with a large asymmetry α, defined as

$$\alpha = \left| \frac{E_1 - E_2}{E_1 + E_2} \right|. \tag{5.7}$$

Only photon pairs with $\alpha < 0.7$ are regarded in the analysis to reduce the dominating contribution from low energetic photons to these random pairs. To account for the loss of real pions from the data sample due to this restriction, we apply the same cut in the efficiency calculation.

A mixed event method is employed to subtract this background from uncorrelated photons: For each photon an invariant mass is calculated using photons from different events with imilar vertex position and multiplicity. Due to the dominating contribution of low multiplicity events in the data sample, using events with strongly deviating multiplicity would cause a distortion of background distribution, so that the real background is no longer correctly described. Photons from these other events are by definition not correlated, such that the resulting distribution can be used to subtract the combinatorial background. The absolute height of this background distribution is solely determined by the number of uncorrelated events used for the calculation.

Before subtracting the background from the real distribution, it is scaled to the height of the real invariant mass distribution by a fit to the ratio of the real and the mixed event histograms, in a region where no peak from particle decays is expected. This procedure is executed for different p_T intervals. The remaining peak is integrated over a 3σ interval for each p_T-bin to obtain the raw neutral pion yield.

5.1.6   Energy Recalibration of the Neutral Pion Peak

The analysis of neutral pions allows to improve the energy calibration of the detector by calibrating the position of the neutral pion peak. Due to the steeply falling shape of the spectra and the limited energy resolution, the peak is shifted to invariant masses higher than the nominal value of 134.9 GeV.

A strict asymmetry cut of $\alpha < 0.2$ is applied to the data, so that for the energies $E_{\gamma 1}$, $E_{\gamma 2}$ of the decay photons $E_{\gamma 1} \approx E_{\gamma 2} \approx E_{\pi^0}/2$ can be assumed. A Monte Carlo simulation modelling the experimental setup, which is described in detail in [KB04], reproduces the widths of the measured neutral pion peaks well with an additional empirically determined smearing of the energy based on a Gaussian distribution. Unlike for higher center-of-mass energies, shower merging, the misidentification of two overlapping showers as a single one, is negligible at the energy of this data set due to the low event multiplicity. The peak widths obtained from the simulation and the data are shown in Figure 5.4. The simulation reproduces the measured widths well.
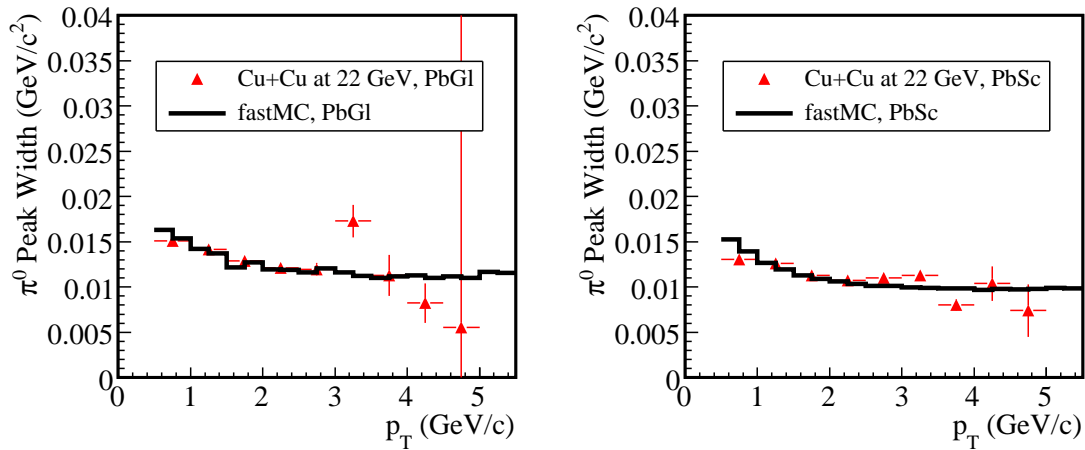
Figure 5.4: Comparison of the measured width of the neutral pion peak in the PHENIX lead-glass calorimeter (left panel) and the lead-scintillator calorimeter (right panel) to the width from the Monte-Carlo simulation.

A remaining deviation of the position of the neutral pion peak in the simulation from the data can then be attributed to uncertainties in the energy scale. An additional empirical correction for the energy of the individual photon hits is applied to reduce this uncertainty.

Due to the statistical limitations of the 22 GeV data set used for this analysis, it is only possible to extract an energy-independent correction factor. Experience from earlier runs however shows that the empirical correction exhibits a non-linearity and that the necessary correction does not vary strongly throughout a whole runtime. We therefore employ the correction extracted from the Cu+Cu data set taken at $\sqrt{s_{\mathrm{NN}}} = 200$ GeV and 62.4 GeV. This correction is compatible with the correction extracted from the 22 GeV data set, but also contains a non linear term that is

relevant at higher p_T. The correction factors used in the analysis are shown in Table 5.3. The factor a_0 is a constant correction factor which is determined for each sector of the electromagnetic calorimeter. Additionally, a non linear correction $a_{1,0-2}$ for both of the subdetectors is determined. The energy of each hit is corrected by

$$E_{hit,corr} = E_{hit,meas} \cdot a_0 \cdot a_{1,0} \cdot a_{1,1} \cdot \exp^{a_{1,2} \cdot E_{hit,meas}} . \tag{5.8}$$

The correction has been optimized over several iterations, each factor corresponds to one step in this process. The comparison of the corrected data to that of the simulation is shown in Figure 5.5

	E0	E1	E2	E3	W0	W1	W2	W3
a_0	9.95074e-1	1.00524	1.04011	1.04376	1.05601	1.05843	1.02543	1.02042
$a_{1,0}$	9.90000e-01			1.00696e+00				
$a_{1,1}$	4.40177e-02			1.00000e-01				
$a_{1,2}$	-5.61228e-01			-3.48038e+00				

Table 5.3: Correction factors for the energy of photon hits used in this analysis.
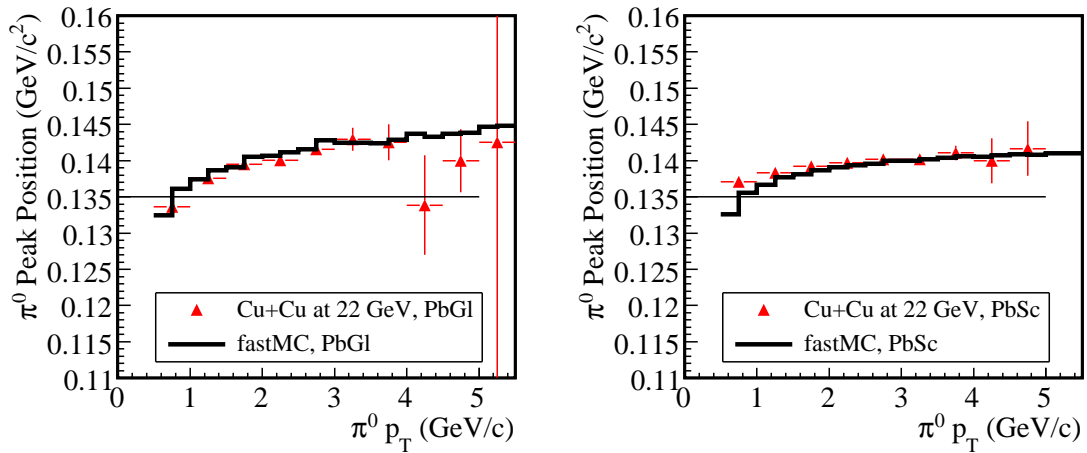
Figure 5.5: Comparison of the neutral pion peak position from the corrected PHENIX data to the simulation. The left panel shows the results for the lead-glass calorimeter, the right panel the results for the lead-scintillator calorimeter. The simulated position of the neutral pion peak describes the measured position well.

5.1.7   Acceptance and Efficiency Correction

The correction for the limited geometrical acceptance is obtained from Monte Carlo simulations described above. The acceptance correction is determined by simulating decays of neutral pions into two photons in the interaction region and calculating the fraction of neutral pions, where both decay photons hit the detector. The reduction of the geometrical acceptance by dead modules, i.e. detector modules which have not been operated during the run or which exhibit significant noise during the analysis, is accounted for by reading the same dead module map as in the analysis code and excluding the marked modules. The acceptance correction shown in Figure 5.6 is obtained by dividing the simulated p_T spectrum of all particles on the active detector surface by the input spectrum.

The distribution of the original particles around the interaction region is modeled with Gaussian fits to the measured rapidity and z-vertex distribution and with a uniform distribution in ϕ. The particles are generated with a flat distribution in p_T to enhance the number of particles with high transverse momentum, the correct physical shape is inferred by a weight, iteratively determined from the fully corrected spectra.

The same simulation is used to determine the efficiency correction, which accounts for detector effects and analysis cuts influencing the measured spectrum. The efficiency corrections applied to the PbGl and the PbSc detector are shown in Figure 5.6. The increase of the efficiency towards higher transverse momenta can be attributed mainly to the influence of the energy smearing in connection with the steeply falling shape of the spectra: particles smeared from low to high p_T constitute a larger relative fraction of the contents in the higher bin than at the original lower p_T. The efficiency ε can be defined as the ratio of the measured spectrum $f_{meas}(p_T)$ to the true spectrum $f_{true}(p_T)$:

$$\varepsilon = \frac{f_{meas}(p_T)}{f_{true}(p_T)}. \tag{5.9}$$

While the relative loss due to the energy smearing in all bins is the same the absolute gain can overcompensate this loss and may even lead to efficiencies larger than one. The small values of the efficiency at low transverse momenta can also be attributed to the influence of the particle identification cuts, especially the energy cut, which has a large impact at these p_T. No dependence on the centrality of the events is included in the efficiency calculation.
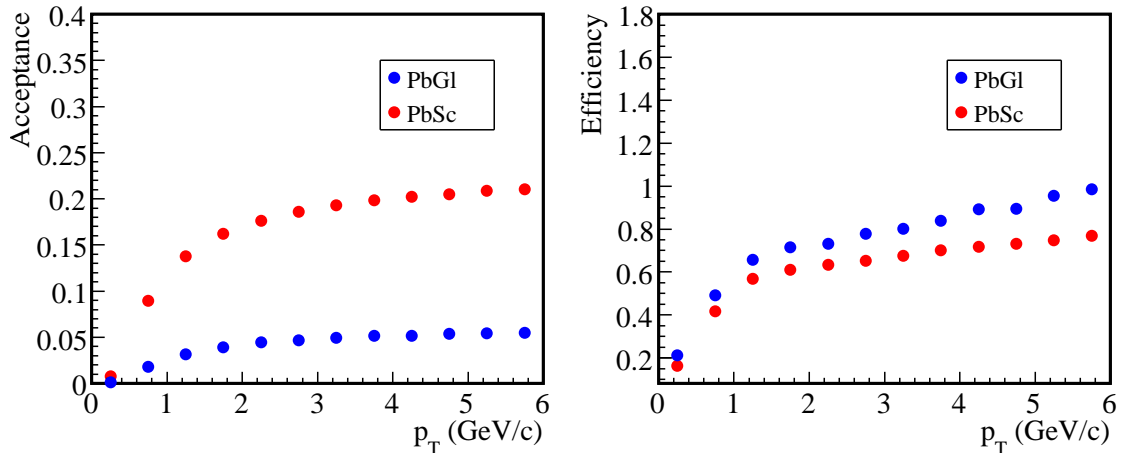
Figure 5.6: Geometrical acceptance (left panel) and efficiency (right panel) of the two PHENIX calorimeters for the detection of neutral pions.

5.1.8 Bin Shift Correction

The analysis of the invariant mass spectra is based on histograms with a finite bin width. In the peak extraction procedure the measured yield is attributed to the center of the corresponding p_T-bin. As the neutral pion spectra are steeply falling, this average value does not represent the most probable value of the true spectrum at the bin center.

It is possible to overcome this by shifting the points to represent this true value, either in p_T, so that the respective value of the yield remains unchanged but is at the correct position on the p_T-axis or to leave the p_T value unchanged and move the point to the yield that represents the correct value at the bin center [KB04]. To retain the original bin widths, the yield is corrected in this analysis. A fit with a so-called Hagedorn function $f_{Hag}(p_T) = a \cdot \left(\frac{b}{b+p_T}\right)^2$ to the invariant yield is used to obtain the correction factor r:

$$r = \frac{\frac{1}{\Delta p_T} \int_{p_{T,\text{cent}}-0.5\Delta p_T}^{p_{T,\text{cent}}+0.5\Delta p_T} f_{Hag}(p_T) dp_T}{f(p_{T,\text{cent}})} \tag{5.10}$$

where $p_{T,\text{cent}}$ gives the center of a bin and Δp_T its width. The corrected yield can be obtained from:

$$\left.\frac{dN}{dp_T}\right|_{corr} = \frac{1}{r} \left.\frac{dN}{dp_T}\right|_{uncorr} . \tag{5.11}$$

The original fit is only an approximation of the true yield. Therefore we apply this correction iteratively until the difference between two iterations becomes negligible.

5.1.9   Additional Corrections

In order to obtain fully corrected Lorentz-invariant yields additional corrections
are necessary: the spectrum has to be normalized to the bin width used in the
peak extraction, the pseudo-rapidity coverage of the acceptance determination in
the Monte Carlo simulation of $|\eta| \leq 0.45$ and corrected for the branching ratio of
98.798%. The loss by conversions $\gamma \rightarrow e^+ e^-$ between the interaction vertex and the
detector surface is accounted for by a p_{T}-independent correction factor of 10% in
the PbSc and 7% in the PbGl [KB05].

5.1.10   Statistical and Systematic Uncertainties

Due to the statistical nature of the neutral pion measurement it is not sufficient
to only regard the extracted neutral pion signal S for each p_{T}-bin. As detailed
in [KB04], it is necessary to account for the individual statistical errors of the mea-
sured number of two-photon pairs N and the uncorrelated background B as well.
These quantities can be related by

$$S = N - B. \tag{5.12}$$

The background cannot be measured directly, but is approximated using so-called
mixed events, where photons from uncorrelated events are used in the reconstruction
of the invariant mass. Their number M is then scaled by a factor k to describe the
background.

$$B' = k \cdot M. \tag{5.13}$$

For the expected values $\langle B \rangle = \langle B' \rangle$ holds, so that the signal can be approximated
by

$$S' = N - B' = N - k \cdot M. \tag{5.14}$$

In order to determine the correct statistical error, we apply an error propagation to
Equation 5.14, which yields:

$$\sigma^2(s') = S' + B' + \sigma^2(k) \cdot M^2 + k^2 \cdot M. \tag{5.15}$$

The statistical error of the neutral pion extraction therefore also includes a contri-
bution from the statistical uncertainty of the background scaling.

The different corrections applied in this analysis are not precisely known and
therefore contribute to the systematic uncertainty of the measurement. Two major
factors determine the uncertainty in the extraction of the neutral pion peak: the fit
function used to parameterize the combinatorial background and the width of the
extraction window. The strong influence of the energy smearing in the detector on

the energy scale is the largest uncertainty at high p_T, together with the uncertainty in the efficiency, which comprises several contributions: we compare the corrected yields for the different PID cuts and we estimate the uncertainty in the Monte-Carlo simulation by varying the numerical values of the input parameters. The total systematic uncertainty of the yield is computed as the quadratic sum of these contributions summarized in Table 5.4.

	2.5 GeV	5.0 GeV
Peak Extraction	5%	5%
Extraction Window	2%	2%
Energy Scale	4.1%	12.9%
Conversion Correction	2.9%	2.9%
Acceptance	2.5%	2.5%
Efficiency	10%	10%
Total Uncertainty	12.7%	17.6%

Table 5.4: Systematic uncertainties of the neutral pion analysis.

5.1.11 Fully Corrected Lorentz-Invariant Yields

Neutral pion spectra for 7 different centrality classes and an additional minimum-bias sample, as shown in Figure 5.7, are extracted from the data. They are plotted as fully corrected Lorentz-invariant yields $\frac{1}{2\pi p_T N_{\text{inel}}} \cdot \frac{\Delta N}{\Delta p_T \Delta y}$, where N_{inel} is the number of measured inelastic events, ΔN the total number of neutral pions detected per transverse momentum interval Δp_T and rapidity interval Δy.

The yield can be related to the Lorentz-invariant cross-section by

$$E\frac{d^3\sigma}{d\overrightarrow{p}^3} = \frac{1}{2\pi p_T N_{\text{inel}}} \cdot \frac{dN}{\Delta p_T \Delta y} \cdot \sigma_{\text{inel}}.$$

For the most central class, data points up to $p_T = 5$ GeV/c could be obtained, in the most peripheral class up to $p_T \leq 3.25$ GeV/c due to the lower amount of events available.

The comparison of the results from the PbGl and the PbSc detector presented in Figure 5.8 shows that the results obtained from the two detectors are in good agreement. The fluctuations of the ratio, which can be attributed to the statistical limitation of the available data, do not allow drawing conclusions on a systematic difference between the two detectors observed in other analyses, e.g. [KB04, Lue07].
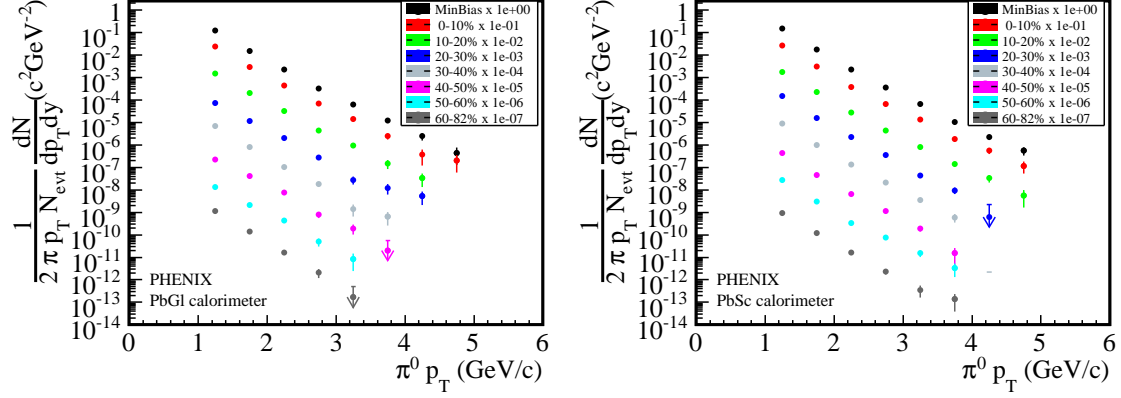
Figure 5.7: Fully corrected yields of neutral pions, measured with the lead-glass calorimeter (left panel) and the lead-scintillator calorimeter (right panel) of the PHENIX experiment.
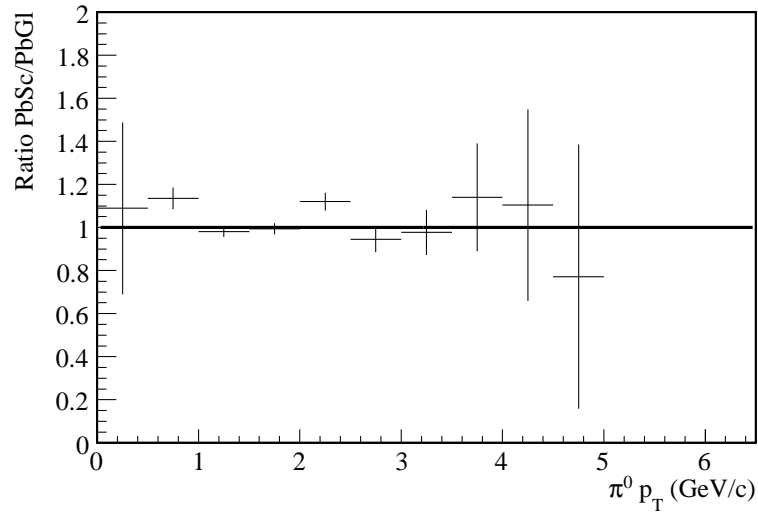
Figure 5.8: Ratio of the minimum bias yield measured with PHENIX PbSc detector compared to the measurement with the PbGl detector.

5.1.12   Combination of Detectors

The results for the PbGl and the PbSc are combined to a single result for the EMCal using a standard weighted least-squares procedure, which is described in [Yao06, Bau06]. For each data point, the average $\bar{x}$ of the two detectors is computed from

$$\bar{x} \pm \delta\bar{x} = \frac{\sum_i \omega_i x_i}{\sum_i \omega_i} \pm \left(\sum_i \omega_i \right)^{-1/2} \tag{5.16}$$

with

$$\omega_i = \frac{1}{(\delta x_i)^2}.$$

For the two separate measurements the statistical uncertainties δx_{sta} and systematic uncertainties δx_{sys} are added in quadrature:

$$\delta x_{tot} = \sqrt{(\delta x_{sta})^2 + (\delta x_{sta})^2}.$$

With this method this propagation of the errors remains valid for the combined yield.

The quality of these combined results is evaluated by computing the χ^2 for each data point, which is given by

$$\chi^2 = \sum_i \omega_i (\bar{x} - x_i)^2. \tag{5.17}$$

If the assumption holds that the errors follow a Gaussian distribution, a value of $\chi^2 \leq N - 1$ is expected, where N gives number of degrees of freedom. For the small number of data points, for which this expectation is exceeded significantly, an additional scale factor S is applied to adjust the combined total error:

$$S = \sqrt{\chi^2/(N-1)}. \tag{5.18}$$

The combined results on neutral pion yields measured with the full PHENIX EmCal are shown in Figure 5.9. They are discussed and compared to other experimental results in Chapter 7.
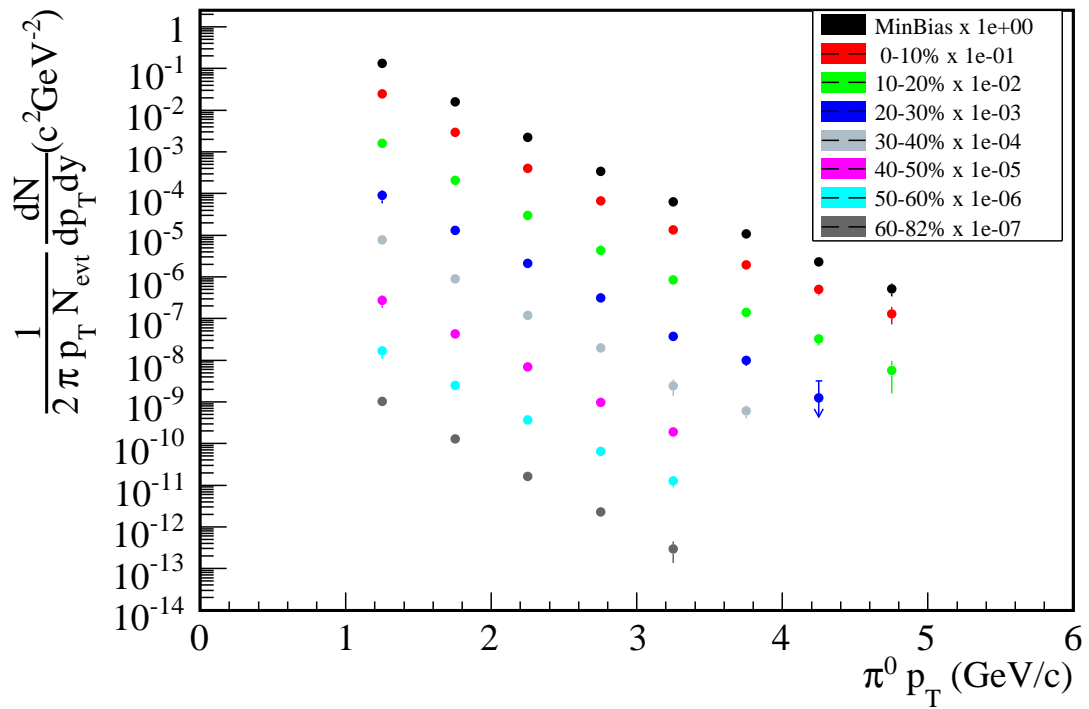
Figure 5.9: Fully corrected yields of neutral pions produced in Cu+Cu collisions at a center-of-mass energy per nucleon pair of 22 GeV from the combination of the results obtained with the two PHENIX calorimeters.

5.2 WA98 Measurements of the Neutral Pion Production in p+Pb and p+C Collisions

WA98 utilized two different target materials in 1996 to record data from collisions with a secondary beam containing a mixture of protons and positively charged pions at an energy of 160 GeV: carbon and lead. For these two data sets no final results on the neutral pion production have been published yet. The general concept for the analyses of these two data sets presented here is very similar to that of the PHENIX analysis presented above. Preliminary results were subject of the diploma thesis of Markus Rammler [Ram07].

Attempts to analyze the neutral pion and direct photon production in the two p+A data sets have been carried out earlier, preliminary results are presented in [MC02, Rey99]. For this analysis, a new analysis program has been developed on the basis of the code employed in the analyses of the Pb+Pb data [Blu98, Buc99].

5.2.1 Data Selection and Quality Assurance

The data from the WA98 proton beam-time is sub-divided into four large segments: the lead-target data-set, the carbon-target data-set and two data sets recorded without target during the p+Pb and p+C run, respectively in order to allow the quantification of reactions outside of the target.

The WA98 DSTs contain data samples taken with different trigger conditions as described in Chapter 4.1.4. In this analysis we use two trigger conditions: the Minimum-Bias trigger (MB) and the High-Energy-Photon trigger (HEP).

Each data-set is subdivided into several runs. In a first step, global properties of the runs are evaluated. Runs in which the mean energy detected in the LEDA calorimeter or the interaction probability deviate strongly from the average result are not included in the analysis. The runs passing this quality criteria are listed in Appendix B.2. A minimum number of working readout channels of 9000 is required as well as a mean number of clusters below 200. These numbers are saved in each DST during the data production, the conditions are checked during the analysis.

For each event, the beam particle has to be identified consistently by both Cherenkov detectors to differentiate the proton induced from the π^+ induced reactions.

5.2.2 Bad Module Maps

The main detector employed in the neutral pion analysis is the LEDA calorimeter. Defective modules can cause signals which are erroneously registered as photon

target-type	E^{min} [GeV]	E^{max} [GeV]	P_{int}^{min}	P_{int}^{max}
p+Pb	2.2	2.6	0.002	0.0028
p+C	2.7	3.0	0.017	0.0022
No Target (p+Pb)	1.3	1.7	0.0002	0.0007
No Target (p+C)	1.5	2.5	0.0025	0.0035

Table 5.5: Runs for which the mean value of the energy per event or the interaction probability exceed the values given in this table are excluded from the analysis. The two No-Target data sets have been obtained during or directly after the the data-taking phase with the denoted target. Due to the different event characteristics, lower thresholds for the two observables have been determined for these runs.

hits. To remove such detector modules from the data samples, we use so-called bad module maps similar to the method employed at PHENIX. Several modules which were known to be defective have already been excluded during data taking and the DST-production. However, when comparing the number of hits per module, it can be seen that some detector towers are significantly more often active than the average. This can, e.g., be attributed to defective photomultipliers or electronic noise on the module. To remove such modules from the analysis, we exclude every module in which the number of hits exceeds the average of its eight direct neighbors by a factor of more than 2.5. The excluded modules are shown in Appendix C.2.

5.2.3   Particle Identification Cuts

To reduce the contribution of non-photonic hits in the LEDA detector, we apply similar Photon Identification Cuts (PID) as to the PHENIX data: an energy cut on hits with an energy of less than 750 MeV and a dispersion cut on the second moment of the cluster as described in [Blu98]. The dispersion is computed for the x- and the y-direction on the detector surface from Equation 5.4. The maximum $D_{max}^{cor} = \max\left\{D_x^{cor}, D_y^{cor}\right\}$ is used to define the dispersion cut:

$$
D_{max}^{cor} < \begin{cases} 0.267 & \text{if } E < 10\text{GeV} \\ 0.167 + 0.01 \cdot E & \text{if } E \geq 10\text{GeV} \end{cases} . \tag{5.19}
$$

The dispersion cut reduces the hadronic contamination by 75% and only removes 1% of the photons [Blu98]. The energy cut has been introduced to reject minimum-ionizing particles, which do not create a hadronic shower and therefore cannot by rejected via the shower shape.

5.2.4   Extraction of the Neutral Pion Peak

The principles of the neutral pion analysis in WA98 and in PHENIX are very similar, as the same mixed event approach is employed for both experiments: the invariant mass is computed for all photon pair combinations as a function of the reconstructed $p_{\rm T}$, as described above, as well as a mixed event distribution calculated by combining photons from different events. Similar photon hit multiplicities in the LEDA detector are required for the events used in the mixing procedure, as described in Chapter 5.1.5, to obtain a background distribution which yields a good description of the real background. As for the PHENIX data, the mixed-event distribution is scaled to the background of the neutral pion peak by fitting the ratio of real events to the mixed events in a region outside the expected peak for each $p_{\rm T}$-interval. The scaled mixed-event distribution is subtracted from the real distribution to obtain the neutral pion peak.

The shape of this peak deviates from the expected simple Gaussian. This has already been observed in earlier analyses of the WA98 data [Blu98] and could be attributed to interactions of the beam particles behind the target. In the calculation of the invariant mass it is assumed that all measured particles originate from the target region. For particles produced further downstream a wrong angle between the two decay photon pairs from neutral pions produced in such off-target collisions is reconstructed, which yields a too small value for the invariant mass. The distributions of the reconstructed invariant mass for neutral pions produced in the target and those produced in off-target collisions overlap. Therefore no simple cut on the invariant mass can be introduced to remove this contamination without removing a significant fraction of neutral pions produced in the target.

The *little veto detector* was introduced into the setup between the p+Pb and the p+C beamtime to reduce these unwanted contributions. Additionally, for the two run periods data without a target was taken to quantify off-target events which cannot be rejected by the avilable veto-detectors. The malformed neutral pion peak reconstructed from these events, in the following referred to as no-target peak, is used to correct the data from runs with the target in place for background from interactions outside of the target.

In a first step, the no-target peak from each $p_{\rm T}$-bin is scaled according to the ratio of the interaction probability of the corresponding data sets with and without target. The interaction probability can be calculated from the ratio of the number of recorded minimum bias events n_{mb}^{ai} and high-$p_{\rm T}$ triggered events n_{high}^{ai} to the total number of beam particles passing through the experiment n_{beam}^{ai}, the index ai denotes that the values have been recorded *after inhibit*. The inhibit signal is generated, when the experiment is not able to record data, thereby the dead-time

	p+Pb	p+C	No Target (p+Pb)	No Target (p+C)
n_{mb}^{ai}	58.6	244.9	1.5	6.9
n_{high}^{ai}	1.29	2.7	0.008	0.25
n_{beam}^{ai}	24.9	12.7	3.9	2.3
p_{mb}^{int}	0.23%	1.93%	0.04%	0.3%
p_{high}^{int}	0.0052%	0.02%	0.00021%	0.01%

Table 5.6: Number of recorded events and beam triggers, together with the resulting interaction probabilites.

of the setup is taken into account. Table 5.6 shows the values obtained from the WA98 database, in which the beamtrigger data was saved.

When the scaled no-target peak is subtracted from the result obtained with a target, it does not completely remove the contamination of off-target particles from the data. The exact source of this additional contribution has not been fully explained, it can, e.g., be attributed to a modification of the beam shape in the target, which enlarges the amount of particles produced outside of the target. As the position and width of the contamination in the data recorded with a target in place are described well by the off-target peak, the source of this additional contribution is well understood.

To improve the subtraction of the off-target contribution, a correction factor for the normalization of the off-target peak S_F is determined, such that the observed deviation of the neutral peak from a Gaussian shape is removed in the p+Pb and p+C data: the neutral pion peak from the data obtained with a target is integrated for $0.2 < p_\mathrm{T} < 2.8$ GeV/c and fitted with a sum of two Gaussians. The first one is fixed to the width and the position of the off-target peak with only the height as free parameter h_fit, for the second Gaussian all parameters are free. Together with the height of the measured off-target peak h_meas, we can calculate the correction factor $S_\mathrm{F} = h_\mathrm{fit}/h_\mathrm{meas}$. A value of $S_\mathrm{F} = 2.55 \pm 0.38$ was extracted from the p+C data set and confirmed to be applicable to the p+Pb data. The uncertainty is determined by varying the p_T interval for the fit.

Figure 5.10 shows the uncorrected neutral pion peak, the off-target peak scaled only by the ratio of the interaction probabilities of the data sets with and without target and the off-target peak with an additional scaling by S_F. In a similar approach applied to the Pb+Pb data published earlier, a correction factor of 2.26 ± 0.16 was extracted [Blu98], in good agreement with the result obtained here for the
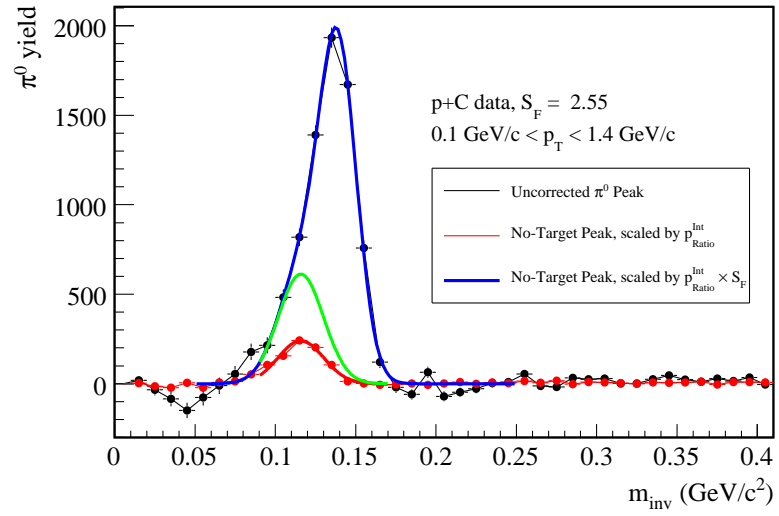
Figure 5.10: Correction of the neutral pion peak for particles produced outside the target in the WA98 setup. The uncorrected neutral pion peak integrated over $0.2 \text{ GeV}/c < p_T < 2.8 \text{ GeV}/c$ is shown in black, the peak measured in the runs without target, scaled by the ratio of the interaction probabilities in the run with and without target, in red. The green curve shows the fit to the off-target data, scaled additionally by the factor $S_F = 2.55$, which is necessary to describe the off-target contribution empirically.

p+A data. For the minimum bias sample, the neutral pion yield per event, corrected for the off-target contribution, is given by

$$\frac{1}{n_{\text{mb}}^{\text{corr}}}\frac{dN_{\pi^0}^{\text{corr,mb}}}{dp_{\text{T}}} = \frac{1}{(1-S_{\text{mb}})n_{\text{mb}}^{\text{ana,T}}}\left(\frac{dN_{\pi^0}^{\text{mb,T}}}{dp_{\text{T}}} - S_{\text{F}}\cdot S_{\text{mb}}\cdot\frac{n_{\text{mb}}^{\text{ana,T}}}{n_{\text{mb}}^{\text{ana,noT}}}\cdot\frac{dN_{\pi^0}^{\text{mb,noT}}}{dp_{\text{T}}}\right)$$

$$(5.20)$$

where

$$S_{\text{mb}} = \frac{p_{\text{int,mb}}^{\text{noT}}}{p_{\text{int,mb}}^{\text{T}}} = \frac{n_{\text{mb}}^{\text{noT}}/n_{\text{beam}}^{\text{noT}}}{n_{\text{mb}}^{\text{T}}/n_{\text{beam}}^{\text{T}}} \tag{5.21}$$

accounts for the different interaction probabilities in the two data sets.

To increase the relative amount of events with a high-p_{T} trigger decision in the data sample, only a fraction of the minimum bias events is recorded. In order to merge the minimum bias data with the triggered data, this scale-down of the minimum bias data has to be accounted for by multiplying the high-p_{T} triggered yield with the fraction of minimum-bias events that are also flagged as high-p_{T} events:

$$\frac{1}{n_{\text{mb}}^{\text{ana}}}\frac{dN_{\pi^0}^{\text{high}}}{dp_{\text{T}}} = \frac{1}{n_{\text{hep}}^{\text{ana}}}\frac{dN_{\pi^0}^{\text{high}}}{dp_{\text{T}}}\cdot\frac{n_{\text{mb}\wedge\text{high}}^{\text{ana}}}{n_{\text{mb}}^{\text{ana}}}. \tag{5.22}$$

Together with Equation 5.20, the corrected high-p_{T} yield is given by

$$\frac{1}{n_{\text{mb}}^{\text{corr,ana}}}\frac{dN_{\pi^0}^{\text{corr,high}}}{dp_{\text{T}}} = \frac{1}{(1-S_{\text{high}})n_{\text{high}}^{\text{ana,T}}}$$
$$\left(\frac{dN_{\pi^0}^{\text{T}}}{dp_{\text{T}}} - S_{\text{F}}\cdot S_{\text{high}}\cdot\frac{n_{\text{high}}^{\text{ana,T}}}{n_{\text{high}}^{\text{ana,noT}}}\cdot\frac{dN_{\pi^0}^{\text{high,noT}}}{dp_{\text{T}}}\right)\cdot\frac{n_{\text{mb}\wedge\text{high}}^{\text{ana}}}{n_{\text{mb}}^{\text{ana}}} \quad (5.23)$$

with

$$S_{\text{high}} = \frac{p_{\text{int,high}}^{\text{noT}}}{p_{\text{int,high}}^{\text{T}}} = \frac{n_{\text{high}}^{\text{noT}}/n_{\text{beam}}^{\text{noT}}}{n_{\text{high}}^{\text{T}}/n_{\text{beam}}^{\text{T}}}. \tag{5.24}$$

In Figure 5.11 the minimum bias yield is compared to the high-p_{T} triggered yield. For the final spectra both yields are combined. The high-p_{T} trigger reaches its full efficiency at $p_{\text{T}} \approx 1.5$ GeV/c. This data set is used for $p_{\text{T}} > p_{\text{T,cut}} = 1.7$ GeV/c. For these transverse momenta the statistical uncertainty in the minimum bias sample exceeds the uncertainty in the enriched data sample. The combined yield is given by

$$\frac{1}{n_{\text{evt}}}\frac{dN_{\pi^0}}{dp_{\text{T}}} = \begin{cases} \frac{1}{n_{\text{mb}}^{\text{corr}}}\frac{dN_{\pi^0}^{\text{corr,mb}}}{dp_{\text{T}}} & p_{\text{T}} < p_{\text{T,cut}} \\ \frac{1}{n_{\text{mb}}^{\text{corr,ana}}}\frac{dN_{\pi^0}^{\text{corr,high}}}{dp_{\text{T}}} & p_{\text{T}} \geq p_{\text{T,cut}} \end{cases}. \tag{5.25}$$

In total, $1.0\cdot 10^6$ minimum bias events from the p+Pb data set and $1.2\cdot 10^6$ from the p+C data set are analyzed. For the high-p_{T} trigger condition, the $0.5\cdot 10^6$
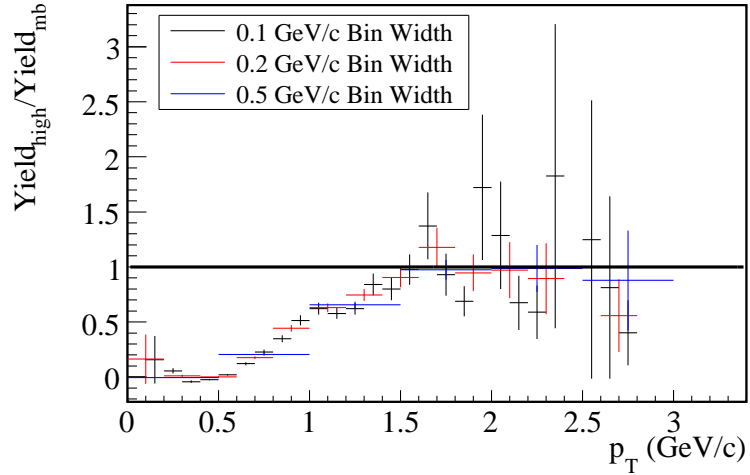
Figure 5.11: Ratio of the high-p_T triggered data to the minimum bias data for three different bin widths used in the WA98 analysis. The trigger is fully efficient for $p_T \gtrsim 1.5$ GeV/c.

analyzed p+Pb events correspond to $8.2 \cdot 10^6$ minimum bias events. The p+C data sample contains $1.5 \cdot 10^6$ events with high-p_T trigger, corresponding to $3.9 \cdot 10^7$ minimum bias events.

5.2.5   Corrections of the Yield

To obtain a physically correct neutral pion yield from the extracted signal, several corrections are applied to the data. The determination of these corrections is discussed in the following.

Geometrical Acceptance

We employ a modified version of the Monte Carlo simulation described in Chapter 5.1.7 to determine the geometrical acceptance. Unlike in the PHENIX analysis presented above, the acceptance correction used in earlier WA98 analyses only accounts for the geometrical coverage of the entire LEDA detector, dead modules are considered later in the efficiency correction. This definition has been used for the analysis presented here to allow the comparison to earlier WA98 results. The acceptance for neutral pions is shown in Figure 5.12.
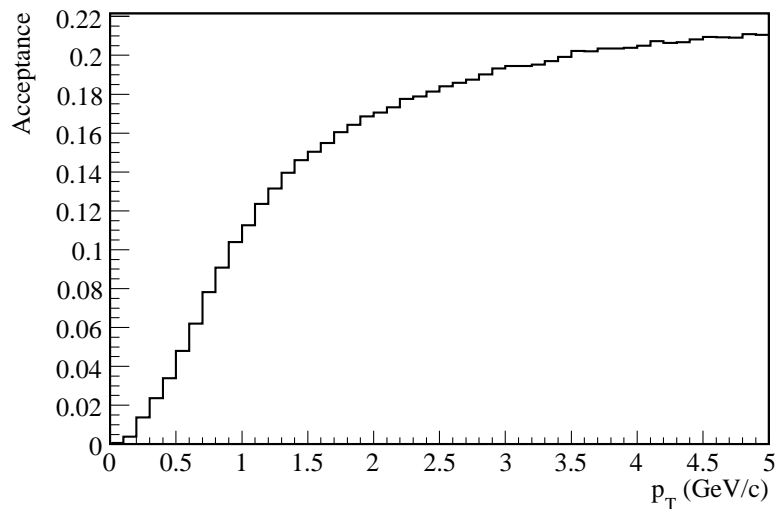
Figure 5.12: Acceptance for the two-photon decay of neutral pions , calculated in a rapidity interval $2.0 < y < 3.2$ which includes the full WA98 LEDA detector.

Efficiency Correction

For the determination of the efficiency two independent methods are utilized: besides the information from the Monte Carlo simulation, which is similar to the method used for the PHENIX data, events generated by GEANT3 [GEA09] have been embedded into the DST files and can be used to determine the efficiency correction for the detector. A detailed description of the embedding procedure is given in [Blu98]: in the GEANT simulation, neutral pions have been created with uniform distributions of $0 \text{ GeV}/c \leq p_\mathrm{T} \leq 5 \text{ GeV}/c$ and $2.0 \leq y \leq 3.2$. Each measured event has been combined with one GEANT event. These have been produced simultaneously to the data production. Some GEANT events have been embedded multiple times into different measured events, as the data reconstruction proceeded faster than the simulation. Each GEANT event contains one neutral pion. The photonic decay and its detection was simulated with the GWA98 package [Bue02], which uses a parameterization of the effects in the LEDA detector to generate the simulated signal of the photons. To reduce computing time this signal was only computed for events, in which both decay photons were found within a pseudorapidity region slightly larger than the acceptance of the LEDA detector. If this condition was not fulfilled, the randomly simulated decay was repeated up to 10 times. During the DST production, these GEANT events are reconstructed using the same algorithms that are used for the measured data. Each simulated photon pair is reconstructed

from the empty detector matrix and saved in the DST. Furthermore, a copy of the real event is overlapped with the simulated photon signals before reconstruction, so that the DST holds three sets of information for each event: the real LEDA data of the full event, the simulated GEANT events consisting of one pion and its two decay photons and the reconstruction of these two photons from the overlap with the full event.

The width of the neutral pion peak from the simulated events does not fully reproduce the measured value. Therefore, an additional Gaussian smearing of the energy is introduced [Blu98]. The width of this smearing is given by

$$\sigma_{\text{smear}} = 4.8\% + \frac{4.8\%}{\sqrt{E}}. \tag{5.26}$$

To determine the efficiency, we fill histograms for two types of GEANT information: for each GEANT decay photon pair, where both photons hit the LEDA surface, we determine the transverse momentum of the original neutral pion and record it in a histogram as a function of this p_{T}. The original pion distribution is uniformly distributed in p_{T} and y to enhance the statistics for events with high transverse momentum. In order to obtain a more realistic simulated spectrum a weight w_{Eff} is applied to each event, which is given by

$$w_{\text{Eff}} = w_{\text{p}_{\text{T}}} \cdot w_{\text{y}} \cdot w_{\text{N}} \cdot w_{\text{Sim}}. \tag{5.27}$$

$w_{\text{p}_{\text{T}}}$ is given by a fit to the fully corrected neutral pion spectrum to account for the steeply falling shape. This weight is determined through an iterative process. To approximate the real rapidity distribution of the particles, a Gaussian distribution with the center at $y = 2.9$ and a width of $\sigma = 1.4$ according to [Jon96] is used as w_{y}. The w_{N} factor compensates for the fact that events with high multiplicity would not be represented correctly, because only one photon pair is overlayed with each event, regardless of its multiplicity. To account for this, $w_{\text{N}} = N$, where N is the event multiplicity measured by the LEDA detector, is used.

As mentioned above, only GEANT decays are accepted for the embedding procedure, in which both decay photons are within a restricted rapidity region narrowly including the LEDA acceptance or where the decay has already been repeated 10 times. Due to this limitation a wrong probability for this event would be asssumed. To correct for the number of repetitions of the decay N_{Sim}, the weight $w_{\text{Sim}} = 1/N_{\text{Sim}}$ is applied.

For the reconstructed hits from the overlayed events both photons do not only have to be on the LEDA surface, but on active modules to account for those modules excluded from the analysis. To the hits fulfilling this condition the same PID and

asymmetry cuts as to the measured data are applied. For the reconstructed mass of the simulated neutral pions, the same deviation from the expected value as for the measured data is allowed. The GEANT event is then counted with the weight w_{Eff} for each set of cuts it fulfills the critera for.

To determine the efficiency correction for a given PID class, the according histogram for the GEANT hits reconstructed from the overlayed event is divided by the histogram of the original GEANT hits.

To verify the results from these embedded events independently, a Monte Carlo simulation is employed analogously to the PHENIX analysis to determine the efficiency correction. The simulation is the same as used for the determination of the acceptance. A fit to the neutral pion spectrum is used as an input, which is improved iteratively. The energy smearing is adjusted empirically to describe the experimentally determined width of the neutral pion peak. This distribution is sampled to generate and simulate the decay of neutral pions. The decay photons are then subjected to the same cuts as the data (PID, asymmetry and dead modules). The efficiency correction can be determined as a quotient of the registered simulated decay photons and the decay photons on the surface of the detector.

A comparison of the results from the Geant particles and the Monte Carlo simulation is shown in Figure 5.13. The results obtained with the two different methods are in good agreement.
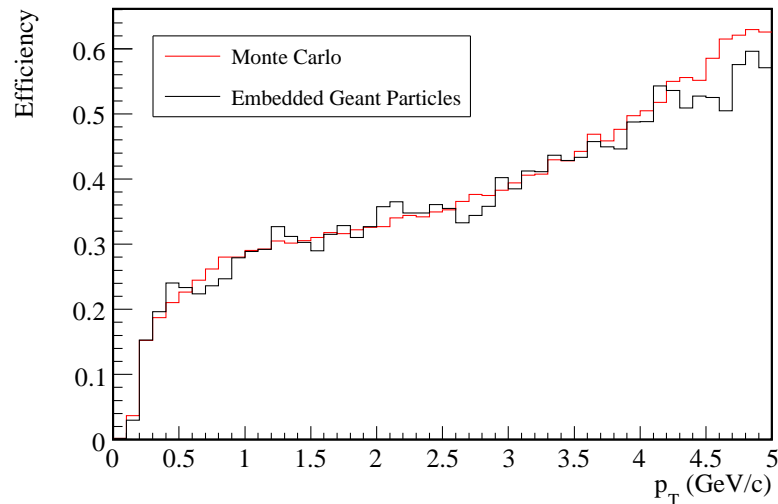
Figure 5.13: Comparison of the efficiency corrections derived from the embedded photons and the Monte Carlo simulation for the WA98 setup.

Correction of the Energy Scale

With the adjusted smearing of the energy of the Geant particles and in the Monte Carlo simulation, the width of the neutral pion peak can be reproduced well. The position of the peak, however, deviates slightly from the expected value. This points to an overall uncertainty in the energy scale of the detector. For the Pb+Pb beamtime in 1996, a correction factor for the hit energy of 1.035 for the upper and 1.044 for the lower half of the LEDA detector was introduced [Blu98]. This effectively removes the difference between the two detector parts in the p+A data samples. From the comparison to simulations an additional correction factor for the measured hit energy of 1.017 for both parts of the LEDA detector is determined for the p+A data. Figure 5.14 shows the agreement between te experimental results and the two simulations.
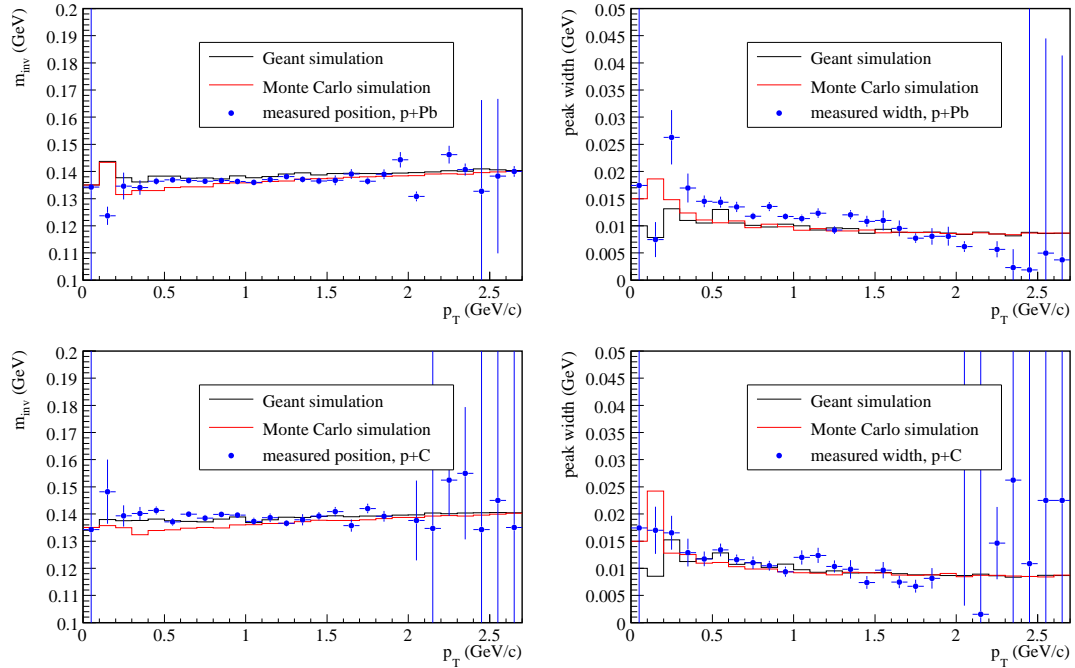
Figure 5.14: In the left column the mean position of the neutral pion peak from the WA98 measurements is shown, in the the right column the width of the energy peak is displayed. The results for p+Pb are shown in the upper row, the results from the p+C data set in the lower row. The slight underestimation of the width in p+Pb data can be related to artifacts from off-target correction.

Additional Corrections

In analogy to the PHENIX analysis described above, the neutral pion yield is normalized to the bin width of the spectrum, the rapidity interval $\Delta y = 1.2$ assumed

in the acceptance correction and the branching ratio of the $\pi^0 \rightarrow 2\gamma$ decay. The necessary conversion correction has been studied in detail in [Blu98]. The data used for this analysis was recorded with the GOLIATH magnet switched off. Without a magnetic field, the electron-positron pairs created in a conversion are not separated significantly when arriving in the LEDA detector. The resulting shower retains a shape similar to a photonic shower due to the overlap of the two particles and also contains the full energy. Therefore, the conversion correction for p+Pb data is 0.6% and 0.5% for the p+C data.

Finally, the bin shift correction described in Chapter 5.1.8 also is applied to the neutral pion spectra. An exponential fit to the data is used as input function.

5.2.6   Systematic Uncertainties

The total systematic uncertainty is given as the quadratic sum of the individual uncertainties assigned to the different steps of the determination of the total yield. It is split into the following contributions: the choice of the extraction window, the quality of the normalization fit for the combinatorial background, the choice of the size of the depletion window used for the fit to the background and the conversion correction. The error of the off-target correction is also included here. None of these contributions exhibit a dependence on p_T. The values of these contributions, together with exemplary values for the other sources of systematic uncertainties discussed in this section, are given in Table 5.7.

The necessary corrections of the energy scale introduce another important systematic uncertainty. We assume a remaining uncertainty of 1.5%, which is attributed to the limitations of the ADC. For the neutral pion yield, this would translate to a shift in p_T. The uncertainty of the yield can be estimated by dividing the original yield by the shifted yield. Under the assumption of an exponential shape of the spectra, the uncertainty can be expressed by

$$\varepsilon_{\mathrm{E-scale}}(p_T) = 1 - \frac{1}{(1+\kappa)^2}\exp^{\left(-\frac{1}{\kappa}\cdot\frac{p_T}{0.2}\right)}, \qquad (5.28)$$

with an assumed uncertainty of the energy scale of $\kappa = 0.015$. The uncertainty of the acceptance correction depends on the accurate representation of the detector surface. By varying the surface in the Monte Carlo simulation, a p_T independent uncertainty of 2.5% is obtained.

For the efficiency correction, the systematic uncertainty arises from different sources. For the energy and the dispersion cut, we compare the fully corrected spectra without the respective cut to fully corrected spectra with both cuts. While the uncertainty of the dispersion cut does not depend on the p_T of the neutral

	1.25 GeV	2.9 GeV
Peak Extraction	5.5%	5.5%
- Depletion Window	3%	3%
- Extraction Window	4%	4%
- Background Fit	2.3%	2.3%
- off-target Correction	0.5%	0.5%
Energy Scale	6.5%	20.3%
Acceptance	2.5%	2.5%
Efficiency	8.9%	18.3%
- Energy Cut	5.4%	3.6%
- Dispersion Cut	6.8%	6.8%
- Asymmetry Cut	1.8%	16.2%
- Energy Smearing	0.02%	3.5%
- Conversion Correction	0.5%	0.5%
Total	12.6%	28.0%

Table 5.7: Systematic uncertainties of the neutral pion measurement (WA98, p+A).

pion, the uncertainty of the energy cut is most relevant for small p_T. Similarly, the uncertainty on the asymmetry cut, which is most relevant for $p_T > 2$ GeV, is determined. The uncertainty of the energy smearing is also included here. The iteratively determined energy smearing in the Monte Carlo simulation described above is varied by $\pm 2\%$. A fit to the ratio of the simulated spectra with and without additional smearing is used to quantify this contribution.

5.2.7 Fully Corrected Spectra

Neutral pion yields shown in Figure 5.15 have been extracted from both the p+Pb and p+C dataset for transverse momenta beween 0.7 GeV/c and 3.5 GeV/c which thereby reach into the p_T-regime where hard parton-parton scattering processes start to dominate. In Chapter 7 these new datasets are compared to the available results and the implications for a possible suppression signal are discussed.

5.2.8 Production of η-Mesons

Similar to the neutral pion, the η-meson can be measured via a two-photon decay, which has a branching ratio of 39.38% [Ams08]. With only small modifications, the
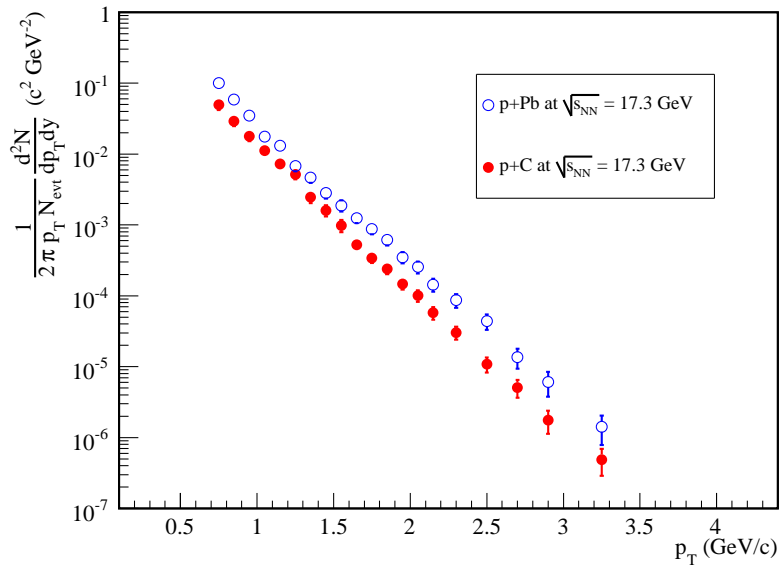
Figure 5.15: The fully corrected Lorentz-invariant neutral pion yields in p+Pb and p+C collisions at $\sqrt{s_{\mathrm{NN}}}$ = 17.3 GeV, measured with WA98. The error bars indicate the total uncertainty of yield.

analysis framework described above for the neutral pion analysis can be utilized to extract the yield of the η-meson:

The peak extraction as well as the efficiency and acceptance are adjusted to the mass $m_{0,\eta} = 547,853$ MeV of the η-meson. For the determination of the efficiency the Monte Carlo analysis is used since no embedded η-mesons generated from Geant were embedded into the DSTs. Here, significant data points can only be obtained from the high-p_T triggered sample of the p+C data. The fully corrected Lorentz-invariant yield is shown in Figure 5.16. Although the uncertainties on the yield are large, this results can be used to verify the p_T-dependent ratio of η-mesons to neutral pions, which is an important input parameter for the determination of the direct photon yield.
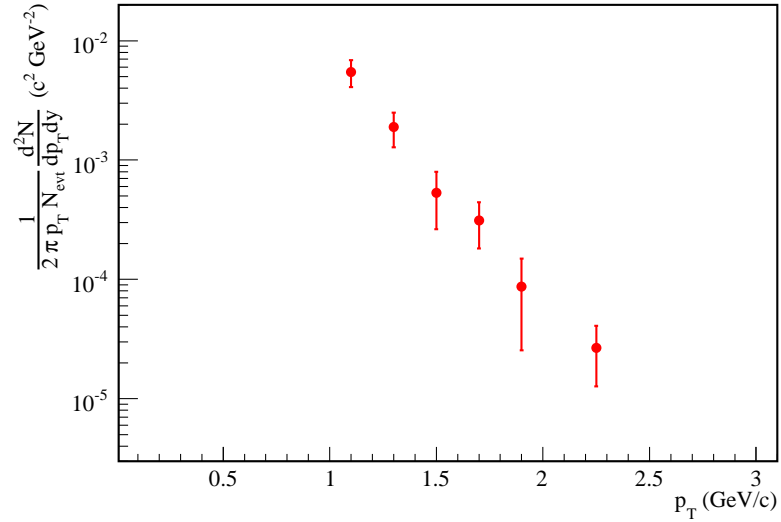
Figure 5.16: Fully corrected spectrum of the η mesons produced in p+C collisions measured with WA98. The results have been solely obtained from the high-p_T triggered data sample. The error bars indicate the total uncertainty of yield.

6. Search for Direct Photons with WA98 and PHENIX

With the neutral pion yield as baseline, the analysis of the direct photon production in the WA98 and PHENIX data sets is described in the following.

6.1 Search for Direct Photons in the WA98 p+Pb and p+C Data

The starting point for the determination of the direct photon yield is the inclusive photon spectrum measured with the LEDA calorimeter. The direct photon yield is expressed as a fraction of the inclusive photon yield.

6.1.1 Inclusive Photon Yield

The inclusive photon yield contains all photons measured with the LEDA detector and is determined on the basis of the same analysis code as the neutral pion yield with the same restrictions on the event selection as described in Chapter 5.2.1. In general, single photon yields are more easily distorted by noisy detector modules than neutral pion yields, since the measurement of correlated photons helps to reduce this unwanted influence. The measurement of photon spectra is more susceptible to the influence of defective detector modules delivering an excessive amount of hits than the measurement of neutral pions described above. The bad module maps have already been chosen rigidly enough during the neutral pion measurement so that no additional modules have to be excluded for this analysis. The PID cuts applied to reduce the amount of LEDA hits not caused by photons are also identical in both analyses.

6.1.2 Acceptance and Efficiency

The acceptance correction accounts for the limited angular coverage of the detector. It is obtained from the same Monte-Carlo simulation that is also used in the neutral pion analysis. For the measurement of the inclusive photon correction, it is independent of p_{T}, with a value of $\varepsilon_{\mathrm{Acc}} = 0.245$. The simulation is restricted to an rapidity interval $2.0 < y < 3.2$ which covers the full LEDA detector.
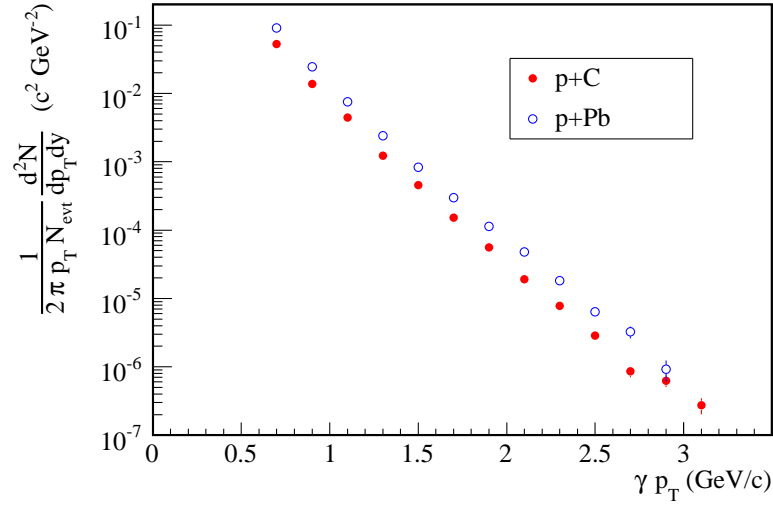
Figure 6.1: Inclusive Photon Yields in p+Pb and p+C collisions at $\sqrt{s_{\mathrm{NN}}} = 17.4$ GeV.

The efficiency correction has also been carried out similarly to the neutral pion analysis. An important difference results from the simulated photons contained in the DSTs as described above. While for the neutral pions decays have been simulated in Geant, as described above, with the results having been included in the DSTs, this has not been done for single photons. It is possible to use the simulated decay photons to determine the efficiency for this analysis, however, the p_{T} distribution of the available simulated photons, which are originally produced in simulated neutral pion decays, is not flat, when regarded as single photons. The resulting shape of the simulated spectrum with the weight w_{Eff}, described in Chapter 5.2.5, does therefore not agree with the real form of the spectrum. In order to account for this deviation, an additional weighting factor has been introduced: in a preparatory analysis of the data, the p_{T} distribution of the single Geant photons is determined and saved as a histogram. The weight for each simulated photon during the analysis of the data is multiplied with the inverse content of the corresponding p_{T}-bin from this reference histogram. This corrects for the deviations from the distorted shape of the input distribution and allows retaining the framework for the efficiency determination from the neutral pion analysis without further modifications.

In order to verify the results obtained by this method independently, a Monte-Carlo simulation, as described in Chapter 5.2.5, is employed. It uses an iteratively improved fit to the fully corrected inclusive photon spectrum as input function. The comparison of these two methods shown in Figure 6.2 reveals that the two results are in good agreement.
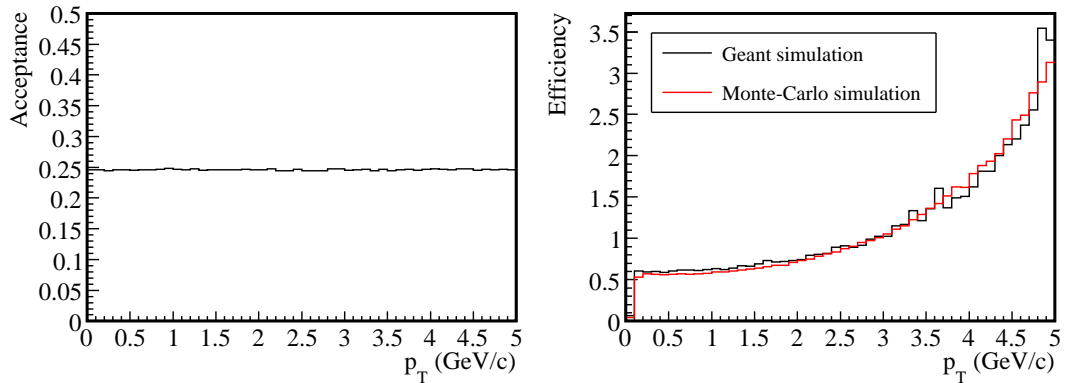
Figure 6.2: The left panel shows the acceptance correction obtained from a Monte-Carlo simulation for the inclusive photon spectrum. In the right panel the corresponding efficiency is shown exemplarily for p+Pb collisions as determined from the embedded Geant particles and from the Monte-Carlo simulation.

6.1.3   Correction for Charged Particles and (Anti-)Neutrons

For the determination of the inclusive photon spectrum it is necessary to correct for charged particles, as well as for neutrons and anti-neutrons. These corrections have not been necessary for the neutral pion measurement, as these contaminations have been effectively removed there by the measurement of correlated photons.

With the CPV detector it is possible to reject hits of charged particles, which are wrongly registered as photon hits in the LEDA detector. In principle two different methods can be employed for this: the CPV can be used on an event-by-event basis to reject hits with a signal in both the CPV and LEDA, or on a statistical basis to determine the fraction of LEDA hits that has been caused by charged particles, and to subtract this contibtion. As the CPV detector was not fully available during the measurements of the p+A run in 1996, the statistical subtraction approach as described in [Rey99] is used to determine this correction. It is summarized in the following.

For the determination of the charged particle correction, only runs in which both CPV subdetectors are available and flagged as functional in the DST and the experimental logbook are included in the analysis. Like in the case of the LEDA detectors, noisy modules are excluded in a first analysis step. Modules for which the average signal over all runs exceeds ten times the average of its neighbors are marked as faulty.

In the analysis, for each photon the closest CPV hit is identified and the distance is saved in a histogram. The same procedure is applied to the photons from the Geant simulation to quantify random veto correlations. Both distributions reflect the probability distribution for the distance d_v of a veto hit to a photon registered in the LEDA. The distance between the hits in LEDA and CPV effectively corresponds to a radius within which a real veto signal has been found. The ratio from real, correlated hits to the simulated hits is constant for a veto radius $R_v > 6$ modules. For larger distances, the observed correlations are expected to be purely random. The probability of a veto hit is given by $\left(p = \int_0^{R_v} N_{veto} d_v \right) / \left(p = \int_0^{\infty} N_{veto} d_v \right)$ by integrating either over the distance distribution of the measured photons to obtain the probability p_{veto}, or by integrating over the distance distribution of the Geant hits to obtain the probability for a random veto p_{ran}. The detection efficiency of the CPV detector is $\varepsilon_{CPV} = 93\%$ [Rey99], i.e. the number of hits from charged particles without a correlated veto is small. Therefore it is assumed that the probability for a random veto signal is the same for photons and charged particles. The number of charged hits in the LEDA detector X_{ch}^{hit} is then given by

$$X_{ch}^{hit} = \frac{1}{\varepsilon_{CPV}} \frac{p_{veto} - p_{ran}}{1 - p_{ran}}. \tag{6.1}$$

Another correction related to charged particles is the conversion of photons into electron-positron pairs as described in Chapter 5.2.5. These two contributions can be combined into a single correction X_{ch}. Hence, the photon yield corrected for charged particles $N_{\gamma,ChCorr}$ can be written as

$$N_{\gamma,ChCorr} = \frac{1 - X_{ch}^{hit}}{1 - p_{conv}} \cdot N_{LEDA} = (1 - X_{ch}) \cdot N_{LEDA},$$

where p_{conv} is the probability for the conversion of a photon and

$$X_{ch} = \frac{X_{ch}^{hit} - p_{conv}}{1 - p_{conv}}. \tag{6.2}$$

Due to the limited number of runs with full CPV information, the extracted X_{ch} only covers $p_T \lesssim 1.5$ GeV/c.

The correction for neutrons and anti-neutrons has been determined for earlier analyses of the Pb+Pb data from the full simulation of the experiment, as described in Chapter 5.2.5. The transverse momentum distributions of the neutrons and anti-neutrons obtained with the VENUS event generator have been modified to describe the measurements presented in [Jon96]. Results described in [MC02] for p+Pb and p+C collisions with different simulation packages for neutron interactions are in qualitative agreement with the results for peripheral Pb+Pb collisions, when only

an energy cut is applied, but exhibit large, non understood deviations between each other and the peripheral Pb+Pb results, when the dispersion cut is also included. Since the Geant simulation of the WA98 setup is no longer available, the simulations cannot easily be repeated.

To overcome statistical limitations of the X_{ch} correction and the lack of a reliable correction for neutrons and anti-neutrons registered in the LEDA detector, the established results obtained for the peripheral Pb+Pb data sample described in [Buc99] are also used for this analysis. From the comparison of the results for X_{ch} obtained in p+Pb and p+C collisions to the result from the Pb+Pb data shown in Figure 6.3, a constant correction factor S_{ch} of $S_{ch}^{p+Pb} = 2.2$ and $S_{ch}^{p+C} = 0.8$ can be deduced, respectively.

Two requirements need to be fulfilled in order to render the application of the scaled Pb+Pb corrections to p+A data-sets valid: it has to be shown that the assumption of a p_T independent scaling factor S_{ch} is valid also for $p_T \gtrsim 1.5$ GeV/c, where no results for X_{ch} can extracted from the p+A data. Furthermore, a scaling factor S_n for the neutron and anti-neutron correction has to be determined, where the relation to S_{ch} is not a priori obvious.

Simulations with Hijing [Hij09] and AMPT [Lin05] can be used to overcome these difficulties, although the simulations of the detector reponses are not available.

Instead of trying to determine the full correction, the differences between peripheral Pb+Pb collisions and p+A collisions is examined with these simulations. It can be assumed that the responses of the detectors are similar for events from the different colliding species so that it is possible to determine a scaling factor for the existing corrections from the simulations.

Therefore we use both event generators to simulate p+Pb, p+C and peripheral Pb+Pb collisions. The results are analyzed within the Unigen framework [Uni09], which provides a standardized interface to the output of different event generators. For each of the three colliding systems, the number of charged particles within a rapidity range corresponding to the LEDA acceptance of $2.0 < \eta < 3.2$ is determined as a function of p_T. The ratios of the number of charged particles for p+Pb or p+C events to peripheral Pb+Pb events obtained from both AMPT and Hijing do not exhibit a dependence on p_T and are consistent with the results obtained from the ratios of the X_{ch} (see Figure 6.4). From deviations between the AMPT and Hijing results, we assign a relative uncertainty of 40% to the scaling factors S_{ch} for p+Pb and p+C collisions.

We use the same simulation to determine the ratio of neutrons and anti-neutrons in p+A collisions compared to the result for peripheral Pb+Pb collisions. The ratios shown in Figure 6.4 do not exhibit a visible dependence on p_T. The scaling
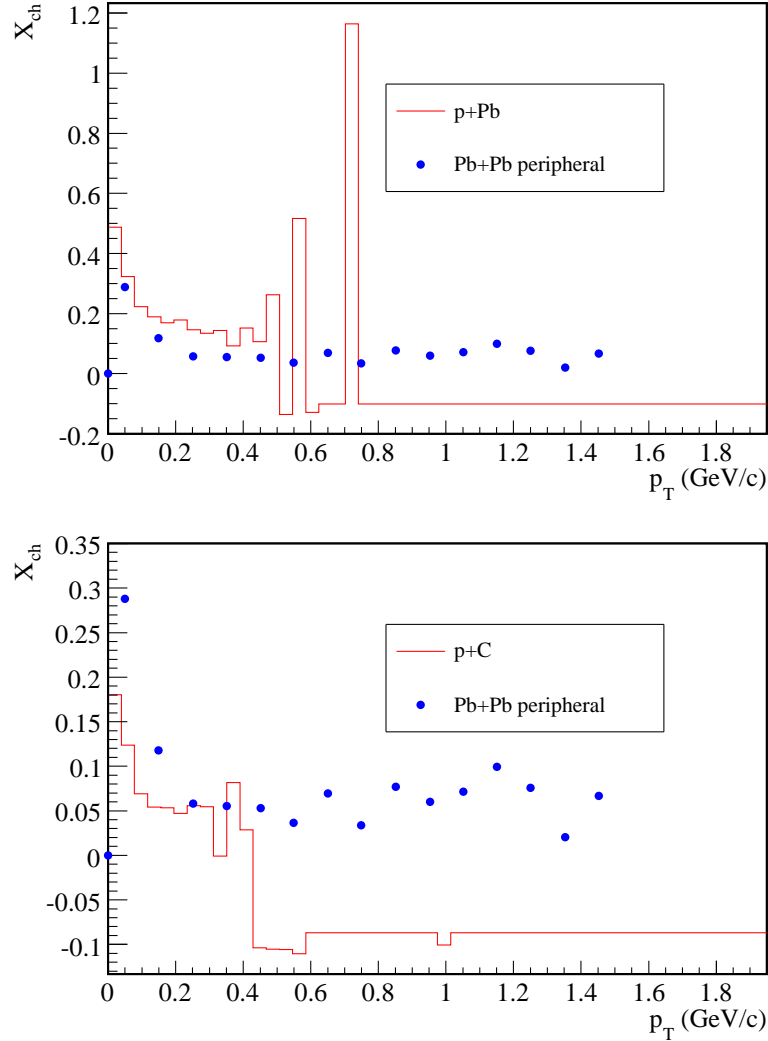
Figure 6.3: Comparison of the X_{ch} correction obtained from p+Pb (upper panel) and p+C collisions (lower panel) to the earlier results obtained in peripheral Pb+Pb collisions [Rey99]. The negative entries at high p_T are an artifact from Equations 6.2 and 6.1 in the case of a vanishing veto probability p_{veto}.

factor determined for neutrons and anti-neutrons detected as photons in the LEDA detector is in all cases compatible with the scaling factor for charged particles. The systematic uncertainty of the scaling value is consistent with the result obtained for the charged particles.

The overall uncertainty for the direct photon yield introduced by this scaling of existing corrections is small: the correction for neutrons and anti-neutrons is typically smaller than 4% of the photon yield, the additional uncertainty due to the
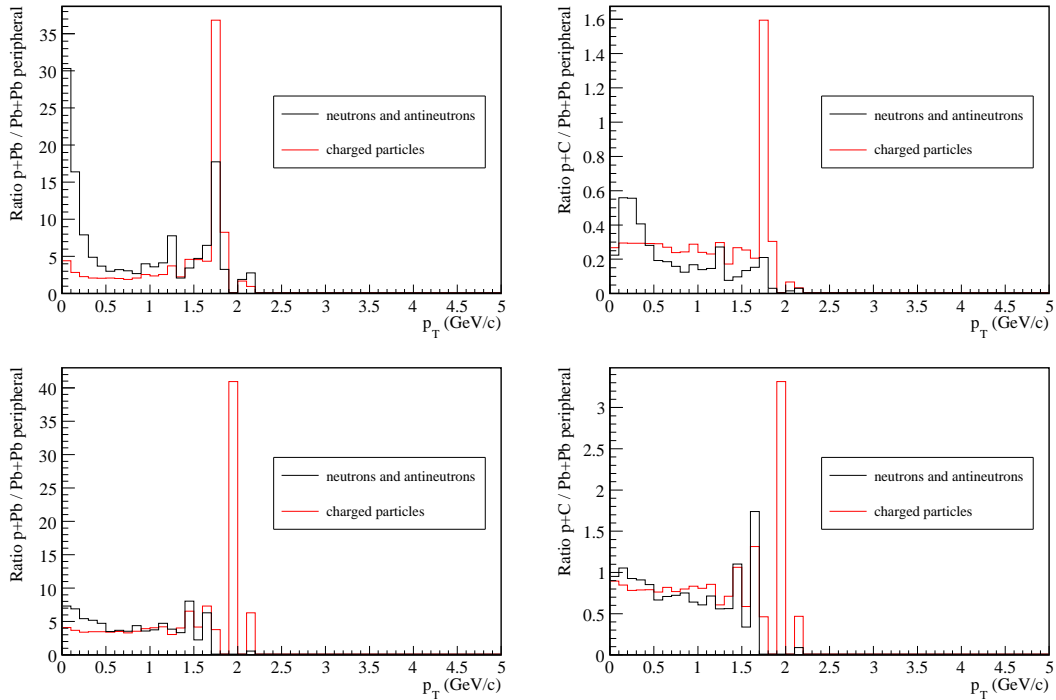
Figure 6.4: Ratio of charged particles and (anti-)neutrons in the LEDA acceptance from AMPT (upper row) and Hijing (lower row) simulations for p+A collisions to peripheral Pb+Pb collisions. The left column shows the simulations for p+Pb collisions, the right for p+C collisions.

scaling is therefore on the order of 1% for this correction, for the charged particle yield the value is slightly larger due to the magnitude of the correction.

We therefore apply the same correction factor to both the (anti-)neutron and the charged particle correction obtained from peripheral Pb+Pb collisions, the uncertainty of this scaling is reflected in the systematic error of the photon yield.

6.1.4 Additional Corrections

In order to obtain the fully corrected inclusive photon yield, all corrections applied to the neutral pion data have to be applied also to the photon spectrum: the bin-shift correction, to account for the misrepresented centers of the individual p_T-bins as described in Chapter 5.1.8, is applied with an exponential as fit function and is normalized to the angular coverage of the detector and the bin width chosen for the extraction of the photon yield.

The No-Target correction, detailed in Chapter 5.2.4, is also applied, using the inclusive photon spectra obtained from the corresponding data sample recorded without a target in place. Together with Equation 5.23, the scale-down of the

	1.25 GeV/c	2.9 GeV/c
Efficiency	8.5%	21.9%
- Dispersion Cut	8.4%	8.4%
- Energy Smearing	1.1%	20.2%
- Conversion Correction	0.5%	0.5%
No-Target Correction	2.5%	2.5%
Energy Scale	13.8%	28.7%
Acceptance	2.0%	2.0%
Charged Particles	9.2%	8.0%
(Anti-)Neutrons	5.7%	2.8%
Total	19.8%	37.2%

Table 6.1: Systematic uncertainties of the inclusive photon measurement (WA98, p+A).

high-$p_{\rm T}$ trigger is corrected for. The two data sets are combined using minimum-bias triggered data for $p_{\rm T} \leq 1.2$ GeV/c and the high-$p_{\rm T}$ triggered data for $p_{\rm T} > 1.2$ GeV/c.

6.1.5   Systematic Uncertainties of the Inclusive Photon Spectra

For the efficiency correction, the uncertainty is composed of contributions from the shower-cut, the energy smearing of the detectors, and the conversion correction. For each error described in this section characteristic values are given in Table 6.1. An uncertainty of 2% has been determined for the single photon acceptance. The uncertainty of the energy scale is derived from Monte-Carlo simulations. For the charged and the (anti-)neutron correction, the errors have been estimated on the basis of the uncertainties assumed for the correction in peripheral Pb+Pb collisions by varying the additional scaling factors within the limits allowed by the Hijing and AMPT simulations.

6.1.6   Determination of the Direct Photon Yield

As discussed in Chapter 2.8, a possible direct photon signal is small compared to the dominant background from decay photons. In this analysis, the direct photon

yield is quantified, similarly to the method presented in [Buc99], as a fraction of the inclusive yield using the ratio of the inclusive to the decay photon spectrum:

$$R = \frac{\gamma_{incl}}{\gamma_{decay}} \tag{6.3}$$

instead of calculating the difference of the measured inclusive and decay spectrum:

$$\gamma_{direct} = \gamma_{incl} - \gamma_{decay} = \left(1 - \frac{1}{R}\right) \cdot \gamma_{incl}. \tag{6.4}$$

In the WA98 setup it is not possible to measure the decay spectrum for all relevant
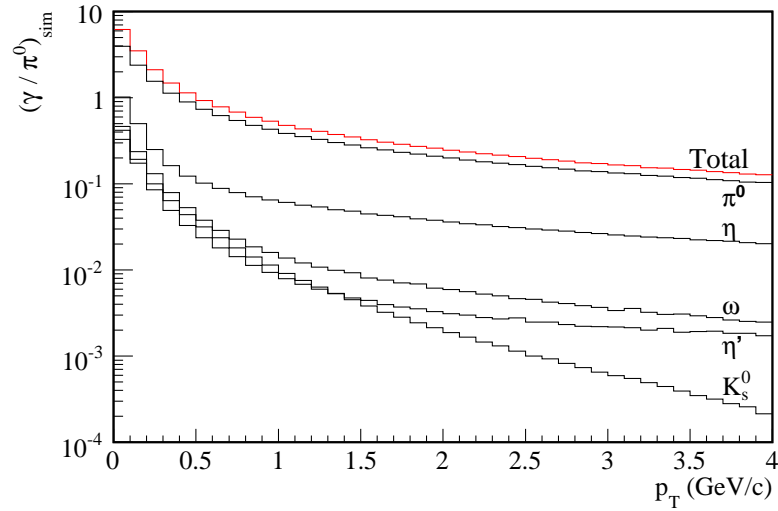
Figure 6.5: Simulated γ/π^0 ratio. The plot shows the total ratio as well as the ratio for the individual photonic decays of mesons included in the simulation.

particles directly. Instead, it is derived from Monte Carlo simulations, in which the measured neutral pion spectrum is used as input to simulate photons from decays. Figure 6.5 shows the simulated ratio as well as the included mesons up to the K_s^0. The p_T distributions of the generated mesons are determined using the assumption of m_T-scaling, i.e. the shape of the spectra as function of the transverse mass m_T is the same for all mesons and only the relative magnitude differs. In this analysis the same scaling factors as in the analysis of the Pb+Pb data presented in [Agg00a] are used. They are shown in Table 6.2. In Figure 6.6 the measured η/π^0-ratio from the results presented in Chapter 5.2 is compared to the scaling factor of 0.55 used in the Pb+Pb analysis. The measurement describes the assumed ratio well and supports the use of the scaling from the Pb+Pb analysis.
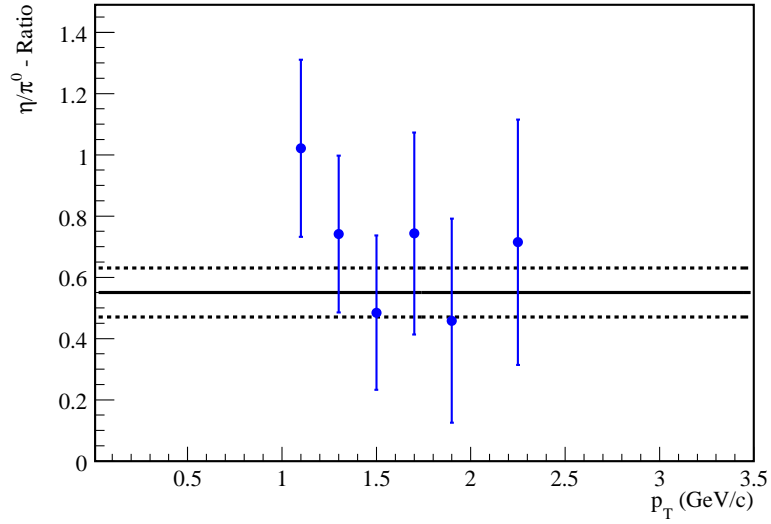
Figure 6.6: η/π^0 ratio from the measurements presented in Chapter 5.2. The black line shows the ratio used in the WA98 Pb+Pb analysis described in [Agg00a], with the assigned uncertainty as dashed lines.

Meson	π^0	η	ω	η'	K_s^0
Ratio	1.0	0.55	1.0	1.0	0.4

Table 6.2: Ratios of the spectra for the mesons which are accounted for in the calculation of the decay photon spectrum with respect to the measured neutral pion spectrum [Agg00a].

Since the simulation of the decay photon spectra relies on the measured neutral pion yield as input, it is assumed that they are identical: $\pi^0_{measured} \equiv \pi^0_{simulated}$. This allows rewriting Equation 6.3 as double ratio:

$$R = \frac{(\gamma_{incl}/\pi^0)_{measured}}{(\gamma_{decay}/\pi^0)_{simulated}}.$$ (6.5)

In this approach, several sources of systematic errors cancel each other at least
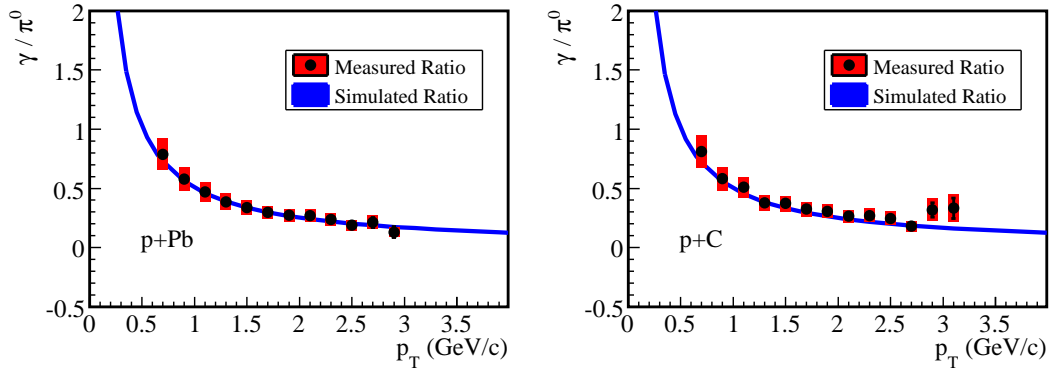
Figure 6.7: Simulated and measured γ/π^0 ratios for p+Pb and p+C. The expectations from decay photons already describe the data well.

partially, e.g. the error on the energy scale and the efficiency, since the neutral pion correction is based on the photon correction, thereby reducing the total systematic uncertainty of the measurement.

The measured γ/π^0-ratio is calculated from the inclusive photon spectrum and a fit to the neutral pion spectrum, since the bin widths used for the two spectra are different.

The resulting double-ratios for p+Pb and p+C, presented in Figure 6.8, do not exhibit any significant excess in the region relevant for thermal photon production.

6.1.7 Systematic Uncertainties of the Direct Photon Spectra

In the following, the different contributions to the systematic uncertainty of the direct photon yield are detailed.

The systematic uncertainty $\Delta(\gamma/\pi^0)_{\text{measured}}$ of the measured inclusive photon yield over the neutral pion yield is computed as the quadratic sum of the systematic
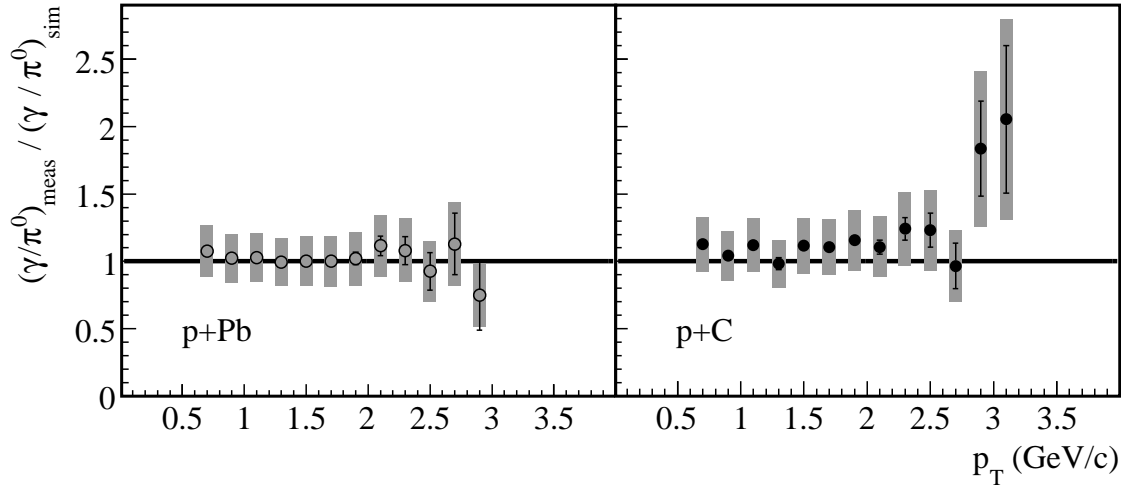
Figure 6.8: Double ratios according to Equation 6.5 for photons from p+Pb and p+C collisions. No significant excess in the p_T range relevant for thermal photon production can be observed.

uncertainties of the inclusive photon spectrum as described above and the neutral pion spectrum as described in Chapter 5.2.6. The errors of the energy scale cancel in this ratio and are therefore removed. The uncertainty of the acceptance correction is accounted for in the simulated (γ/π^0)-ratio. A fit to the measured neutral pion spectrum is used for the simulation as well as for the normalization of the inclusive photon spectrum. The uncertainty of this fit is estimated by fitting the spectrum repeatedly. Before each fit, the points of the spectrum are moved randomly by sampling a Gaussian distribution, the width of which is given by the statistical uncertainty of each point. The residual of each fit is determined and a p_T-dependent fit enveloping all residuals is used as uncertainty of the fit to the neutral pion spectrum. In the calculation of the total error for the γ/π^0-ratio, the uncertainty of the fit replaces the statistical uncertainty of the neutral pion spectrum.

The uncertainty of the simulated γ/π^0-ratio includes, besides the uncertainty in the acceptance determination, the systematical uncertainty of the m_T-scaling and of the η/π^0-ratio used for this scaling.

These uncertainties are propagated when determining the double-ratio R by adding them quadratically. When computing the direct photon yield from Equation 6.4, it is not sufficient to apply a Gaussian error propagation, as the term $(1 - 1/R)$ increases rapidly for small R. Instead, the uncertainty of the direct

	1.25 GeV	2.9 GeV
Efficiency	8.5%	21.9%
- Dispersion Cut	8.4%	8.4%
- Energy Smearing	1.1%	20.2%
- Conversion Correction	0.5%	0.5%
No-Target Correction	2.5%	2.5%
Energy Scale	13.8%	28.7%
Acceptance	2.0%	2.0%
Charged Particles	9.2%	8.0%
(Anti-)Neutrons	5.7%	2.8%
m_T-**scaling**	1%	1%
η/π^0-**ratio**	3%	3%
Fit to π^0-spectrum, p+Pb	2.3%	7.1%
Fit to π^0-spectrum, p+C	2.4%	7.0%

Table 6.3: Systematic uncertainties of the direct photon measurement (WA98, p+A)
.

photon yield $\Delta\gamma_{\text{direct}}$ is determined assuming the maximum errors for the inclusive photon yield and the double ratio R, as described in [Zau07]:

$$\Delta\gamma_{\text{direct},\pm} = \pm \left[\left(1 - \frac{1}{R_\gamma \pm \Delta R_\gamma} \right) \cdot (\gamma_{incl} \pm \Delta\gamma_{incl}) - \gamma_{direct} \right]. \qquad (6.6)$$

The upper and lower limits of the uncertainties obtained from this method are no longer necessarily symmetric.

6.1.8 Upper Limits on the Direct Photon Production

The available data only allow the extraction of upper limits on direct photon production. The results are shown in Figure 6.9. They are discussed and compared to other experimental results in Chapter 7.2. The upper limits are quoted at 1.28σ to ensure consistency with the previously published WA98 results for Pb+Pb collisions, where this interval was used to quote upper limits at a confidence level of 90% [Agg00b]. Feldman and Cousins [Fel98] have shown that the Neyman construction in this earlier analysis may lead to a misrepresantation of the confidence level. The lack of clear criteria for the transition from two-sided to one-sided limits leads to arbitrary decisions on the cross-over, which can cause an under- as well as an over-estimation of the quoted confidence interval. They have introduced a unified
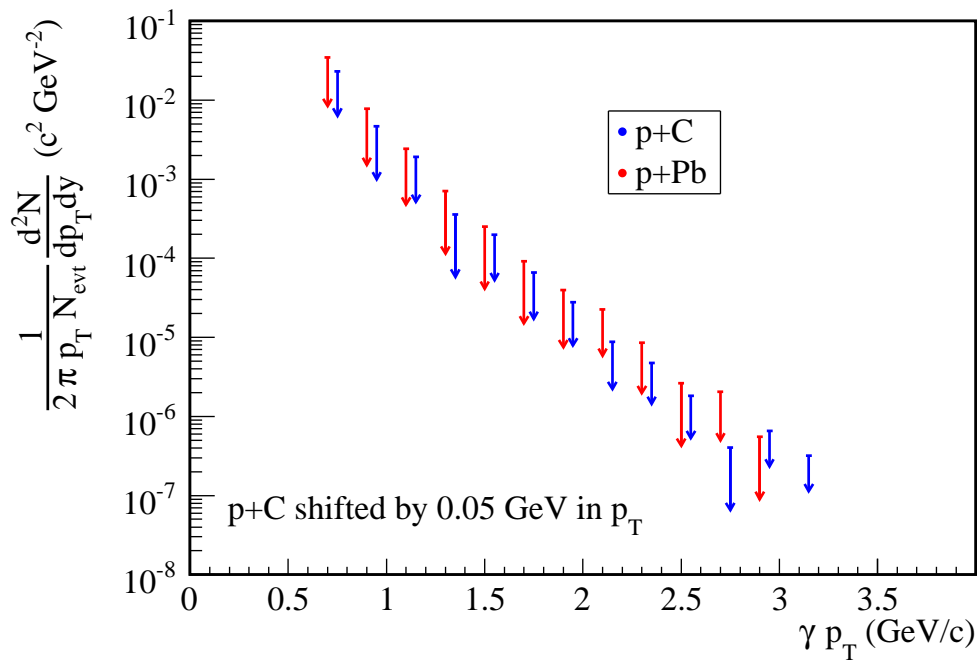
Figure 6.9: Upper limits on the production of direct photons in p+Pb and p+C collisions.

method in which the transition from two-sided to single-sided limits is inherently included. From this method a confidence level of 90% has to be quoted at 1.64σ.

6.2 Search for Direct Photons with PHENIX at SPS Energies

A direct photon yield extracted from the data measured by PHENIX in Cu+Cu collisions at $\sqrt{s_{NN}} = 22.4$ GeV may also deliver information on the early stage of the collision. However, the small amount of available events makes such an analysis difficult. A significant direct photon yield was measured in Cu+Cu collisions at $\sqrt{s_{NN}} = 200$ GeV during the same PHENIX run as the data analyzed in this thesis [Lue07]. To assess the possibility of obtaining a significant direct photon yield from the available data with $\sqrt{s_{NN}} = 22.4$ GeV, the Monte-Carlo simulation used in the analysis of the 200 GeV data is adapted. It is used to obtain the acceptance and efficiency correction. Analogously to the method employed in the WA98 analysis described above, it is also employed for the calculation of the decay photon spectrum. The simulation is based on the same code as the simulation described in Chapter 5.1.6. The energy smearing is adjusted to the values obtained from the neutral pion measurement fits to the measured neutral pion yield and the inclusive photon yield are used as weights for the simulated spectra.

From earlier analyses [Lue07, KB04] it is known that the combined correction for charged particles and (anti-)neutrons, wrongly identified as photons in the electromagnetic calorimeter, can be subtracted well using a p_T-independent correction of 20%.

With these assumptions, the ratios of the inclusive photon to the neutral pion spectra from the measurement and the simulation can be determined as shown in Figure 6.10. Even considering only the statistical errors of the measurement, the results are consistent. The extraction of a significant direct photon yield from the available measured data is, based on this study, not possible due to limitation of the available number of events.
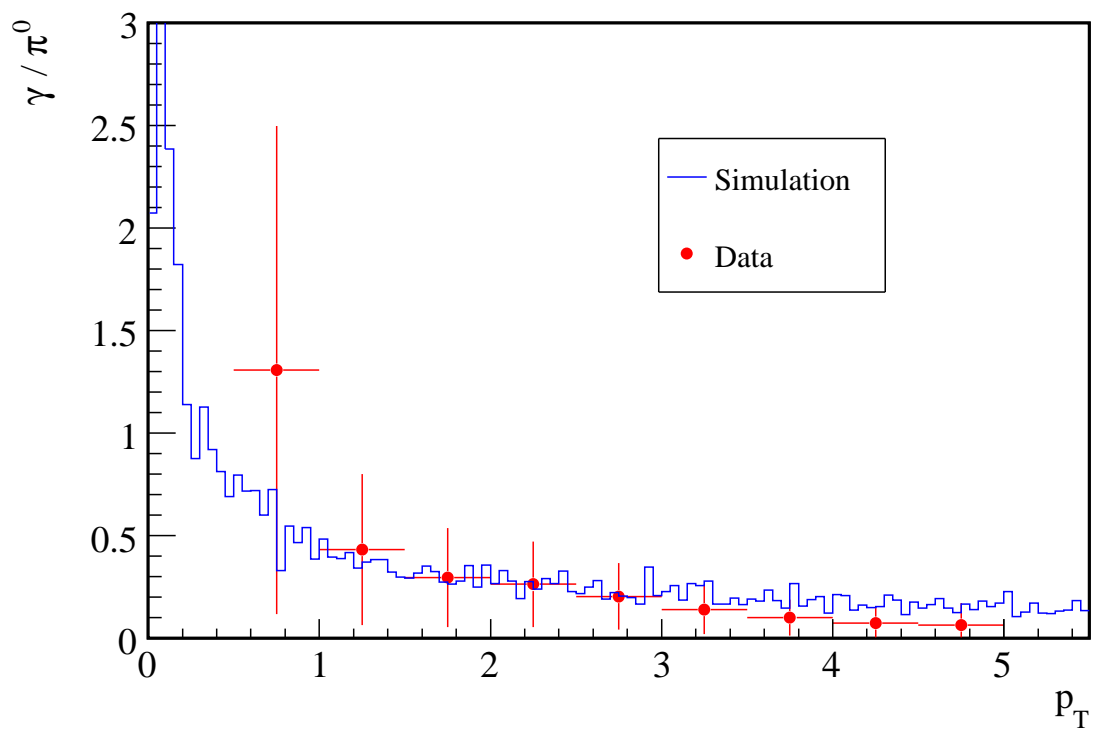
Figure 6.10: Simulated and measured γ/π^0 ratios, only statistical errors are shown.

7. Discussion of the Results

In this chapter, the implications of the measurements presented in this thesis are discussed with a focus on open questions regarding the signatures of a QGP reviewed in Chapter 3.

7.1 Search for Jet Quenching at SPS Energies

With the results presented in Chapter 5 indications for the presence of jet quenching can be sought by determining nuclear modification factors.

7.1.1 WA98 p+A Data as Baseline Measurements

A main motivation for the analysis of the WA98 p+A data is the need for a measured reference for the results on neutral pion production in Pb+Pb collisions to allow the assessment of a possible suppression signal as discussed in Chapter 3.1.

Before employing the results from p+Pb and p+C as a baseline, the consistency with previous results is examined. For the p+C data, it is explored, whether the results scaled by the number N_{coll} of binary parton-parton collisions are in agreement with results obtained from p+p collisions.

It is assumed that in p+C collisions no or only a small Cronin effect is present, while in p+Pb collisions a Cronin enhancement should be more pronounced. Figure 7.1 shows the nuclear modification factor $R_{p+Pb/p+C}$ for p+Pb and p+C collisions, scaled with the number of binary collisions $N_{coll,p+C} = 1.7$ and $N_{coll,p+Pb} = 3.8$. These are determined using a Glauber Monte-Carlo simulation as described in [Mil07]. The relative uncertainty for the N_{coll} values amounts to about 10%. Although the $R_{p+Pb/p+C}$ is compatible with unity within errors, the data shows a slight trend towards an enhancement at higher p_{T}. This supports the assumption of a stronger Cronin enhancement in p+Pb as compared to p+C collisions.

The comparison of the neutral pion yield from the p+C data set scaled by N_{coll} to the average charged pion yield measured in p+p collisions measured by NA49 at $x_F = 0$ [Alt06] shows a reasonable agreement for $p_{\mathrm{T}} \gtrsim 1.2$ GeV and supports the assumption that p+C can be used as a replacement for a p+p measurement.

NA49 has also measured the charged pion production in p+C collisions. The averaged results for $x_F = 0$ are compared to the results from WA98. In the region with overlapping p_{T} coverage good agreement between the two results is found.
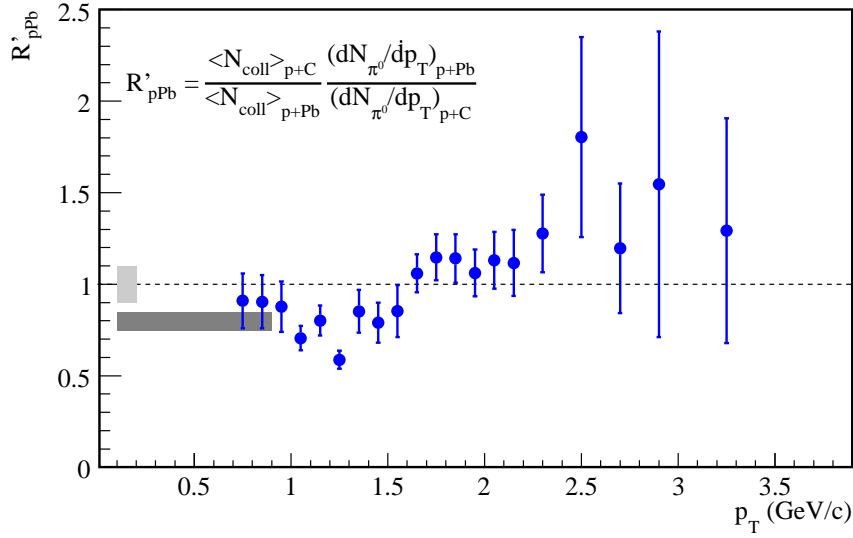
Figure 7.1: Nuclear Modification Factor $R_{p+Pb/p+C}$.

As discussed earlier, it was claimed in [d'E04] that the p+p parameterization by Blattnig et.al. [Bla00] describes the neutral pion production well at SPS energies, while the original parameterization employed by the WA98 collaboration deviates from the available data. The comparison to the p+C data presented here supports this finding (see Figure 7.3): the Blattnig parameterization is in good agreement with the data within errors . The comparison to the p+p parameterization originally employed by the WA98 collaboration shows a significant deviation from the p+C data, scaled by N_{coll}. The fact that the parameterization was derived only from data measured at a higher center-of-mass energy than the Pb+Pb data together with the employed x_T-scaling obviously introduced larger systematic errors than originally assumed.

From these comparisons it can be deduced that the results on the neutral pion production in p+C collisions can be used as a good replacement for proton-proton collisions. The p+Pb data, with the Cronin enhancement being more pronounced compared to the p+C data, may partially remove the enhancement present in the Pb+Pb data when used as reference for the calculation of the nuclear modification factor.

In Figure 7.4, the neutral pion yield from p+C collisions is compared to different NLO-pQCD calculations. These have been scaled with $N_{coll,p+C}$ for this comparison. Pure NLO-pQCD calculations are shown for three scales: $\mu = p_T$, $\mu = 2p_T$, and $\mu = p_T/2$ [Vog07]. The variation of the scale is used to allow the estimation of the
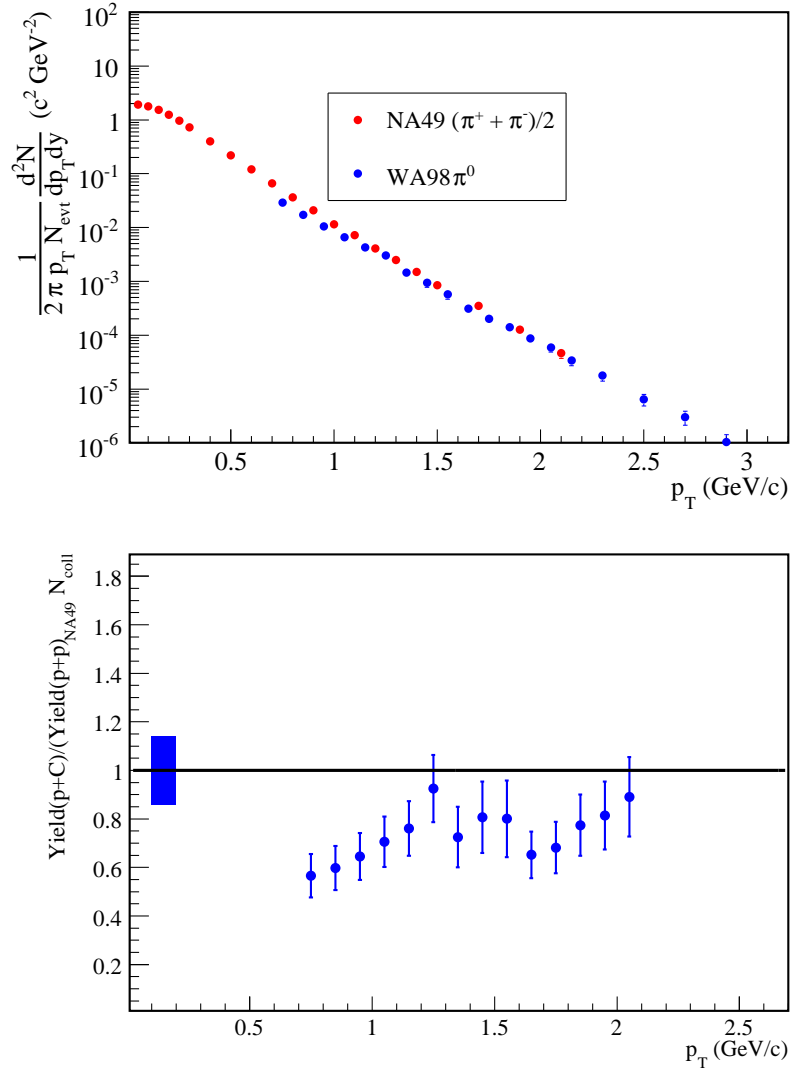
Figure 7.2: The upper panel shows of NA49 results on charged pions in p+p compared to the measurements of the neutral pion yield in p+C collisions from WA98, scaled by N_{coll}. The lower panel shows the ratio of the two results. Due to the different bin widths, a fit to the p+p data is used. The blue box shows the quadratic sum of the uncertainty on the N_{coll} value and the fit to the p+p spectrum.

systematic uncertainty of the calculation. The predicted yield varies between the three calculations for a given p_T by about one order of magnitude. Within these variations, the data is consistent with the calculations. Additionally, NLO-pQCD calculations including threshold resummation corrections according to [dF05] are compared to the data. These additional corrections give an improved description of the measured neutral pion yields in p+p collisions at the higher center-of-mass
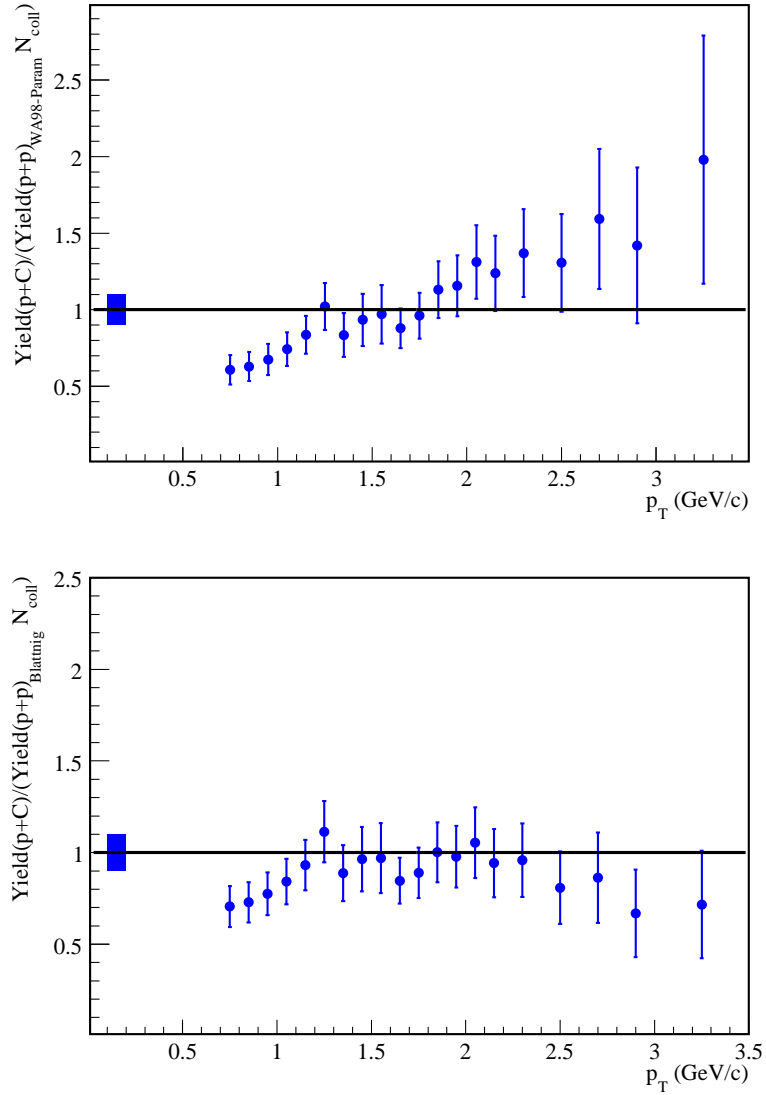
Figure 7.3: The upper panel shows the comparison of the neutral pion production in p+C collisions to the p+p parameterization employed in [Agg02] to quantify the nuclear modification factor of the WA98 Pb+Pb results, the lower panel the comparison of the same data to the p+p parameterization proposed in [Bla00].

energies $\sqrt{s_{NN}} = 22.9$ GeV and $\sqrt{s_{NN}} = 31.5$ GeV. The calculation significantly overpredicts the measured p+C data by nearly one order of magnitude, showing a larger deviation from the data than the pure NLO-pQCD calculation. While results from NLO-pQCD calculations are able to reproduce the measured results, the large systematic uncertainties currently do not allow the use of these calculations for predictions of neutral pion yields for $p_T \approx 3$ GeV/c at SPS energies.
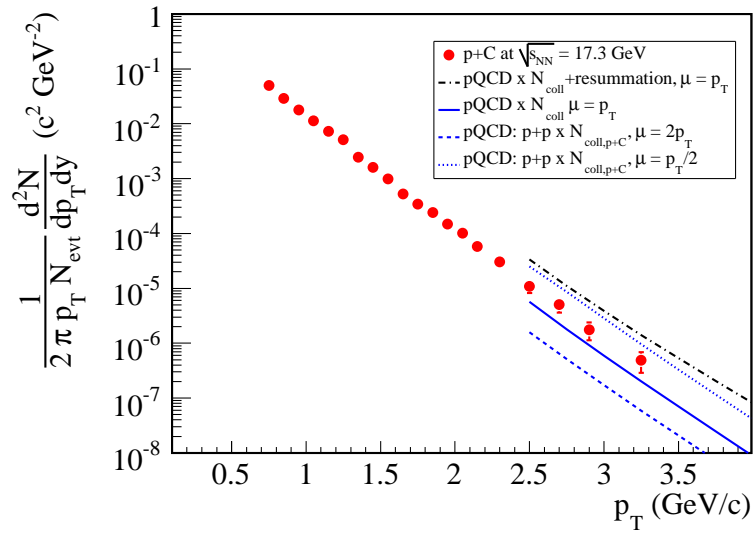
Figure 7.4: Comparison of the neutral pion yield measured in p+C collisions with WA98 to NLO-pQCD calculations, scaled with the number of collisions $N_{coll,p+C}$. The blue lines show pure NLO-pQCD calculations for three different scales $\mu = p_T$, $\mu = 2p_T$ and $\mu = p_T/2$ [Vog07]. The black dash-dotted line shows a NLO-pQCD calculation with threshold resummation according to [dF05] for $\mu = p_T$.

7.1.2   p+p Reference for the 22.4 GeV Data

No measured p+p reference is available at the energy of $\sqrt{s} = 22.4$ GeV, at which the results on the neutral pion production in Cu+Cu collisions presented in Chapter 5.1 have been measured. pQCD calculations do not deliver reliable results at the center-of-mass energy of the Cu+Cu data: the uncertainties for $p_\mathrm{T} \lesssim 5$ GeV are large in this energy regime, as shown above. To calculate the nuclear modification factor, a parameterization by Arleo and d'Enterria [Arl08] described in the following is used.

The parameterization is derived by fitting p+p data sets with 21.7 GeV $\leq \sqrt{s} \leq$ 23.8 GeV. Although pQCD calculations have severe uncertainties at low p_T, the high p_T part of the spectra can be described reasonably well with different sets of parameters.

In order to determine a parameterization, the available data is scaled to the center-of-mass-energy of $\sqrt{s_\mathrm{NN}} = 22.4$ GeV. Unlike in the previous attempts, this is not done by employing x_T scaling. Instead, ratios of NLO-pQCD spectra at $\sqrt{s} = 22.4$ GeV and the center-of-mass energy of the data to be scaled are used to determine a p_T-dependent scaling factor for each data set. This is advantageous, as large scale effects, which are the main source of uncertainty in pQCD calculations, cancel out in this ratio. The scaled experimental cross section is given by

$$\frac{d\sigma_{exp}(\sqrt{s_\mathrm{NN}} = 22.4 \text{ GeV})}{dp_\mathrm{T}} = \left(\frac{d\sigma_{pQCD}/dp_\mathrm{T}(\sqrt{s_\mathrm{NN}} = 22.4 \text{ GeV})}{d\sigma_{pQCD}/dp_\mathrm{T}(\sqrt{s_\mathrm{NN}}_{measured})} \right) \frac{d\sigma_{exp,scaled}(\sqrt{s_\mathrm{NN}}_{measured})}{dp_\mathrm{T}}. \tag{7.1}$$

All scaled data sets are then fitted with the expression

$$f(p_\mathrm{T}) = p_0 \cdot [1 + (p_\mathrm{T}/p_1)]^{p_2} \cdot [1 - (p_\mathrm{T}/p_\mathrm{T}^{max})]^{p_3}. \tag{7.2}$$

This expression has been chosen as it interpolates well between the exponential shape of the spectra at low p_T and the power-law shape at high p_T as well as being zero at the kinematical limit $p_\mathrm{T}^{max} = \sqrt{s}/2 = 11.2$ GeV.

The fit, shown in Figure 7.5, yields the parameters

$$
\begin{aligned}
p_0 &= 176.3 \pm 69.7\text{mb }\text{ GeV}^{-2}\text{c}^3 \\
p_1 &= 2.38 \pm 1.19 \text{ GeV}/c \\
p_2 &= -16.13 \pm 7.21 \\
p_3 &= 6.94 \pm 5.64 \\
\chi^2/\text{ndf} &= 208.2/190.
\end{aligned}
$$

The relative uncertainty increases from 15% for $p_\mathrm{T} \lesssim 2$ GeV to 40% at $p_\mathrm{T} = 5$ GeV.
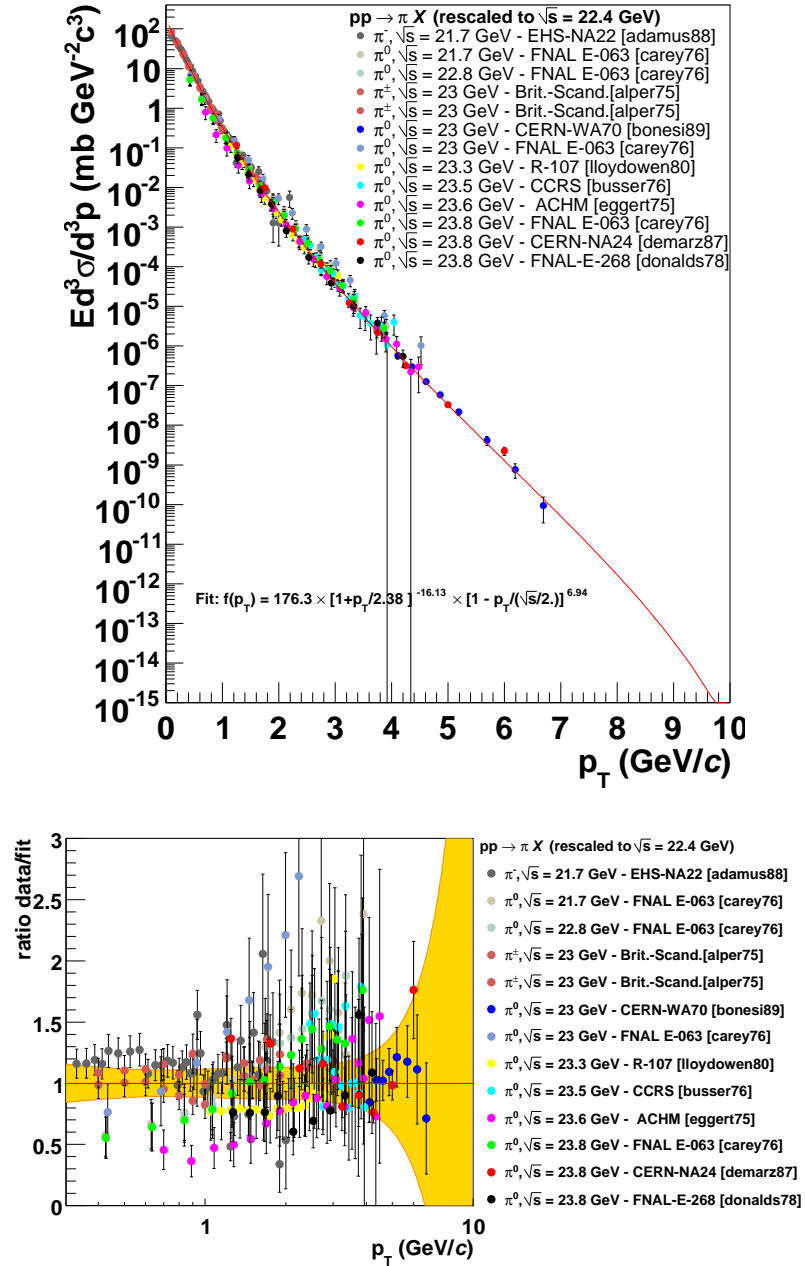
Figure 7.5: Parameterization of available p+p data measured at $\sqrt{s} \approx 22.4$ GeV according to [Arl08]. The upper panel shows the fit together with the data sets used for the determination of the parameters. The data are scaled to a common $\sqrt{s} = 22.4$ GeV. The lower panel shows the ratio of all available data sets, scaled to 22.4 GeV, to the fit. The data sets *carey76* and *eggert75* were exluded from the fit, because they deviate strongly from the majority of available results.

7.1.3 Nuclear Modification Factors

With these references the nuclear modification factors for Pb+Pb collisions at $\sqrt{s_{NN}} = 17.4$ GeV and Cu+Cu collisions at $\sqrt{s_{NN}} = 22.4$ GeV can be estimated.

Centrality Class	Venus 4.21	Glauber Monte-Carlo
$82.8 - 100\%$	9.9 ± 2.5	6.3 ± 2.4
$67.0 - 82.8\%$	30.0 ± 5.0	22.1 ± 7.4
$48.8 - 67.0\%$	78 ± 12	67.1 ± 15.3
$25.3 - 48.8\%$	207 ± 21	202.9 ± 22.9
$13.0 - 25.3\%$	408 ± 41	433.1 ± 43.4
$6.8 - 13\%$	569 ± 57	627 ± 62.7
$0 - 13\%$	651 ± 65	727.8 ± 72.8
$1.0 - 6.8\%$	712 ± 71	803.7 ± 80.4
$0 - 1.0\%$	807 ± 65	912 ± 91.2

Table 7.1: N_{coll} values for different the centrality classes of the WA98 Pb+Pb data, the values from the original publication are compared to results from a Glauber Monte-Carlo calculation.

In the original WA98 publication Venus 4.21 was used to calculate the N_{coll} values for the different centrality classes [Agg02]. For this analysis the same Monte-Carlo simulation as for the p+A data, described in Chapter 7.1.2, is used to recalculate these values [Agg08]. These new results compared to the earlier results are in good agreement within errors, as shown in Table 7.1. For a better consistency with the p+A data, only the Glauber Monte-Carlo results are used for the determination of the nuclear modification factor according to Equation 2.7.1.

The published Pb+Pb data uses a different p_T-bin width than the p+A data. To allow for a calculation of the nuclear modification factor over the entire p_T-range, the Pb+Pb results are rebinned to match the wider bin widths of the p+A data. As a bin shift correction analogous to the correction described in Chapter 5.1.8 had been applied to the data, this correction is removed prior to combining neighboring bins by applying the inverted correction factor to the Pb+Pb data. It is applied again after the rebinning procedure.

The nuclear modification factor for the different centrality classes of the Pb+Pb data, with a p+C as well as a p+Pb reference, is shown in Figure 7.6. For more central events the nuclear modification factor decreases smoothly. It exhibits a clear suppression of up to a factor of 2 for the most central Pb+Pb collisions with both references. As expected from the comparison between the p+Pb and the p+C results, the suppression is more pronounced with the p+Pb data as reference.

Figure 7.7 shows the averaged R'_{AA} of the WA98 data for two different p_T intervals as a function of the centrality, represented by the number of participants N_{part}. While the R'_{AA} with the p+Pb reference is slightly below or consistent with unity for
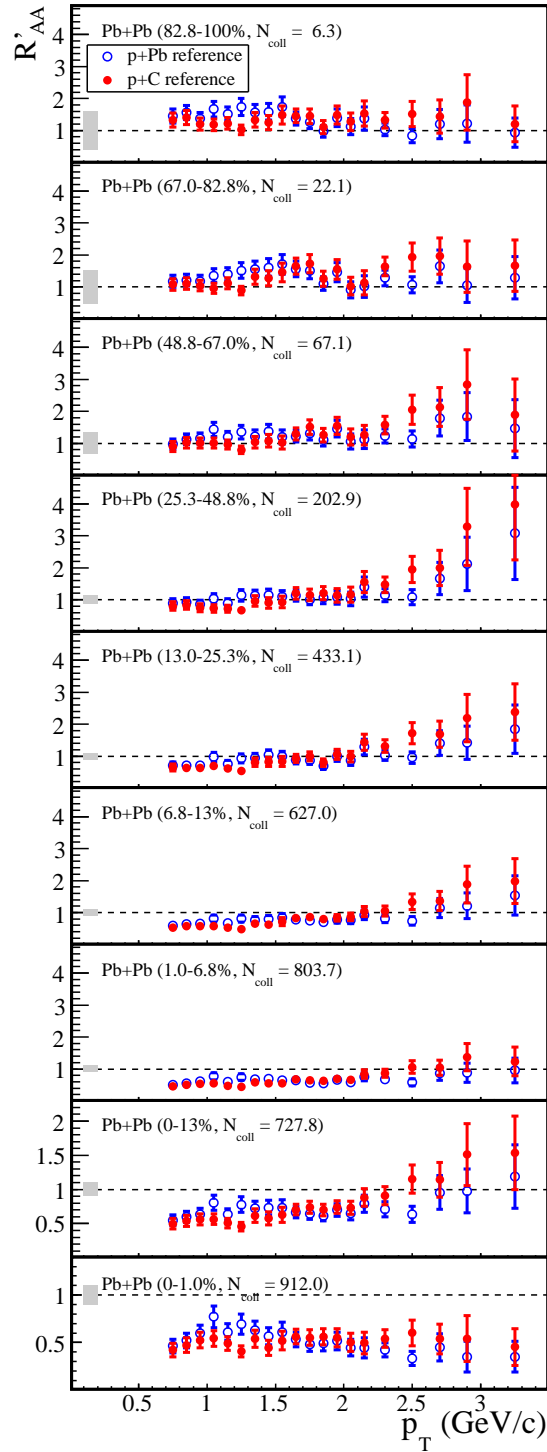
Figure 7.6: Nuclear modification factor for neutral pions from Pb+Pb collisions with a p+C and a p+Pb reference for different centralities.
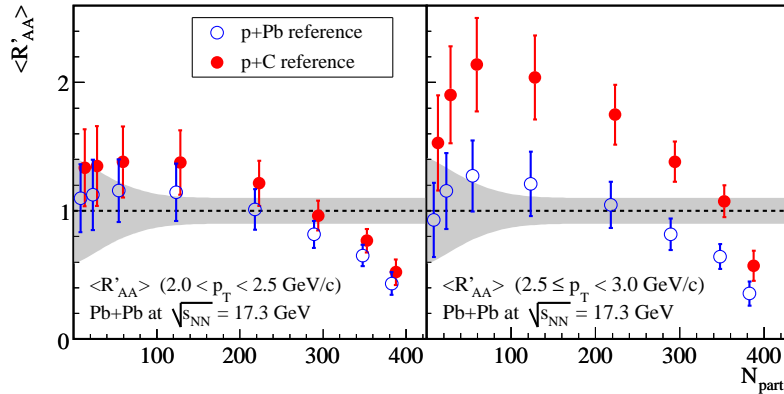
Figure 7.7: Averaged nuclear modification factor for two p_{T} intervals. It can be seen that at higher p_{T}, the suppression is more pronounced with the p+Pb reference, while the p+C data even show a slight enhancement, which is in line with Cronin enhancement.

all intervals, the R'_{AA} with the p+C reference shows an enhancement for non-central events, which is significantly more pronounced in the higher interval 2.5 GeV/$c \leq$ p_{T} < 3.0 GeV/c. This supports the assumption that a suppression of high-p_{T} particles can be hidden by Cronin enhancement at SPS energies. These results have been published in [Agg08].

It has to be noted that it is difficult to quantify energy-loss in a hot and dense medium from the nuclear modification factor alone, because it depends on the energy loss as well as on the steepness of the p_{T} spectra. For the most central events, the nuclear modification factor for the WA98 data presented here is approximately constant at high p_{T} with $R'_{AA} \approx 0.5$. Such values were also reported by PHENIX in heavy ion collisions at $\sqrt{s_{\mathrm{NN}}} = 62.4$ GeV (see Chapter 3.1). Instead, the fractional energy loss S_{loss} can be used to compare the WA98 results to PHENIX results at higher center-of-mass energies. It is given by

$$S_{loss} = \frac{\Delta p_{\mathrm{T}}}{p_{\mathrm{T}}} = 1 - R_{AA}(p_{\mathrm{T}})^{1/(n-2)} \tag{7.3}$$

where n is determined from a power-law fit to the p+p spectrum at the same center-of-mass energy with the assumption $Ed^3N/dp_{\mathrm{T}}^3 \propto p_{\mathrm{T}}^{-n}$ [Adl07a]. Figure 7.8 shows the dependence of S_{loss} on the center-of-mass energy [Rey08]. The S_{loss} calculated from the WA98 R'_{AA} with the p+Pb and p+C reference is significantly below the result obtained from the 62.4 GeV data set. This illustrates that the steeper slope of the spectra at SPS energies compared to RHIC energies has to be taken into account when quantifying energy loss mechanisms.
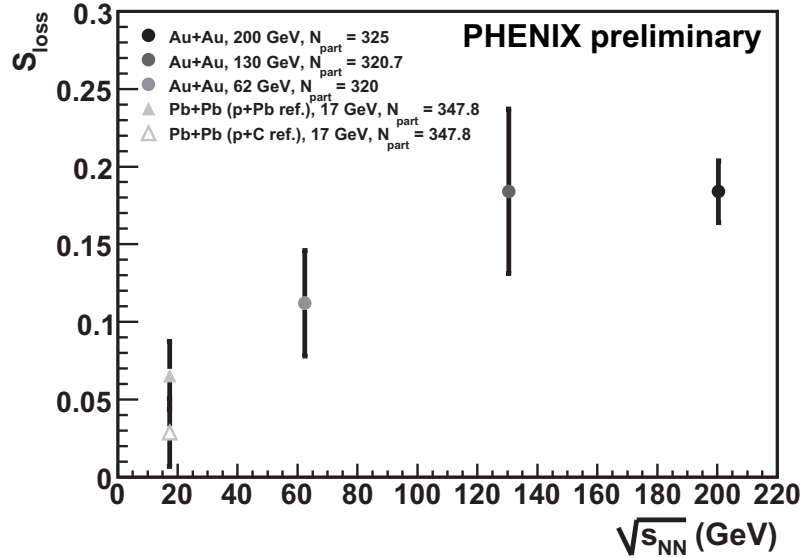
Figure 7.8: S_{loss} determined from neutral pion measurements with WA98 and PHENIX for $\sqrt{s_{\mathrm{NN}}} = 17.4$ GeV $- 200$ GeV [Rey08].

For the PHENIX results from Cu+Cu collisions at $\sqrt{s_{\mathrm{NN}}} = 22.4$ GeV the nuclear modification factor for the neutral pion production is determined with the p+p reference presented in Chapter 7.1.2 and the N_{coll} values shown in Table 5.2. The R_{AA} for all centrality classes of the PHENIX data is shown in Figure 7.9. No suppression is visible in these results. Instead a trend towards an enhancement increasing with p_{T} is observed, with no significant dependence on the centrality.

PHENIX has also published nuclear modification factors for $\sqrt{s_{\mathrm{NN}}} = 200$ GeV and $\sqrt{s_{\mathrm{NN}}} = 62.4$ GeV, together with this result [Ada08c]. In Figure 7.10 the R_{AA} for the $0 - 10\%$ most central events at the three available center-of-mass energies is shown. The data sets measured at $\sqrt{s_{\mathrm{NN}}} = 62.4$ GeV and 200 GeV both exhibit a significant suppression consistent with theoretical expectations for $p_{\mathrm{T}} \gtrsim 2$ GeV/c according to [Vit06b, Vit07]. The suppression of high p_{T} particles in a hot an dense medium is proportional to the gluon density dN_g/dy of the medium. This value can be derived from hadron multiplicities, which allows to control the assumptions of the theoretical calculation.

For $\sqrt{s_{\mathrm{NN}}} = 22.4$ GeV two calculations are provided, one including and one without parton energy loss. Within the given uncertainties it is not possible to discriminate between these two scenarios.
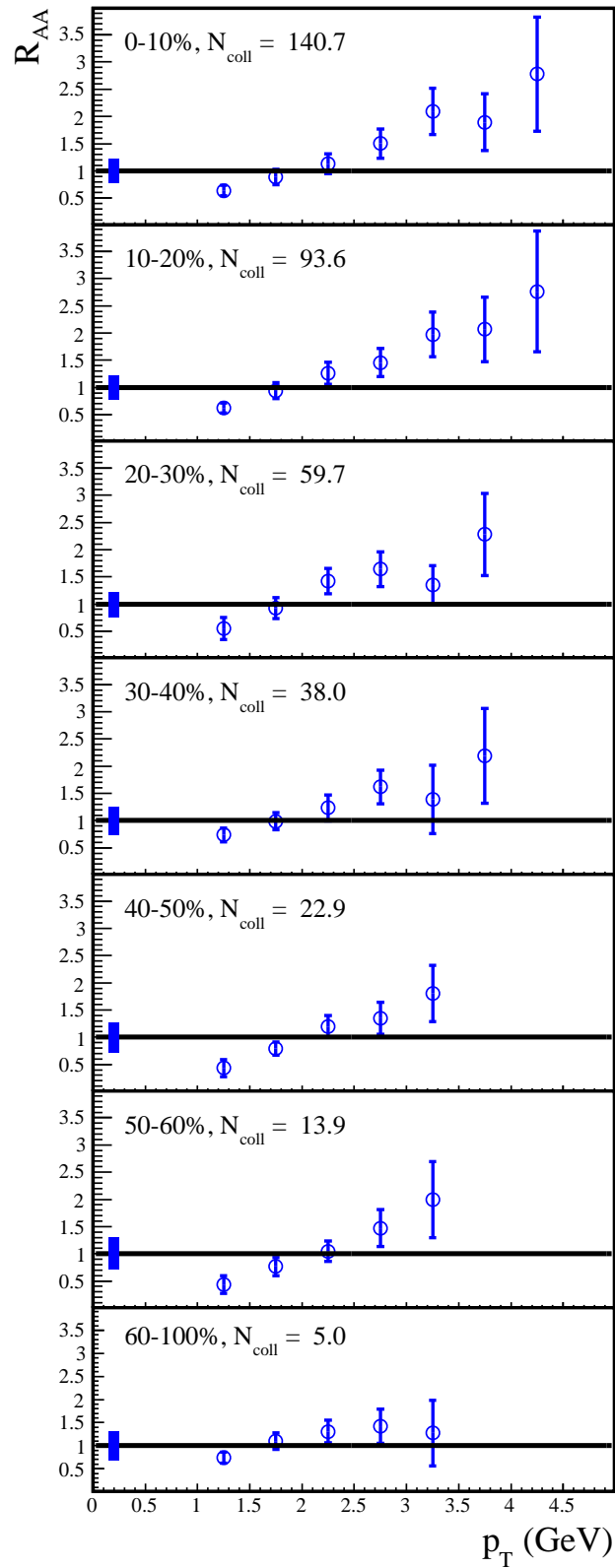
Figure 7.9: R_{AA} for neutral pions measured by PHENIX in Cu+Cu collisions at $\sqrt{s_{\mathrm{NN}}} = 22.4$ GeV.
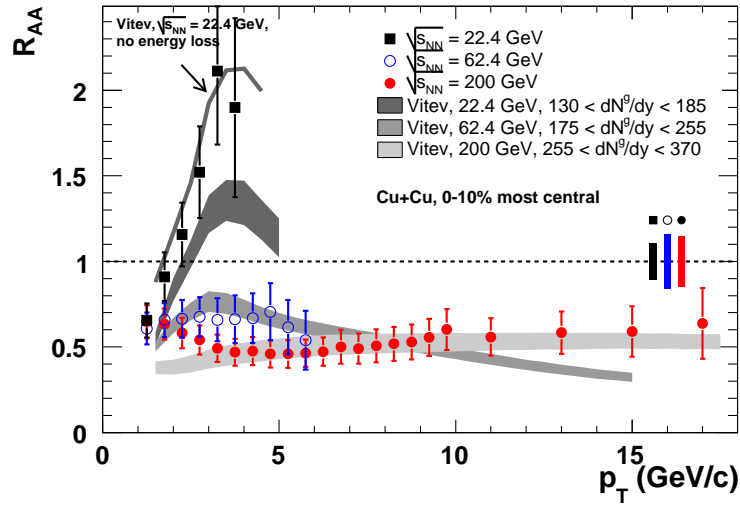
Figure 7.10: Comparison of the nuclear modification factor of the $0 - 10\%$ most central events at the center-of-mass energies 22.4, 62.4 and 200 GeV. The data is compared to energy loss calculations [Vit06b, Vit07]. For the 22.4 GeV data two calculations, one including only Cronin-enhancement, one additionally including energy-loss, are presented [Ada08c].

When displaying the averaged R_{AA} as a function of centrality similar to the WA98 data, as shown in Figure 7.11, this difference is further underlined. While the nuclear modification factor for the Cu+Cu data measured at 62.4 GeV and 200 GeV decreases smoothly for an increasing number of participants and thereby an increasing centrality, the R_{AA} of the 22.4 GeV data exhibits no recognizable dependence on the centrality. This can either be explained by the presence of an only weak Cronin enhancement or by a cancellation of Cronin enhancement and a possibly present high-p_T suppression.

At first glance, these two results may seem contradictory. However, it has to be taken into account that although the PHENIX center-of-mass energy is slightly higher than that at the SPS, copper is a much lighter nucleus than lead, which severely limits the achievable maximum energy density in the collisions. Furthermore, only a p+p parameterization is available. Therefore no experimental quantification of the contribution of Cronin enhancement is possible, as for the WA98 data, where the p+Pb reference at least partially removes this contribution. For the results with the p+C reference, which has been shown to be comparable with a p+p reference, the suppression is only observed for the 6.8% most central events.

When comparing the WA98 measurements to theoretical calculations according to [Vit02] including parton energy loss (see Figure 7.12), they are in good agreement
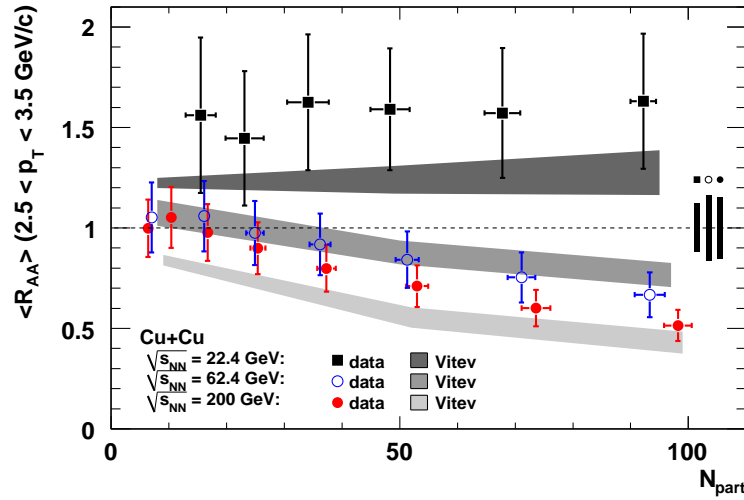
Figure 7.11: Averaged R_{AA} for neutral pions measured by PHENIX as a function of centrality represented by number of participating nucleons N_{part} [Ada08c].

for $p_T \lesssim 2.5$ GeV/c. For higher p_T, the data with p+Pb reference is described better by the theoretical calculations, indicating that the influence of the Cronin enhancement may be underestimated.

RHIC results indicate that at the same center-of-mass energy the suppression only depends on the number of participants. Figure 7.13 shows a comparison of the nuclear modification factor from PHENX data to WA98 results with a p+C reference, the centrality class being chosen so that the number of participants is similar in the data of both experiments. The nuclear modification factors agree well within errors. When comparing the nuclear modification factor for the central events from Pb+Pb collisions at $\sqrt{s_{NN}} = 17.3$ GeV and Au+Au collisions at $\sqrt{s_{NN}} = 62.4$ GeV and 200 GeV with a similar number of participating nucleons N_{coll} (see Figure 7.14), a behaviour qualitatively similar to the results obtained from Cu+Cu is observed. For the approximately $0 - 10\%$ most central events, the onset of a significant suppression seems to be in the interval $\sqrt{s_{NN}} \approx 20 - 60$ GeV.

Figure 7.15 shows the averaged nuclear modification factor as a function of N_{part} for the Pb+Pb and Cu+Cu measurements presented in this thesis for two p_T intervals, 2.0 GeV/$c < p_T < 2.5$ GeV/c and 2.5 GeV/$c \leq p_T < 3.0$ GeV/c. In the lower p_T interval all these data sets agree well within errors, in the higher interval, the nuclear modification factors from the three data sets show larger differences. These are qualitatively consistent with the expected behavior: the Pb+Pb data with p+C
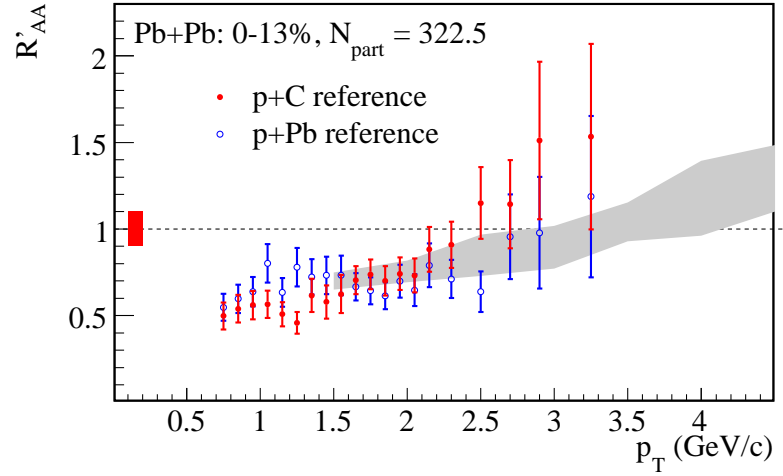
Figure 7.12: Comparison of the nuclear modification factor measured by WA98 in Pb+Pb collisions with two different references from p+Pb and p+C collisions. The shaded band shows theoretical calculations with gluon densitities $dN_g/dy = 400 - 600$, which are consistent with estimates base on hadron multiplicities measured at SPS [Vit02, Blu07].
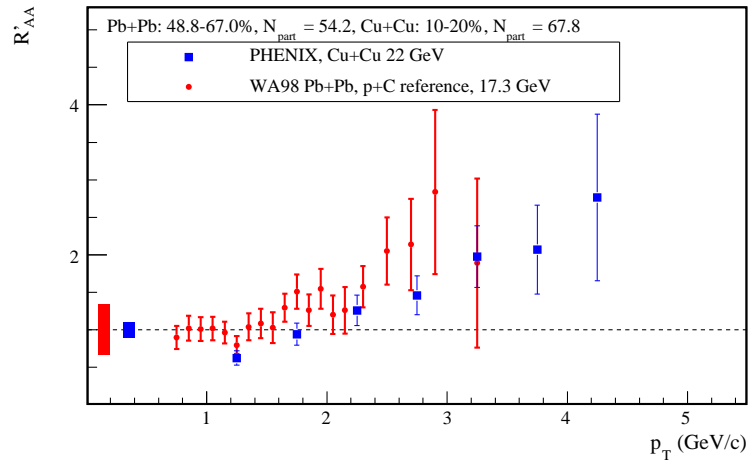
Figure 7.13: Comparison of the nuclear modification factor measured with WA98 and PHENIX at a similar N_{part}.
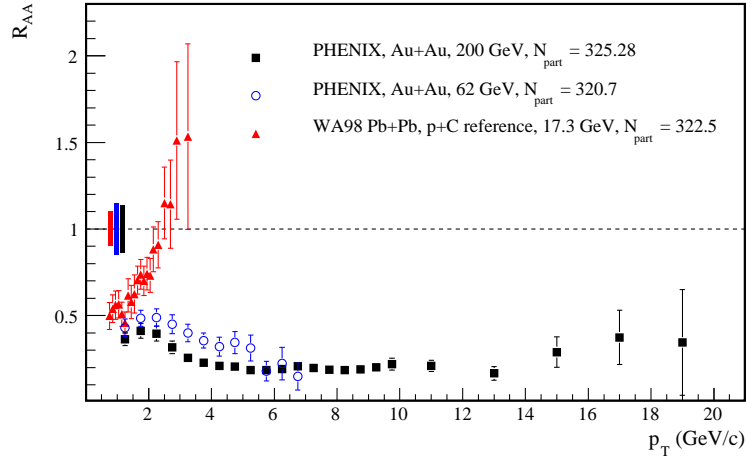
Figure 7.14: Comparison of the nuclear modification factor in Pb+Pb at $\sqrt{s_{\mathrm{NN}}} = 17.3$ GeV measured with the WA98 experiment and in Au+Au collisions at $\sqrt{s_{\mathrm{NN}}} = 62.4$ GeV and 200 GeV for central events with a similar number of participating nucleons [KB08]. While the RHIC results exhibit a significant suppression and are consistent for the highest p_{T} of the 62.4 GeV data, the Pb+Pb data are consistent with unity for the highest p_{T} with a tendency towards an enhancement.
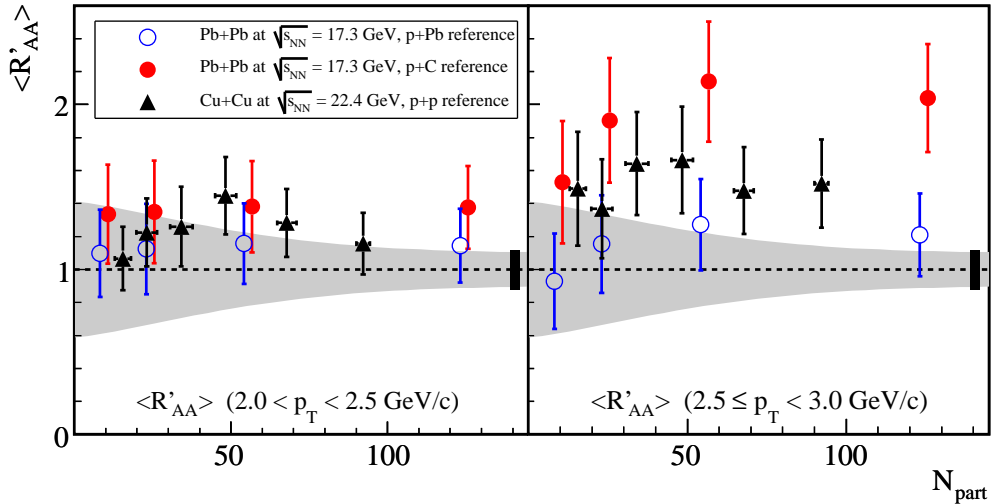
Figure 7.15: Averaged nuclear modification factors of WA98 and PHENIX for two p_{T} intervals as a function of N_{part}. The light grey band indicates the normalization uncertainty for the WA98 data, the black box at $N_{part} = 140$ that of the PHENIX data.

reference exhibit the largest R_{AA}, since Cronin enhancement in Pb+Pb collisions should be more pronounced than in collisions of the lighter Cu+Cu nuclei. The results from Pb+Pb collisions with p+Pb reference show no significant enhancement, this can be explained by the cancellation of Cronin enhancement in the data. It has to be noted that the N_{part} of the most central Cu+Cu collisions is significantly below $N_{part} \approx 300$, the value the onset of suppression can be observed at in the WA98 data.

In summary, the measurements presented in this thesis give strong evidence for the presence of jet-quenching in heavy-ion collisions at SPS energies. A significant influence of Cronin enhancement may obscure the suppression in peripheral events. However, in the most central Pb+Pb collisions at $\sqrt{s_{NN}} = 17.3$ GeV a significant suppression has been established.

7.2 Production of Direct Photons

7.2.1 Comparison to WA98 Pb+Pb Results

The upper limits on the direct photon production in p+A collisions presented in Chapter 6.1.8 may help to set limits on the contribution of prompt direct photons to the direct photon spectrum, measured by WA98 in central Pb+Pb collisions. To compare the two spectra, we assume binary scaling and scale the two p+A data sets by

$$s_{p+A} = N_{coll,Pb+Pb}/N_{coll,p+A}. \tag{7.4}$$

This comparison (see Figure 7.16) shows that while the overall shape of the two spectra agrees well, the scaled upper limits from the p+Pb and p+C data are larger than the data points obtained from central Pb+Pb collisions. Therefore, it is not possible to set upper limits on the prompt direct photon contribution from these new data sets.

Theoretical calculations have used the direct photon production in peripheral Pb+Pb collisions to improve the limits on the prompt direct photon contribution. The comparison shown in Figure 7.17, where the p+A data sets are scaled according to Equation 7.4, shows that also for these data no improvement on the existing limits can be derived from the p+Pb and the p+C data. Bratkovskaya et.al. [Bra08] have compared preliminary results to theoretical calculations of the direct photon yield in p+A collisions. Their calculations show that the upper limits presented in this thesis exceed the expectation by approximately one order of magnitude.
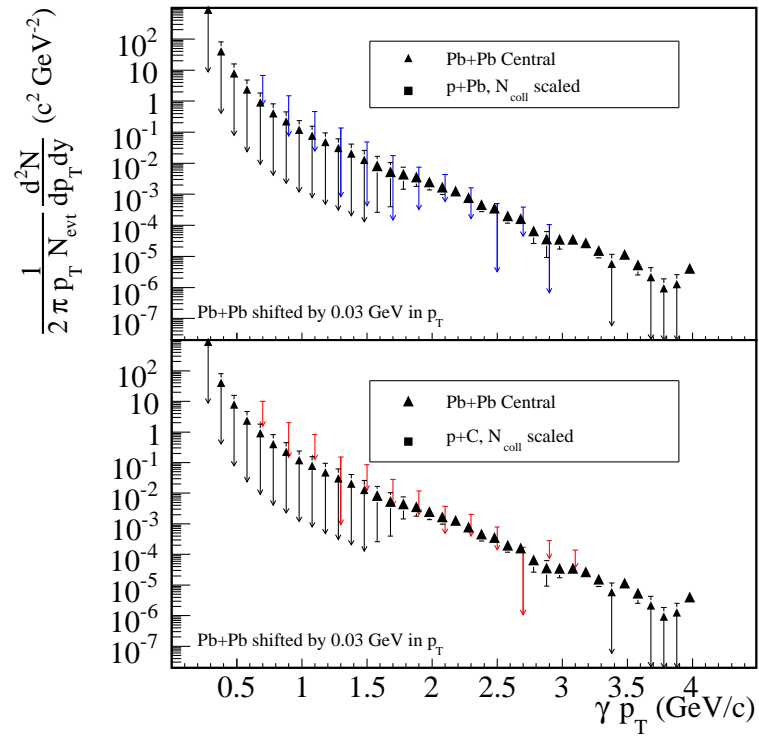
Figure 7.16: Comparison of direct photons in central Pb+Pb collisions to the results from p+C and p+Pb collisions, scaled by N_{coll}.
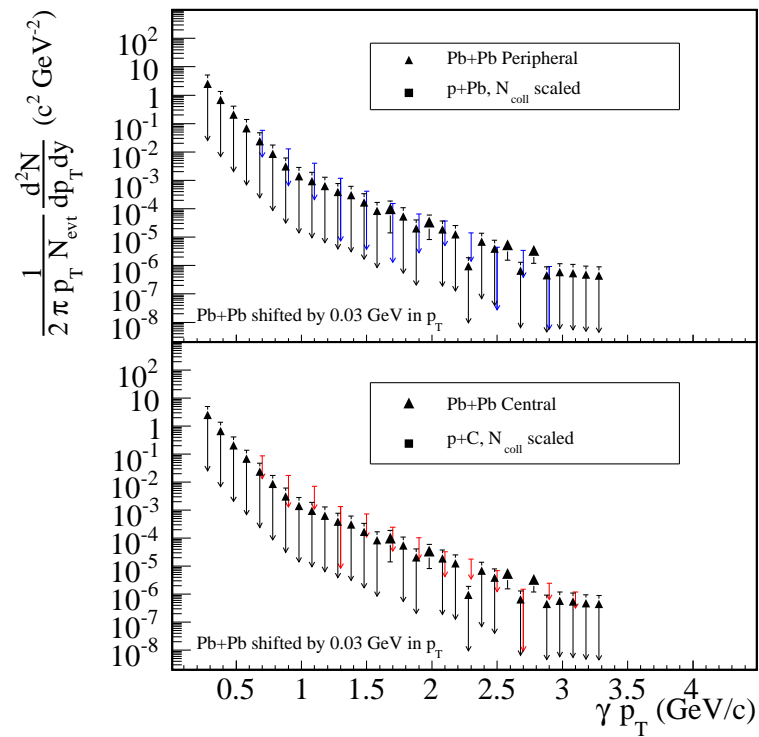
Figure 7.17: Comparison of direct photons in peripheral Pb+Pb collisions to the results from p+C and p+Pb collisions, scaled by N_{coll}.

Although new upper limits are determined for the production of direct photons in p+Pb and p+C collisions at $\sqrt{s_{\mathrm{NN}}} = 17.4$ GeV, the available amount of data still insufficient to constrain a prompt direct photon contribution in Pb+Pb collisions.

Summary

In this thesis, analyses of neutral pion and direct photon production in data sets obtained with two heavy-ion experiments, WA98 located at SPS/CERN and PHENIX at RHIC/BNL, were described. The motivation for these analyses was the search for signatures of the quark-gluon plasma (QGP).

One key discovery at RHIC was the suppression of the neutral pion production in heavy-ion collisions relative to a reference from proton-proton collisions at center-of-mass energies between 62.4 GeV and 200 GeV. The observed suppression pattern can be related to partonic energy loss in a hot and dense medium created in the collisions. Together with other signatures, this discovery provides evidence for the creation of a QGP at the top RHIC energy of $\sqrt{s_{\mathrm{NN}}} = 200$ GeV. For the top SPS center-of-mass energies of about 20 GeV, the experimental situation is unclear. Especially the lack of a reliable, measured p+p or p+A reference with a good coverage of the high p_{T} regime, where a suppression is expected, has been identified as a key problem. Recent reviews of the existing data and the application of parameterizations as a replacement for a measured reference provide evidence that a suppression of particles with high p_{T} in central nucleus-nucleus collisions may be present already at SPS energies.

Thermally produced direct photons were among the first proposed signatures for a QGP. Detailed theoretical studies have shown that the discrimination of models including a QGP and models including other thermal photon sources, e.g. a hot hadron gas, may be difficult, since the predicted thermal photon rates of a hot hadron gas and a QGP do not differ as much as early calculations indicated. However, no experimental evidence for a thermal contribution at SPS energies of $\sqrt{s_{\mathrm{NN}}} \approx 20$ GeV has been found so far. A first evidence for a thermal direct photon signal in heavy-ion collisions has been published by the PHENIX experiment from the analysis of Au+Au and p+p collisions at $\sqrt{s_{\mathrm{NN}}} = 200$ GeV.

Data sets from p+Pb and p+C collisions at $\sqrt{s_{\mathrm{NN}}} = 17.4$ GeV measured with the WA98 experiment were analyzed in this thesis. From both data sets, neutral pion yields covering the p_{T} range $0.7 - 3.5$ GeV/c were extracted on a statistical basis. The yield from the p+C data, scaled by the number of binary nucleon-nucleon

collisions N_{coll}, is consistent with results for the neutral pion production in proton-proton collisions in the overlapping p_T range. The neutral pion production in the p+Pb data set shows a slight enhancement with respect to p+p or p+C data for $p_T \approx 3$ GeV/c. This is consistent with theoretical expectations of a k_T broadening by multiple soft scatterings in the initial state. This so-called Cronin enhancement is expected to be also present in nucleus-nucleus collisions. With these data as reference, the nuclear modification factor R'_{AA} for Pb+Pb collisions measured with WA98 at $\sqrt{s_{NN}} = 17.3$ GeV has been determined. A significant suppression of $R'_{AA} \approx 0.5$ for the $0 - 1\%$ most central Pb+Pb collisions is observed with both data sets as reference. For $p_T \gtrsim 2.5$ GeV/c, the R'_{AA} with the p+Pb reference is significantly below the result with the p+C reference. This is consistent with an at least partial cancellation of the Cronin enhancement between the Pb+Pb and the p+Pb data.

Upper limits on the production of direct photons have been determined from both data sets. When compared to the results obtained from Pb+Pb collisions measured by WA98, it is found that no new constraints on a possible prompt direct photon contribution can be derived from these new results. With the available data a possible thermal contribution to the available direct photon results cannot be identified.

At PHENIX, Cu+Cu collisions at $\sqrt{s_{NN}} = 22.4$ GeV were measured. Neutral pion yields for eight different centrality selections with a maximum p_T of up to 5 GeV/c could be extracted. The nuclear modification factor R_{AA} was quantified with a parameterization of available p+p data, scaled to $\sqrt{s_{NN}} = 22.4$ GeV on the basis of NLO-pQCD calculations. The measured nuclear modification factor exhibits a small enhancement consistent with expectations for the Cronin effect. No dependence of the nuclear modification factor on the centrality is observed, while at center-of-mass energies of 62.4 GeV and 200 GeV results from Cu+Cu collisions exhibit a suppression consistent with partonic energy loss models. With the available 22.4 GeV data, it is not possible to discriminate between scenarios including only a moderate Cronin enhancement and scenarios also including partonic energy loss mechanisms. However, when compared to the WA98 results at a similar number of participants N_{part}, the results from both experiments are found to be in good agreement. The extraction of a direct photon signal has also been studied for the Cu+Cu data, but, due to the large statistical uncertainties, no significant signal for the direct photon production could be obtained.

In summary, the results presented in this thesis, foremost the observation of a suppression of the neutral pion production at high-p_T in central Pb+Pb collisions

with two new measured references, strongly support the assumption that a QGP may already be created at SPS energies.

Zusammenfassung

In dieser Arbeit wurden Analysen der Produktion neutraler Pionen und direkter Photonen vorgestellt. Die Daten wurden mit zwei Schwerionen-Experimenten, dem WA98 Experiment am SPS/CERN und dem PHENIX Experiment am RHIC/BNL gemessen. Die Hauptmotivation für die Analysen ist die Suche nach Hinweisen auf die Erzeugung eines Quark-Gluon Plasmas (QGP).

Eine der Hauptentdeckungen am RHIC war die Unterdrückung der Produktion neutraler Pionen in Schwerionenstössen im Vergleich zu einer Referenz aus Proton-Proton Kollisionen bei Schwerpunktsenergien von 62.4 GeV bis 200 GeV. Bei den höchsten SPS Schwerpunktsenergien von etwa 20 GeV ist die experimentelle Situation unklar. Insbesondere das Fehlen einer gemessenen Referenz aus p+p oder p+A Daten mit einer guten Abdeckung im Bereich hoher Transversalimpulse, wo eine Unterdrückung erwartet wird, hat sich als problematisch herausgestellt. Neubewertungen der existierenden Daten und die Verwendung von Parameterisierungen als Ersatz für eine gemessene Referenz weisen darauf hin, dass eine Unterdrückung von Teilchen mit hohem Transversalimpuls in zentralen Kern-Kern Kollisionen bei SPS Energien vorhanden sein könnte.

Thermisch produzierte direkte Photonen gehören zu den ersten Signaturen, die für die Entdeckung eines QGPs vorgeschlagen wurden. Detaillierte theoretische Rechnungen haben ergeben, dass die Unterscheidung von Modellen die ein QGP beinhalten, von denen die andere thermische Photonenquellen, z.B. ein *heißes Hadronengas*, beinhalten, experimentell schwierig ist, da sich die erwarteten Produktionsraten für thermische Photonen nicht so stark unterscheiden wie ursprünglich angenommen. Bis heute wurde kein Hinweis auf thermische Photonen bei SPS Energien gefunden. Allerdings hat das PHENIX Experiment kürzlich eine erste Evidenz für ein Signal von thermischen direkten Photonen in der Analyse von Au+Au und p+p Kollisionen bei $\sqrt{s_{\mathrm{NN}}} = 200$ GeV publiziert.

In dieser Arbeit wurde die Analyse von Datensätzen aus p+Pb und p+C Kollisionen bei $\sqrt{s_{\mathrm{NN}}} = 17.4$ GeV beschrieben. Für beide Datensätze konnten Impulsverteilungen neutraler Pionen im p_{T} Bereich von 0.7 bis 3.5 GeV bestimmt werden. Die Ergebnisse aus den p+C Daten, skaliert mit der Anzahl der binären Nukleon-

Nukleon Stöße, stimmen in dem p_T Bereich für den Daten anderer Experimente
verfügbar sind mit Ergebnissen aus Proton-Proton Kollisionen überein. Die Impuls-
verteilung neutraler Pionen aus dem p+Pb Datensatz zeigt eine leichte Überhöhung
im Vergleich zu p+p und p+C Daten bei Transversalimpulsen von etwa 3 GeV. Dies
entspricht theoretischen Erwartungen für das sogenannte k_T-*broadening* durch mehr-
fache weiche Streuprozesse. Dieser auch als *Cronin-Verstärkung* bezeichnete Effekt
ist auch in Kern-Kern Kollisionen relevant. Mit diesen Daten als Referenz ließ sich
der nukleare Modifikationsfaktor R'_{AA} für bereits zuvor veröffentlichte Pb+Pb Daten,
die bei einer Schwerpunktsenergie von 17.3 GeV gemessen wurden, berechnen. In den
1% zentralsten Kollisionen lässt sich eine signifikate Unterdrückung von $R'_{AA} \approx 0.5$
mit beiden Referenz-Datensätze beobachten. Der nukleare Modifikationsfaktor mit
einer p+Pb Referenz ist für $p_\mathrm{T} \geq 2.5$ GeV/c kleiner als der mit p+C Referenz.
Dies läßt sich durch eine zumindest teilweise Aufhebung der Cronin-Verstärkung im
Vergleich von p+Pb und Pb+Pb Daten verstehen.

Für die Produktion direkter Photonen wurden obere Grenzen aus beiden Daten-
sätzen bestimmt. Der Vergleich dieser neuen Ergebnisse mit der Messung direkter
Photonen in Pb+Pb Kollisionen zeigt, dass sich die Schranken für die Produktion
prompter Photonen nicht durch die neuen Daten verbessern lassen. Die verfügba-
ren Daten lassen daher keine Rückschlüsse auf einen möglichen Beitrag thermischer
Photonen zu.

Am PHENIX Experiment wurden Messungen von Cu+Cu Kollisionen bei
$\sqrt{s_\mathrm{NN}} = 22.4$ GeV durchgeführt. Aus diesen konnten Transversalimpulsverteilun-
gen neutraler Pionen für acht verschiedene Zentralitätsklassen im Bereich bis 5 GeV
bestimmt werden. Der nukleare Modifikationsfaktor R_{AA} wurde mit Hilfe einer Pa-
rameterisierung von p+p Daten, die mit Hilfe von NLO-pQCD Rechnungen auf
$\sqrt{s_\mathrm{NN}} = 22.4$ GeV skaliert wurden, berechnet. Der nukleare Modifikationsfaktor
weist eine leichte Erhöhung auf, die mit Erwartungen für den Cronin Effekt über-
einstimmt. Es ist keine Abhängigkeit des R_{AA} von der Zentralität der Ereignisse zu
beobachten, während bei höheren Schwerpunktsenergien von 62.4 GeV und 200 GeV
auch in Cu+Cu Kollisionen eine Unterdrückung in Übereinstimmung mit Erwar-
tungen für Energieverlust auf Partonebene zu beobachten ist. Mit den vorhandenen
Daten bei 22.4 GeV ist es nicht möglich zwischen einem theoretischen Szenario das
lediglich eine moderat ausgeprägte Cronin-Verstärkung beinhaltet und einem, das
zusätzlich auch Energieverlust auf Partonebene beinhaltet, zu unterscheiden. Wenn
man die Daten allerdings mit den WA98 Ergebnissen bei einem ähnlichen Wert
für N_{part} vergleicht sind die Ergebnisse der beiden Experimente in guter Überein-
stimmung. Eine mögliche Bestimmung von Transversalimpulsverteilungen direkter
Photonen aus den PHENIX Cu+Cu Daten wurde untersucht, allerdings konnten

aufgrund der großen statistischen Unsicherheiten keine signifikanten Messpunkte bestimmt werden.

Zusammengefasst unterstützen die in dieser Arbeit präsentierten Ergebnisse, insbesondere die Messung einer Unterdrückung der Produktion neutraler Pionen in zentralen Pb+Pb Kollisionen bei hohem p_T im Vergleich zu den zwei neuen Referenzmessungen, die Annahme, dass möglicherweise bereits im Bereich von SPS Energien ein QGP erzeugt wird.

A. Kinematic Variables

As relativistic effects cannot be neglected in the field of high-energy physics, the kinematical variables used in the analysis of the data are generally chosen so that simple mathematical transformations apply when changing the frame of reference. Detailed introductions are given in [Won94, Ams08], an overview is given in the following. In relativistic kinematics, the momentum of a particle can be expressed by the four-vector

$$p^\mu = (E, \overrightarrow{p}) = (E, p_x, p_y, p_z). \tag{A.1}$$

Commonly, *natural units* are used, where $\hbar = c = 1$. The rest mass m_0 of a free particle can be identified with the invariant mass m_{inv}, given by

$$m_{inv}^2 = P^\mu P_\mu = E^2 - \overrightarrow{p} \cdot \overrightarrow{p}, \tag{A.2}$$

yielding

$$E^2 = m_0^2 + p^2. \tag{A.3}$$

In accelerator experiments, the direction of the beam is often used to define the z-axis of the coordinate system, with ϑ being the angle between $\overrightarrow{p}$ and this axis. The momentum can then be separated into

$$p_{\mathrm{L}} = |\overrightarrow{p}| \cdot \cos\vartheta = p_z, \tag{A.4}$$

$$p_{\mathrm{T}} = |\overrightarrow{p}| \cdot \sin\vartheta = \sqrt{p_x^2 + p_y^2}. \tag{A.5}$$

From the transverse momentum p_{T}, it is possible to identify the transverse mass

$$m_{\mathrm{T}} = \sqrt{m_0^2 + p_{\mathrm{T}}^2}. \tag{A.6}$$

The longitudinal velocity of a particle can be quantified with the rapidity y

$$y = \frac{1}{2} \ln \frac{E + p_{\mathrm{L}}}{E - p_{\mathrm{L}}}. \tag{A.7}$$

When changing the frame of reference, where the relative velocity between two systems is given by β, the rapidity is given by the simple additive expression

$$y' = y + \mathrm{atanh}\beta \tag{A.8}$$

For energies $E \gg m_0$, the rapidity can be approximated by the pseudorapidity η, which does not depend on the rest mass of the particle and can be solely related to the angle with respect to the beam axis:

$$\eta = \frac{1}{2} \ln \left(\frac{p + p_{\mathrm{L}}}{p - p_{\mathrm{L}}} \right) = -\ln \left[\tan \left(\frac{\vartheta}{2} \right) \right]. \tag{A.9}$$

The energy of two colliding particles is given by the Mandelstam variable s with

$$s = (P_1 + P_2)^2. \tag{A.10}$$

The center-of-mass energy energy E_{cm} can then be defined as

$$E_{cm} = \sqrt{s} = \sqrt{(E_1 + E_2)^2 - (\vec{p_1} - \vec{p_2})^2}. \tag{A.11}$$

In the rest frame of a particle with the mass m_2, which is the case for fixed-target experiments, this expression becomes

$$E_{cm} = \sqrt{m_1^2 + m_2^2 + 2E_1 m_2}. \tag{A.12}$$

B. Lists of the Analyzed Runs

B.1 PHENIX

163604	163605	163607	163609	163610	163612
163614	163619	163621	163623	163625	163627
163629	163633	163645	163648	163650	163652
163661	163664	163668	163672	163673	163675
163677	163679	163681			

Table B.1: Analyzed runs measured with PHENIX in Cu+Cu collisions at 22.4 GeV.

B.2   Valid Runs for the WA98 Analyses

7005	7006	7007	7008	7009	7010	7011	7012	7013	7014	7015	7016
7017	7018	7026	7027	7028	7029	7030	7031	7032	7033	7034	7035
7036	7037	7038	7039	7040	7041	7042	7043	7044	7045	7046	7047
7048	7049	7050	7051	7052	7053	7054	7056	7058	7059	7060	7061
7062	7063	7064	7065	7066	7067	7068	7069	7070	7071	7072	7073
7074	7075	7076	7077	7078	7079	7080	7081	7082	7083	7084	7086
7087	7088	7089	7090	7091	7092	7093	7094	7095	7096	7097	7105
7107	7108	7109	7110	7111	7112	7113	7114	7115	7116	7117	7121
7122	7123	7124	7125	7126	7128	7129	7130	7131	7132	7133	7134
7135	7136	7137	7138	7139	7141	7142	7143	7149	7150	7151	7152
7153	7154	7155	7156	7157	7158	7159	7160	7161	7162	7163	7164
7166	7167	7169	7170	7171	7172	7173	7174	7175	7176	7177	7178
7179	7180	7181	7182	7183	7184	7185	7193	7195	7196	7197	7199
7200	7201	7202	7203	7204	7205	7206	7207	7208	7209	7210	7211
7212	7213	7215	7216	7217	7218	7219	7220	7221	7222	7223	7233
7234	7235	7236	7237	7238	7239	7240	7241	7242	7243	7244	7245
7246	7247	7248	7249	7250	7251	7252	7253	7254	7255	7257	7258
7259	7261	7262	7263	7264	7265	7266	7269	7270	7271	7272	7273
7274	7275	7276	7277	7278	7279	7280	7281	7282	7283	7284	7285
7286	7288	7290	7291	7292	7307	7308	7309	7310	7311	7312	7313
7314	7315	7316	7317	7318	7319	7320	7321	7322	7323	7324	7325
7326	7327	7328	7329	7330	7331	7332	7333	7334	7335	7338	7339
7340	7343	7344	7368	7383	7385	7386	7387	7388	7389	7390	7391
7392	7394	7395	7396	7397	7398	7408	7409	7410	7411	7412	7413
7414	7415	7416	7417	7418	7419	7420	7421	7422	7423	7424	7425
7427	7428	7429	7430	7431	7432	7433	7437	7438	7439	7440	7441
7442	7443	7444	7445	7446	7448	7449	7450	7451	7453	7454	7455
7456	7457	7458	7459	7460	7461	7462	7463	7464	7465	7466	7468
7469	7470	7476	7477	7478	7479	7480	7481	7482	7483	7484	7485
7486	7487	7488	7489	7490	7491	7492	7493	7495	7496	7497	7498

7500	7501	7502	7504	7505	7506	7507	7508	7509	7510	7511	7512
7513	7514	7515	7516	7517	7518	7519	7520	7521	7522	7523	7524
7525	7526	7527	7528	7529	7531	7533	7534	7535	7536	7537	7538
7539	7540	7541	7542	7543	7544	7545	7546	7547	7548	7560	7561
7562	7563	7564	7565	7566	7567	7568	7569	7570	7571	7572	7573
7575	7576	7579	7580	7581	7586	7587	7588	7589	7591	7593	7594
7595	7596	7597	7598	7599	7600	7601	7602	7603	7604	7605	7606
7607	7608	7609	7610	7611	7612	7613	7615	7616	7617	7619	7620
7621	7622	7634	7635	7636	7637	7638	7639	7640	7641	7642	7643
7644	7645	7646	7647	7648	7649	7650	7651	7652	7653	7654	7655
7656	7658	7659	7660	7661	7662	7663	7664	7665	7668	7669	7670
7671	7672	7673	7674	7675	7676	7677	7678	7679	7680	7681	7682
7683	7684	7685	7686	7687	7688	7689	7690	7691	7692	7693	7694
7696	7697	7698	7699	7700	7701	7702	7703	7704	7748	7749	7750
7751	7752	7753	7755	7756	7757	7758	7759	7760	7761	7773	7774
7775	7776	7777	7778	7779	7780	7781	7782	7783	7784	7785	7786
7787	7788	7789	7790	7791	7792	7794	7795	7796	7796		

Table B.2: Analyzed runs measured with WA98 in p+Pb collisions at 17.4 GeV.

6372	6373	6374	6375	6381	6382	6383	6384	6385	6386	6387	6388
6389	6390	6391	6397	6398	6399	6400	6401	6402	6403	6404	6405
6406	6407	6408	6409	6410	6411	6412	6414	6415	6416	6417	6418
6419	6420	6421	6423	6424	6425	6426	6427	6428	6429	6430	6431
6432	6433	6434	6441	6442	6443	6444	6446	6447	6465	6466	6467
6468	6469	6470	6471	6472	6473	6474	6501	6502	6503	6504	6505
6506	6508	6509	6510	6511	6514	6515	6518	6523	6524	6525	6542
6543	6544	6545	6546	6547	6548	6590	6591	6592	6593	6594	6595
6596	6597	6598	6599	6600	6604	6605	6606	6607	6608	6609	6610
6611	6614	6615	6616	6617	6618	6619	6664	6665	6666	6667	6668
6670	6671	6672	6673	6674	6675	6676	6677	6678	6683	6684	6685

6686	6692	6694	6697	6698	6699	6700	6702	6703	6711	6712	6713
6714	6715	6716	6717	6718	6719	6720	6721	6728	6729	6730	6731
6732	6733	6735	6736	6737	6738	6739	6740	6741	6742	6748	6749
6750	6751	6752	6753	6754	6755	6756	6757	6758	6759	6760	6761
6762	6763	6764	6765	6766	6767	6768	6769	6770	6771	6772	6773
6774	6775	6776	6782	6783	6784	6786	6787	6788	6789	6790	6791
6792	6793	6794	6795	6796	6797	6798	6799	6800	6801	6802	6803
6804	6805	6806	6807	6808	6809	6810	6811	6812	6813	6814	6815
6816	6817	6818	6819	6821	6822	6823	6824	6825	6826	6828	6829
6831	6832	6835	6836	6838	6840	6841	6842	6843	6844	6845	6846
6857	6858	6859	6860	6861	6869	6870	6871	6872	6873	6875	6876
6877	6878	6879	6880	6881	6882	6883	6884	6885	6886	6887	6888
6889	6890	6916	6917	6918	6919	6920	6921	6922	6924	6925	6926
6928	6929	6930	6931	6932	6933	6934	6957	6958	6959	6961	6962
6963	6964	6965	6966	6967	6968	7859	7860	7861	7861		

Table B.3: Analyzed runs measured with WA98 in p+C collisions at 17.4 GeV.

6995	6996	6997	6998	7098	7099	7100	7101	7102	7103	7104	7144
7145	7146	7147	7148	7186	7187	7188	7189	7190	7191	7192	7225
7226	7227	7228	7229	7231	7232	7293	7294	7295	7296	7297	7298
7299	7300	7301	7302	7303	7304	7305	7306	7399	7400	7401	7402
7403	7405	7406	7471	7472	7473	7474	7475	7549	7550	7551	7552
7553	7554	7555	7557	7558	7559	7623	7624	7626	7627	7628	7629
7630	7631	7632	7633	7710	7711	7712	7713	7714	7715	7716	7717
7762	7763	7764	7765	7766	7767	7768	7769	7770	7771	7772	7772

Table B.4: Analyzed runs measured without target in place during the WA98 p+Pb beamtime collisions at 17.4 GeV.

6392	6393	6394	6395	6396	6436	6437	6438	6439	6440	6519	6520
6521	6522	6551	6552	6553	6587	6588	6589	6660	6661	6662	6663
6743	6744	6745	6746	6975	6977	6978	6979	6980	6982	6983	6984
6985	6985										

Table B.5: Analyzed runs measured without target in place during the WA98 p+C beamtime collisions at 17.4 GeV.

C. Bad Module Maps

C.1 PHENIX
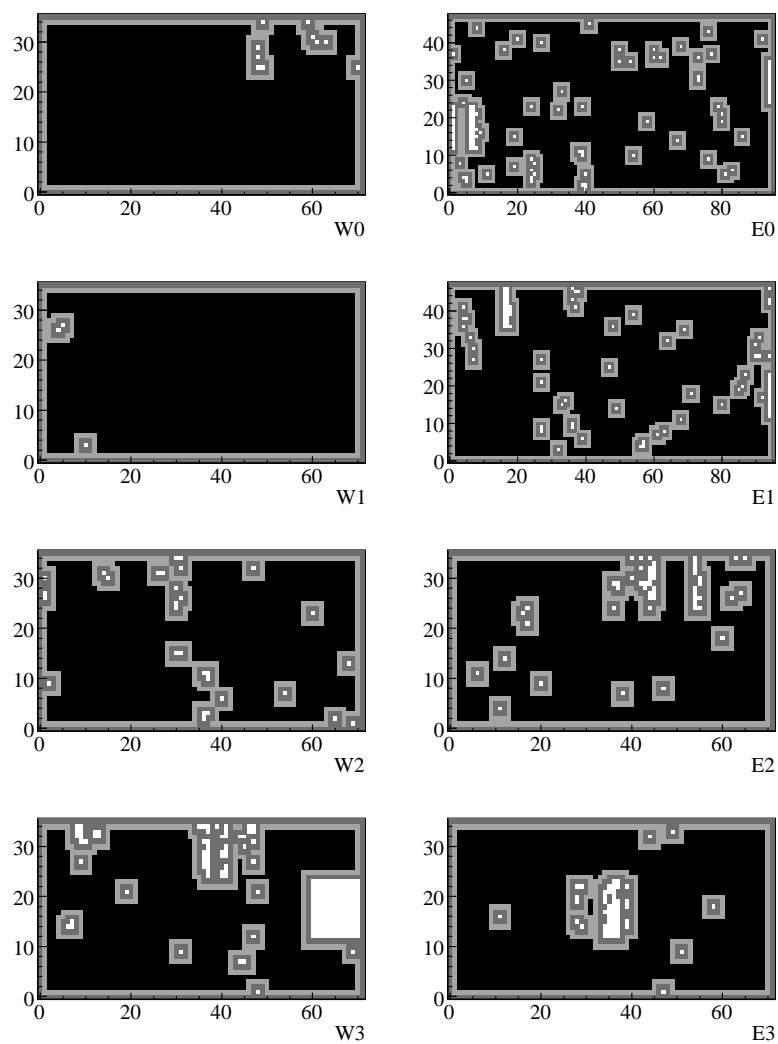
Figure C.1: Defective modules are marked white, the grey area denotes modules excluded because of a neighboring defective module or being on the edge of the detector. Black denotes the active area.

C.2   WA98
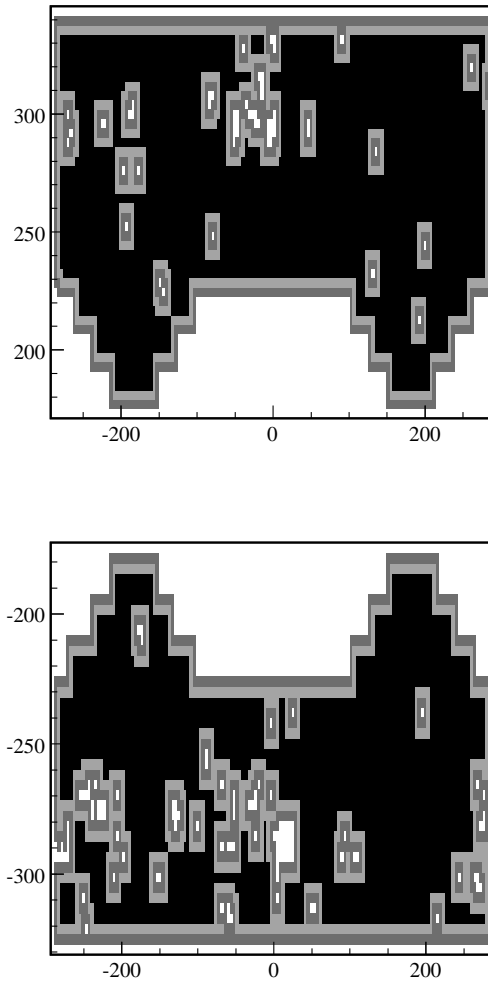
Figure C.2: Defective modules in the p+Pb analysis are marked white, the grey area denotes modules excluded because of a neighboring defective module or being on the edge of the detector. Black denotes the active area.
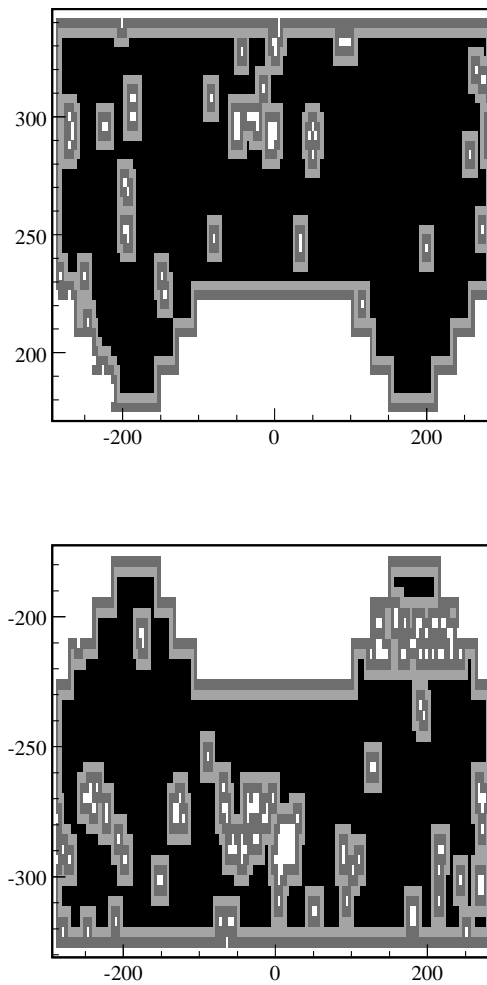
Figure C.3: Defective modules in the p+C analysis are marked white, the grey area denotes modules excluded because of a neighboring defective module or being on the edge of the detector. Black denotes the active area.

D. Data Tables

D.1 PHENIX

D.1.1 Neutral Pion Yields

p_{T}	Yield	stat. error	sys. error
1.25	0.132137	0.00223868	0.0158933
1.75	0.0159602	0.000213942	0.0013676
2.25	0.00225962	4.14702e-05	0.000193006
2.75	0.000341375	1.07496e-05	2.92078e-05
3.25	6.34089e-05	3.27351e-06	5.41776e-06
3.75	1.08788e-05	1.1072e-06	9.30863e-07
4.25	2.29169e-06	4.18826e-07	1.9601e-07
4.75	5.18474e-07	1.70295e-07	4.45024e-08
5.25	6.17862e-08	6.17894e-08	7.46335e-09

Table D.1: Lorentz invariant neutral pion yields from Cu+Cu minimum bias events at $\sqrt{s_{\mathrm{NN}}} = 22.4$ GeV.

p_{T}	Yield	stat. error	sys. error
1.25	0.245367	0.00459288	0.0209903
1.75	0.0294407	0.000627943	0.00251541
2.25	0.00401614	0.000123779	0.00034358
2.75	0.000671786	3.19771e-05	5.74065e-05
3.25	0.000135278	9.76004e-06	1.15602e-05
3.75	1.95736e-05	3.14518e-06	1.68692e-06
4.25	4.98392e-06	1.29336e-06	4.31802e-07
4.75	1.30595e-06	5.67068e-07	1.14753e-07

Table D.2: Lorentz invariant neutral pion yields for the $0 - 10\%$ most central Cu+Cu events at $\sqrt{s_{\mathrm{NN}}} = 22.4$ GeV.

p_T	Yield	stat. error	sys. error
1.25	0.159757	0.00287763	0.0136777
1.75	0.0207559	0.000423408	0.00177549
2.25	0.00296133	8.70844e-05	0.000253602
2.75	0.000434173	2.3719e-05	3.7086e-05
3.25	8.47485e-05	7.23336e-06	7.26211e-06
3.75	1.422e-05	2.56156e-06	1.21493e-06
4.25	3.29767e-06	9.6877e-07	2.81668e-07
4.75	5.68337e-07	4.01917e-07	6.86512e-08

Table D.3: Lorentz invariant neutral pion yields for the $10 - 20\%$ most central Cu+Cu events at $\sqrt{s_{NN}} = 22.4$ GeV.

p_T	Yield	stat. error	sys. error
0.25	0.0898766	0.00743844	0.0301351
1.75	0.0130681	0.000620411	0.00204582
2.25	0.00213461	7.94425e-05	0.00018256
2.75	0.000312067	2.53557e-05	3.08111e-05
3.25	3.69904e-05	6.5132e-06	3.55311e-06
3.75	9.99428e-06	2.45919e-06	8.58186e-07
4.25	1.24372e-06	1.53615e-06	2.35521e-07

Table D.4: Lorentz invariant neutral pion yields for the $20 - 30\%$ most central Cu+Cu events at $\sqrt{s_{NN}} = 22.4$ GeV.

p_T	Yield	stat. error	sys. error
1.25	0.076856	0.00250074	0.00917489
1.75	0.00886227	0.000259077	0.000759485
2.25	0.00118294	8.07652e-05	0.00014133
2.75	0.000195915	1.68443e-05	1.67668e-05
3.25	2.41785e-05	9.23739e-06	4.21496e-06
3.75	6.11332e-06	2.01404e-06	5.22521e-07
4.75	5.57153e-07	5.57182e-07	6.73003e-08

Table D.5: Lorentz invariant neutral pion yields for the $30 - 40\%$ most central Cu+Cu events at $\sqrt{s_{NN}} = 22.4$ GeV.

p_T	Yield	stat. error	sys. error
1.25	0.0270897	0.00265971	0.0086234
1.75	0.00427272	0.000146001	0.000365419
2.25	0.000692107	3.80005e-05	5.9213e-05
2.75	9.8326e-05	1.2837e-05	9.56312e-06
3.25	1.89332e-05	4.034e-06	1.61719e-06
3.75	1.59681e-06	1.00349e-06	1.37274e-07
4.75	6.51993e-07	5.36934e-07	6.48543e-08
5.25	4.86569e-07	4.86594e-07	5.87742e-08

Table D.6: Lorentz invariant neutral pion yields for the $40 - 50\%$ most central Cu+Cu events at $\sqrt{s_{\mathrm{NN}}} = 22.4$ GeV.

p_T	Yield	stat. error	sys. error
1.25	0.0165547	0.00215079	0.00543396
1.75	0.00250568	0.000220792	0.00040204
2.25	0.00036573	3.06358e-05	3.14236e-05
2.75	6.50361e-05	1.02245e-05	5.64081e-06
3.25	1.27428e-05	3.73232e-06	1.12682e-06
3.75	3.27982e-06	1.8939e-06	3.9618e-07

Table D.7: Lorentz invariant neutral pion yields for the $50 - 60\%$ most central Cu+Cu events at $\sqrt{s_{\mathrm{NN}}} = 22.4$ GeV.

p_T	Yield	stat. error	sys. error
1.25	0.0101399	0.000358751	0.000978185
1.75	0.00130017	6.0029e-05	0.000111355
2.25	0.000164559	1.53632e-05	1.40562e-05
2.75	2.26036e-05	4.49903e-06	1.93227e-06
3.25	2.92558e-06	1.52341e-06	2.6077e-07
3.75	1.35897e-06	9.61035e-07	1.64154e-07

Table D.8: Lorentz invariant neutral pion yields for the $60 - 82\%$ most central Cu+Cu events at $\sqrt{s_{\mathrm{NN}}} = 22.4$ GeV.

D.1.2   Nuclear Modification Factor

p_{T}	R_{AA}	stat. error	sys. error
1.25	0.636529	0.0119148	0.0954221
1.75	0.887553	0.0189307	0.137682
2.25	1.13354	0.0349362	0.179976
2.75	1.50047	0.0714226	0.254454
3.25	2.09506	0.151155	0.398412
3.75	1.89421	0.304371	0.422879
4.25	2.779	0.721168	0.763369

Table D.9: Nuclear modification factor for the $0 - 10\%$ most central Cu+Cu events at $\sqrt{s_{\mathrm{NN}}} = 22.4$ GeV.

p_{T}	R_{AA}	stat. error	sys. error
1.25	0.622988	0.0112216	0.0934169
1.75	0.940602	0.0191877	0.145964
2.25	1.25642	0.0369477	0.199545
2.75	1.45773	0.0796364	0.24718
3.25	1.97297	0.168394	0.375402
3.75	2.0686	0.372632	0.461217
4.25	2.76403	0.812	0.758196

Table D.10: Nuclear modification factor for the $10 - 20\%$ most central Cu+Cu events at $\sqrt{s_{\mathrm{NN}}} = 22.4$ GeV.

p_T	R_{AA}	stat. error	sys. error
1.25	0.549501	0.0454782	0.19627
1.75	0.928493	0.0440804	0.188628
2.25	1.41993	0.0528447	0.225427
2.75	1.64272	0.133473	0.290182
3.25	1.35014	0.23773	0.263493
3.75	2.27944	0.56088	0.508604

Table D.11: Nuclear modification factor for the $20 - 30\%$ most central Cu+Cu events at $\sqrt{s_\mathrm{NN}} = 22.4$ GeV.

p_T	R_{AA}	stat. error	sys. error
1.25	0.738227	0.0240204	0.126592
1.75	0.98924	0.0289192	0.153597
2.25	1.23624	0.0844042	0.221711
2.75	1.62022	0.139303	0.274867
3.25	1.38647	0.529699	0.337487
3.75	2.19051	0.721666	0.488428

Table D.12: Nuclear modification factor for the $30 - 40\%$ most central Cu+Cu events at $\sqrt{s_\mathrm{NN}} = 22.4$ GeV.

p_T	R_{AA}	stat. error	sys. error
1.25	0.431782	0.0423931	0.147368
1.75	0.791424	0.0270434	0.122806
2.25	1.20022	0.0658987	0.190566
2.75	1.34935	0.176165	0.237253
3.25	1.80157	0.383852	0.342568

Table D.13: Nuclear modification factor for the $40 - 50\%$ most central Cu+Cu events at $\sqrt{s_\mathrm{NN}} = 22.4$ GeV.

p_T	R_{AA}	stat. error	sys. error
0.25	0.434713	0.056478	0.152397
1.75	0.76463	0.0673766	0.157648
2.25	1.04489	0.0875261	0.166109
2.75	1.47038	0.231163	0.250305
3.25	1.99762	0.585097	0.382588

Table D.14: Nuclear modification factor for the $50 - 60\%$ most central Cu+Cu events at $\sqrt{s_\mathrm{NN}} = 22.4$ GeV.

p_T	R_{AA}	stat. error	sys. error
1.25	0.740218	0.026189	0.11577
1.75	1.10299	0.0509251	0.171226
2.25	1.307	0.122021	0.207423
2.75	1.42069	0.282774	0.240947
3.25	1.27499	0.663912	0.244605

Table D.15: Nuclear modification factor for the $60 - 82\%$ most central Cu+Cu events at $\sqrt{s_\mathrm{NN}} = 22.4$ GeV.

D.2 WA98

D.2.1 Neutral Pion Yields

p_{T}	Yield	stat. error	sys. error	tot. error
0.75	0.0494898	0.00460116	0.00630922	0.00780877
0.85	0.0290865	0.00252947	0.00359224	0.00439345
0.95	0.0177778	0.00155275	0.00216583	0.00266493
1.05	0.0112158	0.0009312	0.00136673	0.00165381
1.15	0.00727567	0.000598085	0.000896436	0.00107764
1.25	0.00514637	0.000420271	0.00064657	0.000771155
1.35	0.00245211	0.00027901	0.00031625	0.000421735
1.45	0.00160545	0.000201184	0.000213694	0.000293496
1.55	0.000982335	0.000138026	0.000135542	0.00019345
1.65	0.000526029	1.82462e-05	7.5516e-05	7.76891e-05
1.75	0.000341893	1.34121e-05	5.1228e-05	5.29546e-05
1.85	0.000240375	1.05813e-05	3.76958e-05	3.91528e-05
1.95	0.000147434	7.47751e-06	2.42577e-05	2.53841e-05
2.05	0.000100825	6.1604e-06	1.74428e-05	1.84987e-05
2.15	5.76026e-05	4.41741e-06	1.04984e-05	1.13899e-05
2.3	3.02999e-05	2.06313e-06	5.98996e-06	6.33531e-06
2.5	1.08798e-05	1.13512e-06	2.408e-06	2.66214e-06
2.7	5.08044e-06	7.22512e-07	1.26335e-06	1.45536e-06
2.9	1.76276e-06	3.92199e-07	4.93376e-07	6.30269e-07
3.25	4.89265e-07	1.08427e-07	1.68406e-07	2.00292e-07

Table D.16: Lorentz invariant neutral pion yields from p+C collisions at $\sqrt{s_{\mathrm{NN}}} = 17.4$ GeV.

p_{T}	Yield	stat. error	sys. error	tot. error
0.75	0.100596	0.00646491	0.0128245	0.0143619
0.85	0.0588111	0.00373194	0.00726328	0.00816595
0.95	0.0348637	0.00225819	0.00424737	0.00481036
1.05	0.0176801	0.00140189	0.00215445	0.00257039
1.15	0.0130375	0.000904602	0.00160636	0.00184355
1.25	0.00675733	0.000624694	0.000848965	0.00105403
1.35	0.00467066	0.000425752	0.000602376	0.000737646
1.45	0.00283319	0.000283241	0.000377115	0.000471636
1.55	0.00187367	0.000213128	0.000258527	0.000335052
1.65	0.00124564	5.88275e-05	0.000178823	0.000188251
1.75	0.000876128	4.46337e-05	0.000131276	0.000138656
1.85	0.000612928	3.52675e-05	9.612e-05	0.000102386
1.95	0.000349837	2.5212e-05	5.75599e-05	6.28394e-05
2.05	0.000254814	1.97529e-05	4.4083e-05	4.83062e-05
2.15	0.000143731	1.43242e-05	2.6196e-05	2.98565e-05
2.3	8.64856e-05	7.39067e-06	1.70973e-05	1.86263e-05
2.5	4.38564e-05	4.87332e-06	9.70662e-06	1.08613e-05
2.7	1.35765e-05	2.58273e-06	3.37605e-06	4.25068e-06
2.9	6.09117e-06	1.58554e-06	1.70485e-06	2.32818e-06
3.25	1.41355e-06	4.01528e-07	4.86546e-07	6.30834e-07

Table D.17: Lorentz invariant neutral pion yields from p+Pb collisions at $\sqrt{s_{\mathrm{NN}}} = 17.4$ GeV.

D.2.2   Nuclear Modification Factors

p_T (GeV/c)	p+Pb		p+C	
	R'_{AA}	total error	R'_{AA}	total error
0.75	1.45712	0.218439	1.32503	0.217673
0.85	1.5618	0.224028	1.41272	0.219367
0.95	1.36767	0.194303	1.19989	0.184396
1.05	1.67102	0.246131	1.17842	0.175982
1.15	1.52404	0.214611	1.22176	0.180277
1.25	1.74182	0.269348	1.02316	0.151879
1.35	1.56687	0.244652	1.33517	0.227439
1.45	1.58423	0.25908	1.25073	0.225317
1.55	1.74302	0.302731	1.4873	0.285969
1.65	1.37375	0.205093	1.45532	0.212205
1.75	1.26289	0.20654	1.4478	0.232058
1.85	0.975361	0.183086	1.11263	0.204744
1.95	1.39699	0.272954	1.48295	0.279626
2.05	1.12581	0.254589	1.27288	0.281367
2.15	1.376	0.363949	1.53601	0.394333
2.3	1.03368	0.193619	1.31994	0.237659
2.5	0.840321	0.220923	1.51538	0.394162
2.7	1.20442	0.459227	1.43989	0.517989
2.9	1.21439	0.587015	1.8773	0.871284
3.25	0.933437	0.462286	1.20647	0.557722

Table D.18: Nuclear modification factor for the $82.8-100\%$ most central central Pb+Pb collisions at $\sqrt{s_{\mathrm{NN}}} = 17.4$ GeV.

p_{T} (GeV/c)	p+Pb		p+C	
	R'_{AA}	total error	R'_{AA}	total error
0.75	1.18391	0.189949	1.07659	0.187262
0.85	1.21554	0.18785	1.09952	0.182064
0.95	1.18369	0.178059	1.03848	0.167649
1.05	1.35787	0.216322	0.957588	0.154364
1.15	1.39252	0.206191	1.11632	0.172464
1.25	1.5131	0.244654	0.888807	0.138455
1.35	1.55164	0.252933	1.32219	0.233582
1.45	1.60893	0.271475	1.27023	0.234835
1.55	1.70595	0.309081	1.45567	0.289783
1.65	1.55914	0.240831	1.65172	0.249578
1.75	1.51074	0.249773	1.73194	0.280757
1.85	1.10274	0.21434	1.25794	0.240022
1.95	1.4628	0.300915	1.55281	0.309381
2.05	0.907477	0.252908	1.02602	0.281725
2.15	1.01236	0.345152	1.13009	0.378515
2.3	1.28262	0.240445	1.63782	0.295155
2.5	1.07056	0.250534	1.93057	0.445724
2.7	1.64302	0.516034	1.96425	0.564799
2.9	1.05438	0.538155	1.62993	0.802244
3.25	1.28786	0.662769	1.66456	0.803946

Table D.19: Nuclear modification factor for the $67.0-82.8\%$ most central central Pb+Pb collisions at $\sqrt{s_{\mathrm{NN}}} = 17.4$ GeV.

p_T (GeV/c)	p+Pb		p+C	
	R'_{AA}	total error	R'_{AA}	total error
0.75	0.986535	0.156978	0.897106	0.15495
0.85	1.12686	0.169668	1.01931	0.165009
0.95	1.15006	0.169523	1.00898	0.160046
1.05	1.44055	0.217503	1.01589	0.155411
1.15	1.20068	0.174226	0.962533	0.145972
1.25	1.35432	0.214196	0.795536	0.121006
1.35	1.2183	0.195513	1.03815	0.180981
1.45	1.36907	0.226311	1.08086	0.19645
1.55	1.20335	0.217247	1.02681	0.203807
1.65	1.21958	0.181138	1.29199	0.187372
1.75	1.31601	0.204666	1.5087	0.229451
1.85	1.10474	0.188376	1.26022	0.209753
1.95	1.45628	0.262521	1.54589	0.2672
2.05	1.06096	0.23248	1.19955	0.256543
2.15	1.12713	0.285759	1.2582	0.308772
2.3	1.23154	0.22414	1.5726	0.274451
2.5	1.13658	0.253647	2.04964	0.450646
2.7	1.78765	0.557843	2.13715	0.609791
2.9	1.83531	0.749684	2.83716	1.09369
3.25	1.46172	0.909761	1.88928	1.12693

Table D.20: Nuclear modification factor for the $48.8-67.0\%$ most central central Pb+Pb collisions at $\sqrt{s_\mathrm{NN}} = 17.4$ GeV.

p_{T} (GeV/c)	p+Pb		p+C	
	R'_{AA}	total error	R'_{AA}	total error
0.75	0.885067	0.141218	0.804836	0.139336
0.85	0.924348	0.140019	0.836119	0.136064
0.95	0.857446	0.130018	0.75226	0.122288
1.05	1.03679	0.161586	0.731157	0.115365
1.15	0.897814	0.132961	0.719738	0.111211
1.25	1.14185	0.183107	0.67073	0.103558
1.35	1.12736	0.18024	0.96065	0.166939
1.45	1.14354	0.190712	0.902808	0.165297
1.55	1.09121	0.197828	0.931119	0.185456
1.65	1.13244	0.171421	1.19969	0.177482
1.75	1.00484	0.162192	1.15196	0.182131
1.85	1.06055	0.179178	1.20981	0.199419
1.95	1.07458	0.210771	1.14071	0.215984
2.05	1.02676	0.214269	1.16089	0.235844
2.15	1.39137	0.31487	1.55316	0.337297
2.3	1.14965	0.203761	1.46802	0.248902
2.5	1.08389	0.231121	1.95462	0.410032
2.7	1.66967	0.502848	1.9961	0.545694
2.9	2.12098	0.827343	3.27876	1.1998
3.25	3.07706	1.44505	3.97711	1.72886

Table D.21: Nuclear modification factor for the $25.3-48.8\%$ most central central Pb+Pb collisions at $\sqrt{s_{\mathrm{NN}}} = 17.4$ GeV.

p_{T} (GeV/c)	p+Pb		p+C	
	R'_{AA}	total error	R'_{AA}	total error
0.75	0.71632	0.112261	0.651386	0.11107
0.85	0.705782	0.105369	0.638415	0.102594
0.95	0.713273	0.10443	0.625774	0.0986842
1.05	0.975379	0.146996	0.687848	0.105037
1.15	0.761781	0.108624	0.610686	0.0911452
1.25	0.925212	0.14326	0.543477	0.0807902
1.35	0.949084	0.145918	0.808738	0.135992
1.45	1.03531	0.165202	0.817366	0.144308
1.55	0.986719	0.167292	0.84196	0.158746
1.65	0.879742	0.12193	0.931978	0.125669
1.75	0.868282	0.124512	0.995413	0.139028
1.85	0.700678	0.109926	0.79929	0.121849
1.95	0.993923	0.16155	1.05509	0.162761
2.05	0.872764	0.15612	0.986773	0.17012
2.15	1.2858	0.244414	1.43532	0.257088
2.3	1.03015	0.166942	1.31543	0.202062
2.5	0.95588	0.187283	1.72377	0.331238
2.7	1.41026	0.390006	1.68597	0.414746
2.9	1.42045	0.516311	2.19583	0.740966
3.25	1.84445	0.754839	2.38397	0.878866

Table D.22: Nuclear modification factor for the $13.0-25.3\%$ most central central Pb+Pb collisions at $\sqrt{s_{\mathrm{NN}}} = 17.4$ GeV.

p_{T} (GeV/c)	p+Pb		p+C	
	R'_{AA}	total error	R'_{AA}	total error
0.75	0.588062	0.0845651	0.534755	0.0848778
0.85	0.6369	0.0876131	0.576108	0.0863378
0.95	0.651459	0.0874206	0.571543	0.083689
1.05	0.812316	0.113023	0.572855	0.0809429
1.15	0.665238	0.0877637	0.533292	0.0741798
1.25	0.811971	0.117252	0.476958	0.0657012
1.35	0.762692	0.109004	0.649909	0.102891
1.45	0.795613	0.118251	0.628127	0.104729
1.55	0.83668	0.13228	0.713932	0.127312
1.65	0.778062	0.0941974	0.82426	0.0962303
1.75	0.751993	0.0927886	0.862098	0.102618
1.85	0.703804	0.0907	0.802857	0.0990958
1.95	0.787418	0.109662	0.835873	0.108258
2.05	0.763371	0.111737	0.86309	0.119435
2.15	0.927605	0.152452	1.03547	0.156901
2.3	0.819736	0.128133	1.04675	0.154432
2.5	0.741195	0.137803	1.33663	0.243192
2.7	1.14116	0.293765	1.36427	0.305985
2.9	1.21336	0.403395	1.8757	0.569781
3.25	1.5352	0.607764	1.98426	0.70196

Table D.23: Nuclear modification factor for the $6.8 - 13.0\%$ most central central Pb+Pb collisions at $\sqrt{s_{\mathrm{NN}}} = 17.4$ GeV.

p_{T} (GeV/c)	p+Pb		p+C	
	R'_{AA}	total error	R'_{AA}	total error
0.75	0.511018	0.0733689	0.464694	0.0736612
0.85	0.559497	0.0768964	0.506093	0.0757878
0.95	0.61833	0.0829131	0.542477	0.0793834
1.05	0.771802	0.107453	0.544284	0.0769526
1.15	0.591865	0.0781401	0.474472	0.066041
1.25	0.748407	0.108107	0.43962	0.0605789
1.35	0.682768	0.0976551	0.581803	0.0921652
1.45	0.695968	0.103498	0.549459	0.0916521
1.55	0.640164	0.101702	0.546247	0.0977812
1.65	0.643723	0.0782259	0.681945	0.0799366
1.75	0.565036	0.0708906	0.647767	0.0784958
1.85	0.552775	0.0720835	0.630572	0.0788389
1.95	0.654368	0.0920088	0.694636	0.0909652
2.05	0.587471	0.0872087	0.664213	0.0933702
2.15	0.755131	0.125493	0.842941	0.129405
2.3	0.678674	0.106405	0.866622	0.128292
2.5	0.587017	0.110025	1.05859	0.194239
2.7	0.866531	0.225481	1.03594	0.235653
2.9	0.883456	0.299503	1.36571	0.424636
3.25	0.955453	0.387729	1.23493	0.450542

Table D.24: Nuclear modification factor for the $1.0 - 6.8\%$ most central central Pb+Pb collisions at $\sqrt{s_{\mathrm{NN}}} = 17.4$ GeV.

p_{T} (GeV/c)	p+Pb		p+C	
	R'_{AA}	total error	R'_{AA}	total error
0.75	0.547462	0.0776705	0.497835	0.0781487
0.85	0.596901	0.0811646	0.539927	0.0801307
0.95	0.638994	0.0848507	0.560607	0.081367
1.05	0.801835	0.110599	0.565464	0.0792283
1.15	0.633371	0.0827461	0.507745	0.0700082
1.25	0.779319	0.11151	0.457778	0.0624263
1.35	0.723662	0.102409	0.61665	0.0968435
1.45	0.732652	0.107748	0.57842	0.095636
1.55	0.732341	0.114823	0.624901	0.110709
1.65	0.665851	0.0789495	0.705387	0.0805239
1.75	0.643439	0.078042	0.737649	0.0861964
1.85	0.614331	0.077459	0.700791	0.0844587
1.95	0.698673	0.0950497	0.741668	0.0934803
2.05	0.646983	0.0922506	0.731498	0.0982899
2.15	0.790484	0.126591	0.882406	0.129672
2.3	0.711637	0.110456	0.908713	0.133011
2.5	0.637956	0.117492	1.15045	0.20726
2.7	0.956199	0.244416	1.14314	0.254007
2.9	0.977985	0.322256	1.51184	0.454365
3.25	1.187	0.465112	1.53421	0.535788

Table D.25: Nuclear modification factor for the $0.0 - 13.0\%$ most central central Pb+Pb collisions at $\sqrt{s_{\mathrm{NN}}} = 17.4$ GeV.

p_{T} (GeV/c)	p+Pb		p+C	
	R'_{AA}	total error	R'_{AA}	total error
0.75	0.462905	0.0722292	0.420943	0.0715113
0.85	0.522961	0.076841	0.473044	0.0749827
0.95	0.598978	0.0852443	0.5255	0.0808777
1.05	0.771347	0.113675	0.543963	0.0812757
1.15	0.611204	0.086446	0.489975	0.0725878
1.25	0.692728	0.105905	0.406914	0.0596586
1.35	0.631109	0.0964758	0.537783	0.0899979
1.45	0.565168	0.0911336	0.446194	0.0794559
1.55	0.610759	0.105064	0.521156	0.0994237
1.65	0.531851	0.0766209	0.56343	0.0791362
1.75	0.480525	0.0731943	0.550882	0.0819787
1.85	0.491716	0.0781132	0.56092	0.0866488
1.95	0.51682	0.09304	0.548624	0.0946867
2.05	0.444815	0.0874208	0.502922	0.0958842
2.15	0.444188	0.105972	0.49584	0.114008
2.3	0.424331	0.0750349	0.541843	0.0916386
2.5	0.333213	0.0758088	0.600895	0.134764
2.7	0.449522	0.1423	0.537407	0.155982
2.9	0.350799	0.161797	0.54229	0.239146
3.25	0.350947	0.162741	0.453601	0.194287

Table D.26: Nuclear modification factor for the $0.0 - 1.0\%$ most central central Pb+Pb collisions at $\sqrt{s_{\mathrm{NN}}} = 17.4$ GeV.

Bibliography

[Abe07] B. I. Abelev *et al.*, *Phys. Rev. Lett.* **98** (2007) 192301.

[Ack03] K. H. Ackermann *et al.*, *Nucl. Instrum. Meth.* **A499** (2003) 624.

[Ada03a] M. Adamczyk *et al.*, *Nucl. Instrum. Meth.* **A499** (2003) 437.

[Ada03b] J. Adams *et al.*, *Phys. Rev. Lett.* **91** (2003) 172302.

[Ada05] J. Adams *et al.*, *Nucl. Phys.* **A757** (2005) 102.

[Ada08a] A. Adare *et al.*, *Phys. Rev.* **C78** (2008) 014901.

[Ada08b] A. Adare *et al.*, *Enhanced production of direct photons in Au+Au collisions at $\sqrt{s_{NN}}$=200 GeV*, arXiv:0804.4168v1 [nucl-ex], 2008.

[Ada08c] A. Adare *et al.*, *Phys. Rev. Lett.* **101** (2008) 162301.

[Adc02] K. Adcox *et al.*, *Phys. Rev. Lett.* **88** (2002) 022301.

[Adc03a] K. Adcox *et al.*, *Nucl. Instrum. Meth.* **A499** (2003) 489.

[Adc03b] K. Adcox *et al.*, *Nucl. Instrum. Meth.* **A499** (2003) 469.

[Adc05] K. Adcox *et al.*, *Nucl. Phys.* **A757** (2005) 184.

[Adl02] C. Adler *et al.*, *Phys. Rev. Lett.* **89** (2002) 202301.

[Adl03a] C. Adler *et al.*, *Phys. Rev. Lett.* **90** (2003) 082302.

[Adl03b] C. Adler *et al.*, *Nucl. Instrum. Meth.* **A499** (2003) 433.

[Adl03c] S. S. Adler *et al.*, *Nucl. Instrum. Meth.* **A499** (2003) 593.

[Adl03d] S. S. Adler *et al.*, *Nucl. Instrum. Meth.* **A499** (2003) 560.

[Adl05a] S. S. Adler *et al.*, *Phys. Rev. Lett.* **94** (2005) 232301.

[Adl05b] S. S. Adler *et al.*, *Phys. Rev.* **D71** (2005) 071102.

[Adl06]   S. S. Adler *et al.*, *Phys. Rev. Lett.* **96** (2006) 202301.

[Adl07a] S. S. Adler *et al.*, *Phys. Rev.* **C76** (2007) 034904.

[Adl07b] S. S. Adler *et al.*, *Phys. Rev. Lett.* **98** (2007) 012002.

[Agg00a] M. M. Aggarwal *et al.*, *Direct photon production in 158-A-GeV Pb-208 + Pb-208 collisions*, arXiv:nucl-ex/0006007v2, 2000.

[Agg00b] M. M. Aggarwal *et al.*, *Phys. Rev. Lett.* **85** (2000) 3595.

[Agg02]   M. M. Aggarwal *et al.*, *Eur. Phys. J.* **C23** (2002) 225.

[Agg04]   M. M. Aggarwal *et al.*, *Phys. Rev. Lett.* **93** (2004) 022301.

[Agg08]   M. M. Aggarwal *et al.*, *Phys. Rev. Lett.* **100** (2008) 242301.

[Ake90]   T. Akesson *et al.*, *Z. Phys.* **C46** (1990) 361.

[Aki03]   H. Akikawa *et al.*, *Nucl. Instrum. Meth.* **A499** (2003) 537.

[Ala96]   J. Alam, B. Sinha, and S. Raha, *Phys. Rept.* **273** (1996) 243.

[Alb91]   R. Albrecht *et al.*, *Z. Phys.* **C51** (1991) 1.

[Alb96]   R. Albrecht *et al.*, *Phys. Rev. Lett.* **76** (1996) 3506.

[Alb08]   S. Albino, B. A. Kniehl, and G. Kramer, *Nucl. Phys.* **B803** (2008) 42.

[All03]   M. Allen *et al.*, *Nucl. Instrum. Meth.* **A499** (2003) 549.

[Alt06]   C. Alt *et al.*, *Eur. Phys. J.* **C45** (2006) 343.

[Alt07]   C. Alt *et al.*, *Eur. Phys. J.* **C49** (2007) 897.

[Alt08]   C. Alt *et al.*, *Phys. Rev.* **C77** (2008) 034906.

[Ams08]   C. Amsler *et al.*, *Phys. Lett.* **B667** (2008) 1.

[And09]   A. Andronic, P. Braun-Munzinger, and J. Stachel, *Phys. Lett.* **B673** (2009) 142.

[Ang91]   A. L. S. Angelis, P. Dönni, and E. Durieux, *Proposal for a large acceptance hadron and photon spectrometer*, CERN Scientific Committee Paper, 1991, proposal for the WA98 experiment.

[Ant79]   D. Antreasyan *et al.*, *Phys. Rev.* **D19** (1979) 764.

[Ant05]   F. Antinori *et al.*, *Phys. Lett.* **B623** (2005) 17.

[Aok09]   Y. Aoki *et al.*, *The QCD transition temperature: results with physical masses in the continuum limit II*, arXiv:0903.4155v1 [hep-lat], 2009.

[Aph03]   L. Aphecetche *et al.*, *Nucl. Instrum. Meth.* **A499** (2003) 521.

[Arl07]   F. Arleo, *JHEP* **07** (2007) 032.

[Arl08]   F. Arleo and D. d'Enterria, *Phys. Rev.* **D78** (2008) 094004.

[Arn83]   G. Arnison *et al.*, *Phys. Lett.* **B123** (1983) 115.

[Ars03]   I. Arsene *et al.*, *Phys. Rev. Lett.* **91** (2003) 072305.

[Ars04]   I. Arsene *et al.*, *Phys. Rev. Lett.* **93** (2004) 242303.

[Ars05]   I. Arsene *et al.*, *Nucl. Phys.* **A757** (2005) 1.

[Ars07]   I. Arsene *et al.*, *Phys. Lett.* **B650** (2007) 219.

[Ath80]   H. W. Atherton *et al.*, *Precise Measurements of Particle Production by 400 GeV/c Protons on Beryllium Targets*, CERN yellow report 80-07, CERN, 1980.

[Aur00]   P. Aurenche, M. Fontannaz, J. P. Guillet, *et al.*, *Eur. Phys. J.* **C13** (2000) 347.

[Aur06]   P. Aurenche, M. Fontannaz, J.-P. Guillet, *et al.*, *Phys. Rev.* **D73** (2006) 094007.

[Bac03]   B. B. Back *et al.*, *Nucl. Instrum. Meth.* **A499** (2003) 603.

[Bac05]   B. B. Back *et al.*, *Nucl. Phys.* **A757** (2005) 28.

[Bad82]   A. R. Baden *et al.*, *Nucl. Instr. Meth.* **203** (1982) 189.

[Bat07]   S. Bathe, *Eur. Phys. J.* **C49** (2007) 225.

[Bau96]   R. Baur *et al.*, *Z. Phys.* **C71** (1996) 571.

[Bau97]   R. Baur *et al.*, *Z. Phys.* **C74** (1997) 593.

[Bau06] C. Baumann, C. Klein-Bösing, and K. Reygers, *Combined PbSc+PbGl π^0 Spectra for $\sqrt{s} = 22.4$ GeV Cu+Cu*, February 2006, PHENIX Internal Analysis Note 546.

[Ben]   J. Benjamin *et al.* Prepared for IEEE Particle Accelerator Conference (PAC 99), New York, New York, 29 Mar - 2 Apr 1999.

[Bia08] A. Bialas, *J. Phys.* **G35** (2008) 044053.

[Bie09a] J. Bielcikova, *Near-side high-p(T) correlations: the ridge*, Submitted to European Physical Journal C, 2009.

[Bie09b] J. Bielcikova, *private communication*, 2009.

[Bjo82] J. D. Bjorken, *Energy Loss of Energetic Partons in Quark - Gluon Plasma: Possible Extinction of High p(t) Jets in Hadron - Hadron Collisions*, FERMILAB-PUB-82-059-THY, 1982.

[Bla00] S. R. Blattnig, S. R. Swaminathan, A. T. Kruger, *et al.*, *Phys. Rev.* **D62** (2000) 094030.

[Blu98] C. Blume, *Produktion neutraler Mesonen in heißer hadronischer Materie*, Ph.D. thesis, Institut für Kernphysik, Westfälische Wilhelms-Universität Münster, 1998.

[Blu07] C. Blume, *Nucl. Phys.* **A783** (2007) 65.

[BM03]   P. Braun-Munzinger, K. Redlich, and J. Stachel, *Particle production in heavy ion collisions*, 2003.

[BM07]   P. Braun-Munzinger and J. Stachel, *Nature* **448** (2007) 302.

[BM09]   P. Braun-Munzinger and J. Stachel, *Charmonium from Statistical Hadronization of Heavy Quarks – a Probe for Deconfinement in the Quark-Gluon Plasma*, 2009.

[Bou01] L. Bourhis, M. Fontannaz, J. P. Guillet, *et al.*, *Eur. Phys. J.* **C19** (2001) 89.

[Bra08] E. L. Bratkovskaya, S. M. Kiselev, and G. B. Sharkov, *Phys. Rev.* **C78** (2008) 034905.

[Bro79] S. J. Brodsky, *Phys. Scripta* **19** (1979) 154.

[Buc99] D. Bucher, *Produktion direkter Photonen in ultrarelativistischen Schweri-onenstößen*, Ph.D. thesis, Institut für Kernphysik, Westfälische Wilhelms-Universität Münster, 1999.

[Bue02] H. Buesching, *Azimutale Photonen-Korrelationen in ultrarelativistischen p+A-, Pb+Pb- und Au+Au-Reaktionen*, Ph.D. thesis, Institut für Kern-physik, Westfälische Wilhelms-Universität Münster, 2002.

[Bur00] C. P. Burgess, *Phys. Rept.* **330** (2000) 193.

[Cap02] A. Capella, A. B. Kaidalov, and D. Sousa, *Phys. Rev.* **C65** (2002) 054908.

[Car01] J.-L. Caron, *Accelerator complex of CERN*, `http://cdsweb.cern.ch/record/42384`, 07 2001.

[Cha09] R. Chatterjee, L. Bhattacharya, and D. K. Srivastava, *Electromagnetic probes*, arXiv:0901.3610v1 [nucl-th], 2009.

[Cho74] A. Chodos, R. L. Jaffe, K. Johnson, *et al.*, *Phys. Rev.* **D9** (1974) 3471.

[Cla79] A. G. Clark *et al.*, *Nucl. Phys.* **B160** (1979) 397.

[Col75] J. C. Collins and M. J. Perry, *Phys. Rev. Lett.* **34** (1975) 1353.

[Cor79] M. D. Corcoran *et al.*, *Phys. Scripta* **19** (1979) 95.

[Cro75] J. W. Cronin *et al.*, *Phys. Rev.* **D11** (1975) 3105.

[Dar76] P. Darriulat *et al.*, *Nucl. Phys.* **B110** (1976) 365.

[d'E04] D. G. d'Enterria, *Phys. Lett.* **B596** (2004) 32.

[d'E05] D. G. d'Enterria, *Eur. Phys. J.* **C43** (2005) 295.

[d'E09] D. d'Enterria, *Jet quenching in QCD matter: from RHIC to LHC*, arXiv:0902.2488v1 [nucl-ex], 2009.

[dF05] D. de Florian and W. Vogelsang, *Phys. Rev.* **D71** (2005) 114004.

[Dre05] A. Drees, *Eur. Phys. J.* **C43** (2005) 459.

[Ell96] R. K. Ellis, W. J. Stirling, and B. R. Webber, *Camb. Monogr. Part. Phys. Nucl. Phys. Cosmol.* **8** (1996) 1.

[Fel98] G. J. Feldman and R. D. Cousins, *Phys. Rev.* **D57** (1998) 3873.

[Fer84]   T. Ferbel and W. R. Molzon, *Rev. Mod. Phys.* **56 2** (1984) 181.

[Fra07]   J. Frantz, *J. Phys.* **G34** (2007) S389.

[Fuk98]   Y. Fukuda *et al.*, *Phys. Rev. Lett.* **81** (1998) 1562.

[Gal03]   C. Gale and K. L. Haglin, *Electromagnetic radiation from relativistic nuclear collisions*, arXiv:hep-ph/0306098v3, 2003.

[Gal09]   C. Gale, *Photon Production in Hot and Dense Strongly Interacting Matter*, arXiv:0904.2184v1 [hep-ph], 2009.

[GEA09]   *GEANT3 Homepage*, http://wwwasd.web.cern.ch/wwwasd/geant/, 2009.

[Gee95]   D. F. Geesaman, K. Saito, and A. W. Thomas, *Ann. Rev. Nucl. Part. Sci.* **45** (1995) 337.

[GM64]   M. Gell-Mann, *Phys. Lett.* **8** (1964) 214.

[Gro09]   D. D. Group, *The Durham HEP Databases: Parton Distribution Function Server*, http://durpdg.dur.ac.uk/hepdata/pdf, 2009.

[Gyu05]   M. Gyulassy and L. McLerran, *Nucl. Phys.* **A750** (2005) 30.

[Hah03]   H. Hahn *et al.*, *Nucl. Instrum. Meth.* **A499** (2003) 245.

[HBO09]   *HBOOK - Reference Manual*, http://wwwasdoc.web.cern.ch/wwwasdoc/hbook_html3/hboomain.html, 2009.

[Hei00]   U. W. Heinz and M. Jacob, *Evidence for a new state of matter: An assessment of the results from the CERN lead beam programme*, arXiv:nucl-th/0002042v1, 2000.

[Hij09]   *Hijing Monte Carlo Program*, http://www-nsdth.lbl.gov/ xnwang/hijing/index.html, 2009.

[Hor07]   M. J. Horner, *J. Phys.* **G34** (2007) S995.

[Ian02]   E. Iancu, A. Leonidov, and L. McLerran, *The colour glass condensate: An introduction*, arXiv:hep-ph/0202270v1, 2002.

[Jac78]   M. Jacob and P. V. Landshoff, *Phys. Rept.* **48** (1978) 285.

[Jac79]   M. Jacob, *Phys. Scripta* **19** (1979) 69.

[Jac80] M. Jacob and P. Landshoff, *Sci. Am.* **242** (1980) 46.

[Jan08] K. Jansen, *Lattice QCD: a critical status report*, arXiv:0810.5634v2 [hep-lat], 2008.

[Jon96] P. G. Jones *et al.*, *Nucl. Phys.* **A610** (1996) 188c.

[Kam97] K. H. Kampert *et al.*, *Z. Phys.* **C74** (1997) 587.

[Kap91] J. I. Kapusta, P. Lichard, and D. Seibert, *Phys. Rev.* **D44** (1991) 2774.

[KB00] C. Klein-Bösing, *Simulation der Detektoreigenschaften des Bleiglaskalorimeters den Experimenten WA98 und PHENIX*, Master's thesis, Westfälische Wilhelms-Universität Münster, 2000.

[KB04] C. Klein-Bösing, *Production of Neutral Pions and Direct Photons in Ultra-Relativistic Au+Au Collisions*, Ph.D. thesis, Institut für Kernphysik, Westfälische Wilhelms-Universität Münster, 2004.

[KB05] C. Klein-Bösing, K. Reygers, G. David, *et al.*, *Centrality dependence of Neutral Pion Production in sNN = 200 GeV Cu+Cu Collisions (Run05)*, July 2005, PHENIX Internal Analysis Note AN417.

[KB08] C. Klein-Boesing, *J. Phys.* **G35** (2008) 044026.

[Kni00] B. A. Kniehl, G. Kramer, and B. Potter, *Nucl. Phys.* **B582** (2000) 514.

[Kre00] S. Kretzer, *Phys. Rev. D* **62 5** (2000) 054001.

[Las08] A. Laszlo, *Nuclear modification at $\sqrt{s_{NN}}$ = 17.3 GeV, measured at NA49*, arXiv:0805.4771v1 [nucl-ex], 2008.

[Lin05] Z.-W. Lin, C. M. Ko, B.-A. Li, *et al.*, *Phys. Rev.* **C72** (2005) 064901.

[Lue07] R. Luechtenborg, *Produktion direkter Photonen in ultrarelativistischen Cu+Cu Stößen am PHENIX-Experiment*, Master's thesis, Westfälische Wilhelms-Universität Münster, 2007.

[MC02] M. J. Mora Corral, *Production de photons directs et de mesons neutres a grande impulsion transverse lors de collisions proton et pion sur noyau à 160 GeV*, Ph.D. thesis, Université de Nantes, 2002.

[Mil07] M. L. Miller, K. Reygers, S. J. Sanders, *et al.*, *Ann. Rev. Nucl. Part. Sci.* **57** (2007) 205.

[Owe87] J. F. Owens, *Rev. Mod. Phys.* **59** (1987) 465.

[Paw09] *PAW Physics Analysis Workstation,* http://wwwasd.web.cern.ch/wwwasd/paw/, 2009.

[Pei02] T. Peitzmann and M. H. Thoma, *Phys. Rept.* **364** (2002) 175.

[Per00] D. H. Perkins, *Introduction to High Energy Phyiscs*, Cambridge University Press, 4th edition, 2000.

[Per07] D. Peressounko, *Bose-Einstein correlations of direct photons in Au+Au collisions at $\sqrt{s_{NN}} = 200$ GeV*, arXiv:0704.0852v1 [nucl-ex], 2007.

[PHE09] *Homepage of the PHENIX Experiment,* http://www.phenix.bnl.gov/, 2009.

[Phi08] O. Philipsen, *Prog. Theor. Phys. Suppl.* **174** (2008) 206.

[Pov06] B. Povh, K. Rith, C. Scholz, *et al.*, *Teilchen und Kerne: Eine Einführung in die physikalischen Konzepte (Springer-Lehrbuch)*, Springer, 7. edition, September 2006.

[Pra09] S. Pratt, *Acta Phys. Polon.* **B40** (2009) 1249.

[Rad09] M. Radici and R. Jakob, *Fragmentaion Function Database*, http://www.pv.infn.it/ radici/FFdatabase/, 2009.

[Ram07] M. Rammler, *Produktion neutraler Pionen in ultrarelativistischen p+Pb und p+C Kollisionen*, Master's thesis, Westfälische Wilhelms-Universität Münster, 2007.

[Rey99] K. Reygers, *Teilchenproduktion in ultrarelativistischen p+Pb und Pb+Pb-Reaktionen*, Ph.D. thesis, Institut für Kernphysik, Westfälische Wilhelms-Universität Münster, 1999.

[Rey02] K. Reygers, *High-p(T) neutral pion production in heavy ion collisions at SPS and RHIC*, arXiv:nucl-ex/0202018v1, 2002.

[Rey05] K. Reygers, *Eur. Phys. J.* **C43** (2005) 393.

[Rey06] K. Reygers, C. Baumann, and J. Nagle, *Centrality Determination and Glauber Calculations for PHENIX Run-5 22.4 GeV Copper-Copper*, February 2006, PHENIX Internal Analysis Note.

[Rey08] K. Reygers, *J. Phys.* **G35** (2008) 104045.

[Roo09]   *ROOT Data Analysis Framework*, http://root.cern.ch, 2009.

[Rus07a] M. J. Russcher, *J. Phys.* **G34** (2007) S1033.

[Rus07b] M. J. Russcher, *Eur. Phys. J.* **C49** (2007) 231.

[Sah09]   B. Sahlmueller, *Photons at PHENIX*, arXiv:0904.4764 [nucl-ex], 2009.

[Sen06]   P. Senger, T. Galatyuk, D. Kresan, *et al.*, *PoS* **CPOD2006** (2006) 018.

[Shu80]   E. V. Shuryak, *Phys. Rept.* **61** (1980) 71.

[Sli03]   J. Slivova, *Azimuthal Correlations of high-p$_{\mathrm{T}}$ Pions in 158 AGeV/c Pb+Au Collisions Measured by the CERES Experiment*, Ph.D. thesis, Charles University in Prague, 2003.

[Sor09]   P. Sorensen, *Elliptic Flow: A Study of Space-Momentum Correlations In Relativistic Nuclear Collisions*, arXiv:0905.0174v3 [nucl-ex], 2009.

[Sta05]   P. Stankus, *Ann. Rev. Nucl. Part. Sci.* **55** (2005) 517.

[Ste98]   P. A. Steinberg, *Search for Disoriented Chiral Condensates in 158 AGeV ^{208}Pb+Pb Collisions*, Ph.D. thesis, Massachusetts Institute of Technology, 1998.

[Tho77]   W. Thome *et al.*, *Nucl. Phys.* **B129** (1977) 365.

[Tse05]   I. Tserruya, *Eur. Phys. J.* **C43** (2005) 399.

[Tse09]   I. Tserruya, *Electromagnetic Probes*, arXiv:0903.0415v2 [nucl-ex], 2009.

[Tur04]   S. Turbide, R. Rapp, and C. Gale, *Phys. Rev.* **C69** (2004) 014903.

[Ull08]   T. Ullrich Prepared for 16th International Workshop on Deep Inelastic Scattering and Related Subjects (DIS 2008), London, England.

[Uni09]   *United Generators*, http://www.gsi.de/unigen/, 2009.

[Vit02]   I. Vitev and M. Gyulassy, *Phys. Rev. Lett.* **89** (2002) 252301.

[Vit06a] I. Vitev, *J. Phys. Conf. Ser.* **50** (2006) 119.

[Vit06b] I. Vitev, *Phys. Lett.* **B639** (2006) 38.

[Vit07]   I. Vitev, *private communication*, 2007.

[Vit08]   I. Vitev and B.-W. Zhang, *Phys. Lett.* **B669** (2008) 337.

[Vog07]   W. Vogelsang, *private communication*, 2007.

[WA909]   *WA98 Collaboration Homepage*, http://wa98.web.cern.ch/WA98/, 2009.

[Wan98]   X.-N. Wang, *Phys. Rev. Lett.* **81** (1998) 2655.

[Wan00]   X.-N. Wang, *Phys. Rev.* **C61** (2000) 064910.

[Wan01]   E. Wang and X.-N. Wang, *Phys. Rev.* **C64** (2001) 034901.

[Wer93]   K. Werner, *Phys. Rept.* **232** (1993) 87.

[Won94]   C. Y. Wong, *Introduction to high-energy heavy ion collisions*, 1994, singapore, Singapore: World Scientific (1994) 516 p.

[Wur04]   J. P. Wurm and J. Bielcikova, *Elliptic flow and semi-hard scattering at SPS*, arXiv:nucl-ex/0407019v2, 2004.

[Yag05]   K. Yagi, T. Hatsuda, and Y. Miake, *Camb. Monogr. Part. Phys. Nucl. Phys. Cosmol.* **23** (2005) 1.

[Yao06]   W.-M. Yao *et al.*, *J. Phys.* **G33** (2006) 1.

[Zau07]   O. Zaudtke, *Measurement of Direct-Photon Production and Neutral Pion Double Helicity Asymmetry in Ultra-Relativistic p+p Collisions*, Ph.D. thesis, Institut für Kernphysik, Westfälische Wilhelms-Universität Münster, 2007.

[Zwe64a]   G. Zweig, *An SU(3) model for strong interaction symmetry and its breaking*, CERN-TH-401, 1964.

[Zwe64b]   G. Zweig, *An SU(3) model for strong interaction symmetry and its breaking 2*, CERN-TH-412, 1964.

D. Danksagung

Zu guter Letzt bedanke ich mich bei meinen Eltern, die mir dieses Studium ermöglicht haben, und meiner Frau Anna für ihre Unterstützung, besonders in den letzten Wochen des Verfassens dieser Arbeit.